

AN ABSTRACT OF THE DISSERTATION OF

Tony Masiello for the degree of Doctor of Philosophy in Chemistry presented on May 1, 2003.

Title: High Resolution Spectroscopy of Sulfur Trioxide and Carbon Suboxide.

Redacted for Privacy

Abstract approved: _____



Joseph W. Nibler

High resolution spectroscopy was used to study the properties of two simple polyatomic molecules, sulfur trioxide, SO_3 , and carbon suboxide, C_3O_2 .

The fundamental modes and several hot bands of the ^{18}O isotopic forms of SO_3 ($^{32}\text{S}^{18}\text{O}_3$ and $^{34}\text{S}^{18}\text{O}_3$) have been investigated using both infrared spectroscopy and coherent anti-Stokes Raman scattering spectroscopy (CARS). The Raman-active symmetric stretching mode, ν_1 , shows complex Q -branch patterns due to indirect Coriolis couplings, l -resonances, and Fermi resonances with infrared inaccessible ν_2 , ν_4 combination/overtone levels. ^{18}O isotopic substitution changes the character of these interactions in such a way that their effect on the ν_1 CARS spectrum is unique among the different isotopomers studied. Accurate rovibrational constants are determined for all of the mixed states for the first time, leading to deperturbed values for the ν_1 band origin of 1004.661(24) and 1004.693(23) for $^{34}\text{S}^{18}\text{O}_3$ and $^{32}\text{S}^{18}\text{O}_3$ respectively. The strong Coriolis coupling is very noticeable in these species due to the close proximity of the ν_2 and ν_4 fundamental vibrations. The effect that this and other interaction terms have on the ν_1 CARS spectrum of $^{34}\text{S}^{18}\text{O}_3$ is examined by selectively turning off the coupling

between the hot bands. A global force field analysis was performed with the fundamental frequency values of all of the isotopomers studied that revealed a counterintuitive trend in the bond lengths between sulfur oxide species. In addition, band center frequencies for all the mixed ^{16}O - ^{18}O isotopic species are computed.

High-resolution CARS Spectroscopy was also used to study the ν_1 symmetric CO stretching mode of the quasi-linear molecule carbon suboxide, C_3O_2 . Q -branches are seen that originate from the ground state and from thermally-populated levels of the unusually low frequency ν_7 bending mode. The intensity variation of these on cooling to about 110 K in a jet expansion requires reversal of the order of assignment given in a previous Raman study at low resolution. The identification of the ν_1 $\Sigma_g^+ \leftarrow \Sigma_g^+$ transition from the ground state is confirmed by the absence of J_{odd} Q -branch lines in the resolved CARS spectrum. Analysis of this band leads to vibration-rotation parameters (in cm^{-1}) of $\nu_1 = 2199.9721(6)$, $(B' - B'') = 2.029(6) \times 10^{-4}$. Other transitions originating from higher ν_7 levels occur at only slightly lower wavenumber values, indicating that the ground state barrier to linearity (22 cm^{-1}) increases only 1 to 2 cm^{-1} when the CO symmetric stretch is excited.

©Copyright by Tony Masiello
May 1, 2003
All Rights Reserved

High Resolution Spectroscopy of Sulfur Trioxide and Carbon Suboxide

by
Tony Masiello

A DISSERTATION

submitted to

Oregon State University

in partial fulfillment of
the requirements for the
degree of

Doctor of Philosophy

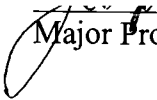
Presented May 1, 2003

Commencement June 2003

Doctor of Philosophy dissertation of Tony Masiello presented on May 1, 2003

APPROVED:

Redacted for Privacy

 _____
Major Professor, representing Chemistry

Redacted for Privacy


Chair of the Department of Chemistry

Redacted for Privacy

Dean of the Graduate School

I understand that my dissertation will become part of the permanent collection of Oregon State University libraries. My signature below authorizes release of my dissertation to any reader upon request.

Redacted for Privacy

 _____
Tony Masiello, Author

CONTRIBUTION OF AUTHORS

Joseph W. Nibler contributed to the writing of all of the chapters and analysis of the spectra. Jeffrey Barber contributed in the synthesis of the $^{32}\text{S}^{18}\text{O}_3$ sample, the analysis of the spectra, and the improvements to the infrared analysis program. Engelen t.H. Chrysostom collected the CARS spectra for the SO_3 molecules. Arthur Maki assisted in the final data analysis of the infrared spectra. Thomas A. Blake and Robert L. Sams assisted in the collection of the infrared data.

TABLE OF CONTENTS

	<u>Page</u>
1 Introduction	1
1.1 Overview of Thesis	1
1.2 Literature Review	3
2 High Resolution Spectroscopic Studies of $^{32}\text{S}^{18}\text{O}_3$ and $^{34}\text{S}^{18}\text{O}_3$	5
2.1 Introduction	5
2.1.1 The Modes of Vibration	5
2.1.2 Nuclear Spin Considerations	8
2.1.3 Initial Effort	10
2.1.4 Breakdown of the Analysis	13
2.2 Experimental Details	15
2.3 Results	19
2.4 Analysis	21
2.4.1 Energy Level Expression for the Ground State	21
2.4.2 ν_2, ν_4	24
2.4.3 Energy Levels for $\nu_1, 2\nu_2, \nu_2+\nu_4$ and $2\nu_4$ States	26
2.5 Vibration-Rotation Constants for $^{34}\text{S}^{18}\text{O}_3$	30
2.5.1 Ground State	30
2.5.2 ν_2 and ν_4 Parameters	32
2.5.3 Hot Bands Involving ν_2 and ν_4	34
2.5.4 The ν_1 Level Perturbations and Their Effect on the Calculated CARS spectrum	38
2.5.5 ν_1 Parameters	52
2.5.6 The Anharmonicity Constants	52
2.5.7 The Rotational Constants and Equilibrium Bond Length for $^{34}\text{S}^{18}\text{O}_3$	54

TABLE OF CONTENTS (Continued)

	<u>Page</u>
2.6 Studies of $^{32}\text{S}^{18}\text{O}_3$	56
2.6.1 Ground State Parameters	56
2.6.2 Parameters for ν_2 , ν_4 , $2\nu_2$, $\nu_2+\nu_4$ and $2\nu_4$	58
2.6.3 The ν_2/ν_4 Hot Bands	62
2.6.4 The ν_1 Constants and the Calculated CARS spectrum	62
2.6.5 The Anharmonicity Constants	68
2.6.6 The Equilibrium Bond Lengths	68
2.6.7 The Force Constants	72
3 Coherent Raman Spectra of the ν_1 Mode of Carbon Suboxide	76
3.1 Introduction	76
3.2 Experimental	80
3.3 Results and Discussion	83
3.3.1 CARS spectra of C_3O_2	83
3.3.2 Modeling of Spectra	85
3.3.3 Implications for ν_7 Bending Potential in the ν_1 Manifold	90
3.3.4 Axial Force Constants and Bonding in C_3O_2	91
4 Conclusion	95
Bibliography	97

LIST OF FIGURES

<u>Figure</u>		<u>Page</u>
2.1	The vibrational modes of SO ₃	6
2.2	The possible a_1' ground state rotational energy levels for SO ₃	9
2.3	The CARS spectra for ³² S ¹⁶ O ₃ and ³⁴ S ¹⁶ O ₃	11
2.4	The CARS spectra for ³² S ¹⁸ O ₃ and ³⁴ S ¹⁸ O ₃	12
2.5	Vibrational energy level diagram for SO ₃	14
2.6	The experimental CARS apparatus	18
2.7	The experimental infrared spectra of the ν_2, ν_4 region for all of the studied isotopomers of SO ₃	20
2.8	High resolution IR spectrum of ³⁴ S ¹⁸ O ₃ showing Coriolis perturbations	35
2.9	Infrared spectrum of the ν_2, ν_4 region of ³⁴ S ¹⁸ O ₃ and calculated spectra of hot bands involving ν_1 perturbing states	36
2.10	The relative positions of ν_1 and $2\nu_4$ for all of the isotopomers	39
2.11	Reduced energy diagram of Q -branch transitions from the ground state of ³⁴ S ¹⁸ O ₃ to ν_1 and its perturbing states	40
2.12	Experimental and calculated CARS spectra for ³⁴ S ¹⁸ O ₃ , along with an expanded view of Fig. 2.11 showing how the level pattern contributes to the appearance of the spectrum	42
2.13	The CARS spectrum of ν_1 of ³⁴ S ¹⁸ O ₃	43
2.14	Effect on ν_1 CARS spectrum of setting the Fermi resonance constants k_{122} and k_{144} to zero	44

LIST OF FIGURES (CONTINUED)

<u>Figure</u>		<u>Page</u>
2.15	Effect on the ν_1 CARS spectrum (top) and reduced energy diagram (bottom) of setting all $W_{1,1}$ and $W_{2,2}$ interactions to zero but with all Fermi resonance interactions on	45
2.16	Effect on the ν_1 CARS spectrum and reduced energy diagram of setting all $W_{1,1}$ interactions to zero but with $W_{2,2}$ and Fermi resonance interactions on	46
2.17	Effect on the ν_1 CARS spectrum and reduced energy diagram of setting $W_{1,1}$ for the $\nu_2+\nu_4/2\nu_4$ coupling to zero, but with $W_{2,2}$ and Fermi resonance interactions and $W_{1,1}$ for $\nu_2+\nu_4/2\nu_2$ coupling on	47
2.18	Effect on the ν_1 CARS spectrum and reduced energy diagram of setting $W_{1,1}$ for the $\nu_2+\nu_4/2\nu_2$ coupling to zero but with $W_{2,2}$ and Fermi resonance interactions and $W_{1,1}$ for $\nu_2+\nu_4/2\nu_4$ on	48
2.19	High resolution IR spectrum of $^{32}\text{S}^{18}\text{O}_3$. The effect of the Coriolis perturbation is demonstrated with the shifting of the predicted line positions $^R R_{12}(23)$ through $^R R_{12}(25)$ sequence	60
2.20	The CARS spectrum of ν_1 of $^{32}\text{S}^{18}\text{O}_3$	64
2.21	Reduced energy diagram of Q -branch transitions from the ground state of $^{32}\text{S}^{18}\text{O}_3$ to ν_1 and its perturbing states	66
2.22	Experimental and calculated CARS spectra for $^{32}\text{S}^{18}\text{O}_3$ along with an expanded view of Fig. 21 showing the level pattern to illustrate how this pattern contributes to the appearance of the spectrum	67
2.23	Effect of ν_1 CARS spectrum of setting the Fermi resonance constants k_{122} and k_{144} to zero	70
3.1	The vibrational modes of C_3O_2	78

LIST OF FIGURES (CONTINUED)

3.2	The effective potential well of the ν_2 , ν_4 , and ν_5 levels	79
3.3	Raman and CARS spectra of C_3O_2	84
3.4	The rotational modeling of the Q -branch of C_3O_2	86
3.5	The vibrational modeling of C_3O_2	89

LIST OF TABLES

<u>Table</u>		<u>Page</u>
2.1	Data Files Used in the Analysis of $^{32}\text{S}^{18}\text{O}_3$ and $^{34}\text{S}^{18}\text{O}_3$	22
2.2	The 7×7 Hamiltonian Matrix Describing Possible Interactions with ν_1 States	28
2.3	Ground-State Rotational Constants in cm^{-1} for $^{34}\text{S}^{18}\text{O}_3$	31
2.4	The Rovibrational Constants in cm^{-1} for the ν_2, ν_4 States for the Fundamentals and Hot Bands of $^{34}\text{S}^{18}\text{O}_3$	33
2.5	The Rovibrational Constants in cm^{-1} for ν_1 of $^{34}\text{S}^{18}\text{O}_3$	51
2.6	Anharmonic Constants in cm^{-1} for $^{34}\text{S}^{18}\text{O}_3$	53
2.7	Rotational Constants for $^{34}\text{S}^{18}\text{O}_3$	55
2.8	Ground-State Rotational Constants in cm^{-1} for $^{32}\text{S}^{18}\text{O}_3$	57
2.9	The Rovibrational Constants in cm^{-1} for the ν_2, ν_4 States for the Fundamentals and Hot Bands of $^{32}\text{S}^{18}\text{O}_3$	59
2.10	The Rovibrational Constants in cm^{-1} for ν_1 of $^{32}\text{S}^{18}\text{O}_3$	65
2.11	Anharmonic Constants in cm^{-1} for $^{32}\text{S}^{18}\text{O}_3$	69
2.12	Rotational Constants for $^{32}\text{S}^{18}\text{O}_3$	71
2.13	Predicted Frequencies of the Isotopomers of SO_3	74
2.14	Calculated Force Constants for Different Oxides of Sulfur	75
3.1	CARS Transitions and Vibrational-Rotational Parameters	88
3.2	Harmonic Force Constants for C_3O_2	92
3.3	Internal Force Constants for C_3O_2 and Related Molecules	93

High Resolution Spectroscopy of Sulfur Trioxide and Carbon Suboxide

1 Introduction

1.1 Overview of Thesis

The research described in this thesis focuses on the use of high resolution molecular spectroscopy as a method of studying interesting properties of simple polyatomic molecules. Integral to this research is the use of coherent anti-Stokes Raman scattering (CARS) spectroscopy as a molecular probe. Oregon State University houses one of the most well-equipped facilities in the world for coherent Raman spectroscopy and it has been used for a variety of applications. For this investigation, CARS is used to examine two structurally simple polyatomic molecules, SO_3 and C_3O_2 .

In the first of these cases, the ν_1 symmetric stretch of sulfur trioxide, SO_3 , has been studied. A complete understanding of the subtle interactions that perturb this mode took the collaboration of a myriad of scientists and so far has led to six published papers on which I am coauthor (1-6). These involved the investigation of not only the parent isotopomer of sulfur trioxide, $^{32}\text{S}^{16}\text{O}_3$, but also of the isotopic variants with substitution of ^{34}S and/or ^{18}O . Studies of the two forms of SO_3 containing ^{16}O are presented in the thesis of Jeffrey Barber. My thesis research involved the synthesis, recording of spectra, and analysis of the ^{18}O counterparts,

$^{32}\text{S}^{18}\text{O}_3$ and $^{34}\text{S}^{18}\text{O}_3$. This work contributes to the body of knowledge about the spectroscopic and structural properties of SO_3 , as described in chapter 2.

The second intriguing system studied using CARS spectroscopy is carbon suboxide (C_3O_2). This molecule is unusual in that it has an extremely low frequency bending motion at a frequency of 18 cm^{-1} . The Lewis configuration normally written for C_3O_2 is linear, $\text{O}=\text{C}=\text{C}=\text{C}=\text{O}$, so that one would expect a stiff linear structure. However, high level *ab initio* calculations indicate that the equilibrium structure is bent, but with a very low barrier to linearity in the ground state, so the average structure is linear. The molecule is thus said to be quasi-linear. This property leads to rich vibrational spectra due to hot bands involving the bend. Much work has been done on this molecule to examine the infrared-active transitions, but little has been done on the Raman active ν_1 symmetric CO stretching mode. In this study I synthesized C_3O_2 and recorded high resolution CARS spectra of this mode for both static and jet-cooled samples. The results show that previous studies involving this mode require reinterpretation and reveal how excitation of the CO bonds influences the bending potential. The work is discussed in chapter 3.

Finally, chapter 4 summarizes some of the principal findings from both studies and indicates possible areas for future investigation.

1.2 Literature Review

As mentioned above, so far our efforts have led to six publications on the topic of SO_3 , each with a unique aspect. Because these publications are referenced throughout this work a summary of the more important aspects of each is given.

The first publication (1) gives a general overview of the unique problems posed in the CARS analysis of the ν_1 symmetric stretching mode of SO_3 . It details efforts made to model the CARS spectrum of $^{32}\text{S}^{16}\text{O}_3$, and shows how the CARS spectrum changes upon isotopic substitution of ^{18}O for ^{16}O . Medium resolution (0.125 cm^{-1}) infrared spectra and CARS spectra of $^{32}\text{S}^{16}\text{O}_3$, $^{32}\text{S}^{18}\text{O}_3$ and the 16-18 mixed isotopomers are given.

The second publication reports on the fundamental vibrations of ν_2 , ν_3 , ν_4 and the overtone $2\nu_3$ for the $^{32}\text{S}^{16}\text{O}_3$ isotopomer. Comparisons are made between these new measurements and previous less detailed studies at lower resolution. Further analysis of the $^{32}\text{S}^{16}\text{O}_3$ data is made in the third publication, which deals specifically with the hot bands of the ν_2 and ν_4 vibrations and the subtle, but critical interactions that couple the $2\nu_2$, $\nu_2+\nu_4$ and $2\nu_4$ states to one other, and to the ν_1 levels. Only when these hot bands and interactions are properly taken into account is an accurate analysis of the CARS spectrum achieved.

A similar treatment of $^{34}\text{S}^{16}\text{O}_3$ is given in the next two publications (4, 5). The results of the analysis of the ν_2 and ν_4 fundamental vibrations is given in reference 4 along with an investigation of the intensity perturbations caused by

Coriolis and *l*-type interactions between ν_2 and ν_4 . The results of the hot band analysis are reported in publication 5 along with the calculated CARS spectrum for the ν_1 vibration of $^{34}\text{S}^{16}\text{O}_3$ that takes the interactions with the hot bands into account. Comparisons between the results of $^{34}\text{S}^{16}\text{O}_3$ and $^{32}\text{S}^{16}\text{O}_3$ are given.

Publication 6 reports on the antisymmetric stretching mode, ν_3 , and on the $2\nu_3$ bands of all of the symmetric isotopomers, $^{32}\text{S}^{16}\text{O}_3$, $^{34}\text{S}^{16}\text{O}_3$, $^{32}\text{S}^{18}\text{O}_3$, $^{34}\text{S}^{18}\text{O}_3$. This vibrational motion is found to be almost completely unperturbed by the other vibrational modes and the effects of the mass changes are discussed.

Finally, the work presented in this thesis will be submitted for two and possibly three additional papers. This body of work will make SO_3 one of the most carefully and accurately characterized non-linear polyatomic molecules ever studied by molecular spectroscopy. We believe that SO_3 will become a "standard" by which spectroscopic studies of other molecules will be judged.

2. High Resolution Spectroscopic Studies of $^{32}\text{S}^{18}\text{O}_3$ and $^{34}\text{S}^{18}\text{O}_3$

2.1 Introduction

Sulfur trioxide is an important molecule both environmentally and industrially. Chemically, it is one of the most powerful oxidizing agents known, but it finds its main application serving as a chemical precursor in the production of sulfuric acid. Environmentally, it is thought of as a nuisance, making its way into the atmosphere through the combustion of sulfur-containing compounds. Once in the atmosphere it is long-lived, and when mixed with water vapor, contributes extensively to acid rain. SO_3 is of astronomical interest due to its presence on the planet Venus (7) and Jupiter's moon Io (8). Spectroscopically, it is interesting in that it serves as an example of a simple oblate top and, with perhaps the exception of BF_3 , is the most easily recognizable trigonal-planar molecule. However, unlike the latter molecule, the spectroscopy of SO_3 is greatly simplified by nuclear spin restrictions. It is therefore amenable to detailed study.

2.1.1 The Modes of Vibration

Early spectroscopic (9, 10) and electron diffraction analysis (11) determined that SO_3 is a planar oblate top molecule possessing D_{3h} symmetry. There are six fundamental vibrational modes for a molecule possessing such symmetry, two pairs of which are degenerate (Fig. 2.1). The vibration of lowest energy, ν_2 , is an out-of-

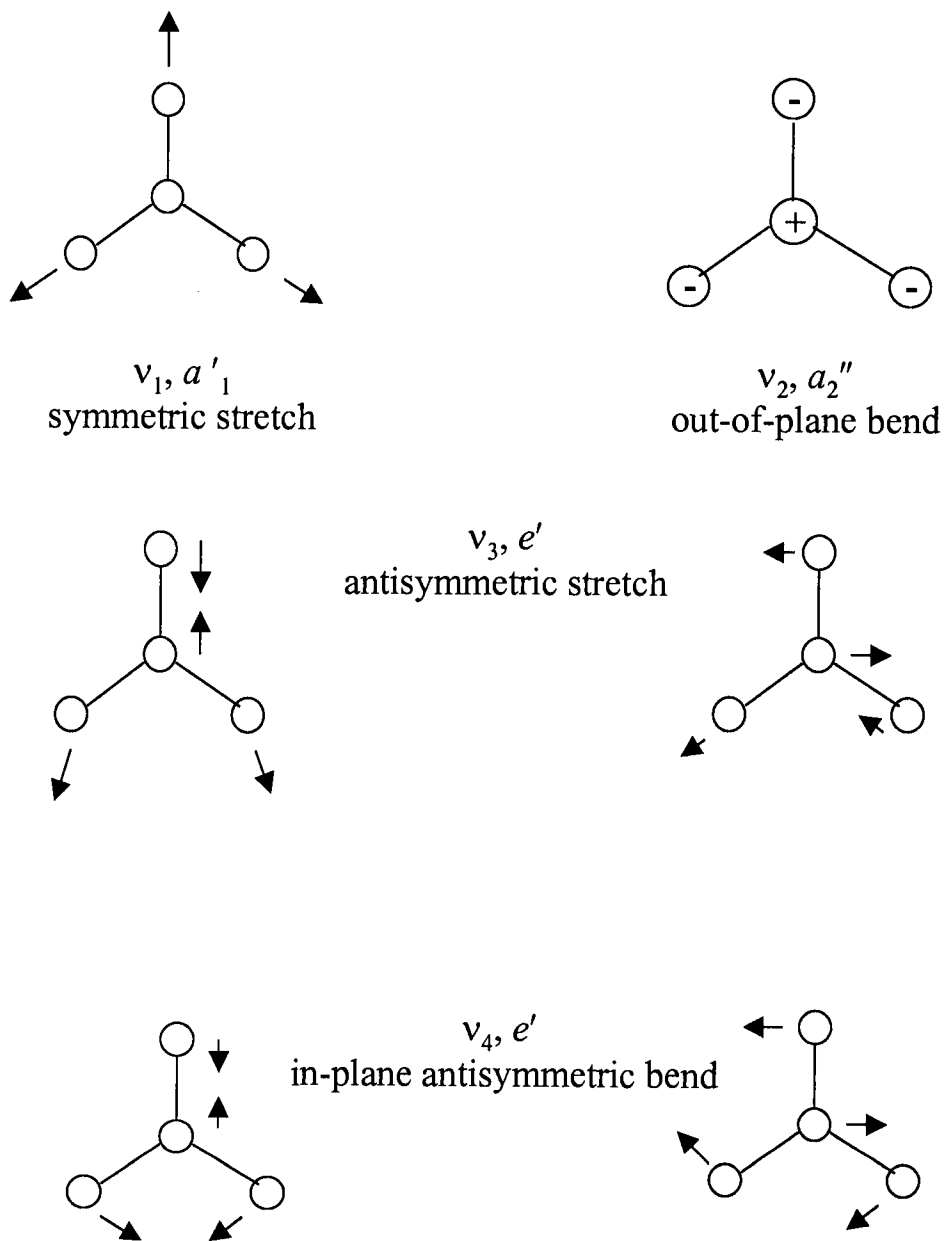


Fig. 2.1 The vibrational modes of SO_3

plane bend. It is termed a parallel vibration because the vibrational mode produces a changing dipole moment along the principal symmetry axis, the axis perpendicular to the symmetry plane and passing through the central sulfur atom. The sulfur atom is displaced above and below the symmetry plane in this vibration. For such a parallel vibration only transitions with $\Delta K=0$, $\Delta J = 0, \pm 1$ are allowed, where J is the quantum number that characterizes the total rotational momentum and K measures its component along the symmetry axis. The other bending motion is an in-plane vibration, ν_4 . It is a perpendicular vibration since the changing dipole moment (and thus molecular motion) lies in a plane perpendicular to the principal symmetry axis. For a perpendicular transition the selection rules state that $\Delta K = \pm 1$, $\Delta J = 0, \pm 1$.

The ν_1 vibrational mode is one in which the oxygen atoms stretch symmetrically in the plane of the molecule. No electric dipole is produced in this vibration, however a net change in the polarizability of the molecule does result, and thus this vibration is accessible through Raman spectroscopy. The selection rules for this vibration are that $\Delta K = 0$, $\Delta J = 0, \pm 2$. In CARS spectroscopy however, only Q -branch structure corresponding to transitions where $\Delta K=0$, $\Delta J=0$ have appreciable intensity and this is all that was observed for SO_3 . The fundamental vibration of highest energy is the ν_3 perpendicular antisymmetric stretching vibration. Both the ν_3 and ν_4 perpendicular vibrations are degenerate and will have associated with their description, a third quantum number, l , (l_3 or l_4), which implies a vibrational motion that produces a net angular momentum. This angular momentum can couple to angular momentum corresponding to rotation about the symmetry axis (characterized

by K) and it turns out that states of common J and $k-l$ quantum numbers are mixed (lower case k and l are signed quantum numbers). A complete vibrational state designation is given by the quantum level $(v_1 v_2 v_3^l v_4^l)$, so, for example, the ground state is $(000^0 0^0)$ and the reference v_4 means a transition $(000^0 1^1) \leftarrow (000^0 0^0)$.

2.1.2 Nuclear Spin Considerations

The analysis of the vibrational spectra of SO_3 is greatly simplified by the fact that both ^{18}O and ^{16}O are Bosons with zero nuclear spin. Nuclear spin statistics restrict the population of the ground state of such a molecule possessing three-fold symmetry to levels where $K=3n$ ($n=0, 1, 2, \dots$). In addition, for $K=0$, only even J levels are allowed. In contrast, about three times as many levels (Fig. 2.2) can be occupied in a molecule, such as S^{17}O_3 , which possesses D_{3h} symmetry but has an atomic ligand with non-zero spin (^{17}O has $I=5/2$ and is a Fermion).

The pattern of levels shown in Fig. 2.2 applies to a state of A_1' symmetry. For degenerate E vibrational states, only the $K=3\pm 1$ levels are occupied and, for each J the rotational levels are usually split in to an $A_1' - A_2'$ pair, lying above and below a mean position. For S^{16}O_3 and S^{18}O_3 , nuclear spin statistics restrict population to only the A_1' level, whose energy is thus observed to be staggered with J , alternating above and below an average position.

Sulfur trioxide is thus spectroscopically interesting as perhaps the prototypical oblate symmetric top molecule and, initially, we expected its spectrum

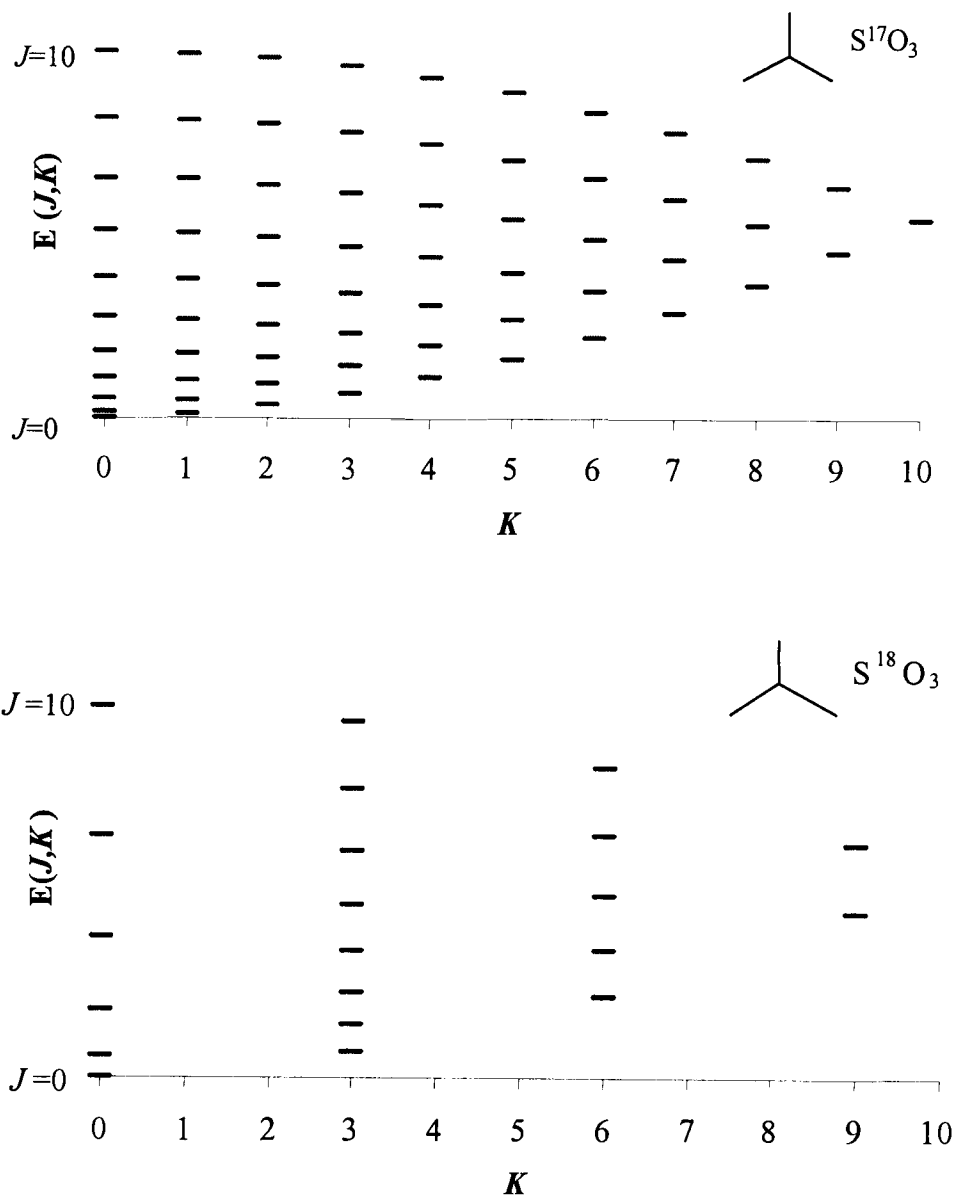


Fig. 2.2 The possible a_1' ground state rotational energy levels for SO₃. ¹⁷O is a Fermion ($I = 5/2$) and has rotational levels in its ground state ($J=K, K+1 \dots$) as displayed at the top. ¹⁸O on the other hand is a spin zero Boson and only every third K level will exist, as shown at the bottom. In addition, in the $K=0$ state, only even J states exist for a planar molecule. For an a_2'' vibrational level, only odd J levels are allowed for $K=0$.

to be simple. This proved not to be the case however, as evidenced by the complex and quite different ν_1 CARS spectra discussed below.

2.1.3 Initial Effort

The parent isotopomer of $^{32}\text{S}^{16}\text{O}_3$ was the first to be studied with CARS spectroscopy. It revealed a surprisingly complex spectrum (Fig. 2.3) for the ν_1 symmetric SO_3 stretch, showing two apparent Q -branch structures, separated by 2 cm^{-1} , which trailed off in opposite directions. This result was very unexpected when contrasted with the predicted Q -branch structure of such an oblate symmetric top, one Q -branch that trails off in intensity to lower Raman shift. Many possible explanations for this complexity were considered and rejected, such as chemical impurities, hot-bands involving ν_1 , and first or second order Coriolis couplings to other fundamental vibrations. One hypothesis considered was the idea that coupling to overtone levels of the ν_2 and ν_4 fundamental modes through a Fermi resonance perturbed the ν_1 levels. Both the $2\nu_2$ and $2\nu_4(l = 0)$ states possess the proper symmetry to couple with ν_1 through this type of interaction.

To test this proposition, CARS experiments on other isotopomers of SO_3 were carried out with the idea that the frequencies of the fundamental vibrations, and consequently the interacting levels, would change in a predictable fashion upon isotopic substitution. The startling result, as evidenced by Figs. 2.3 and 2.4, is that the CARS spectrum of each isotopomer is completely unique. Fully characterizing the ν_1 mode for each isotopomer turned out to be a major challenge, requiring a

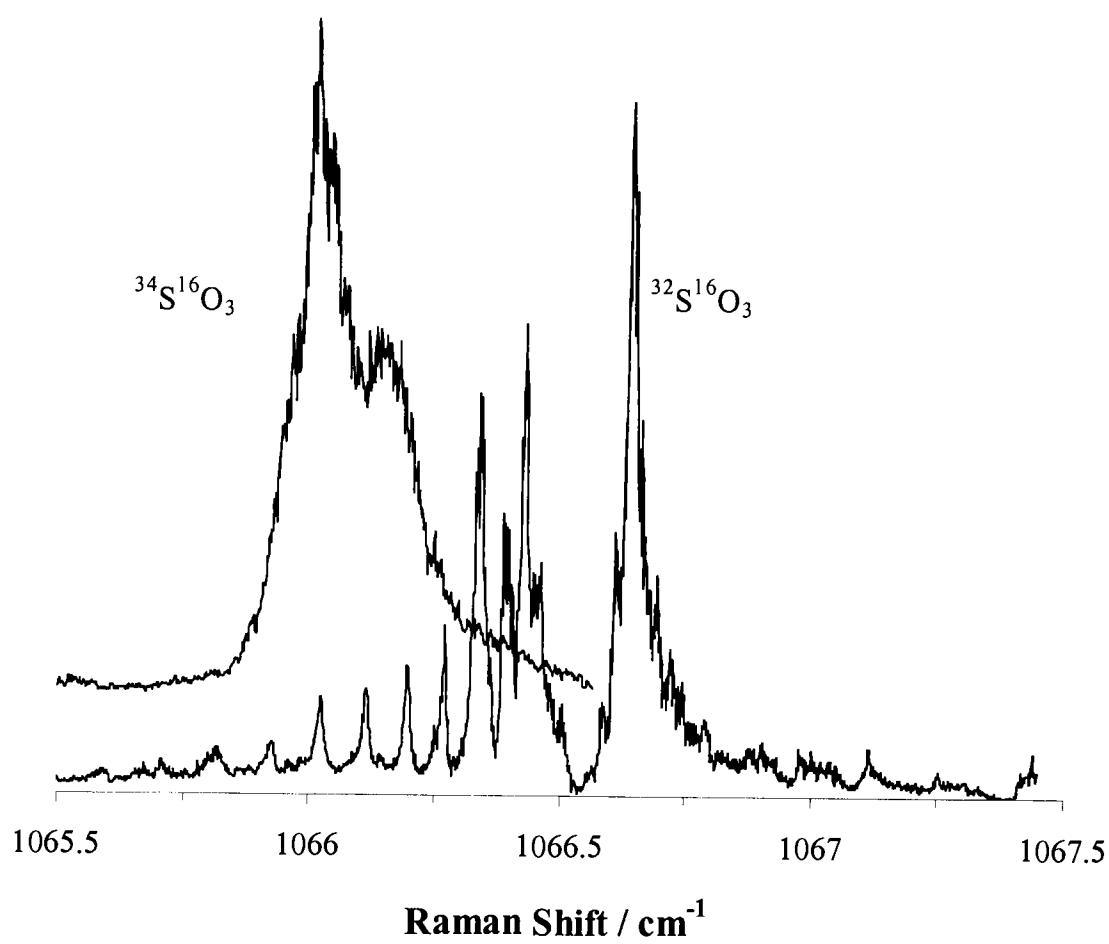


Fig. 2.3 The CARS spectra of ν_1 for $^{32}\text{S}^{16}\text{O}_3$ and $^{34}\text{S}^{16}\text{O}_3$.

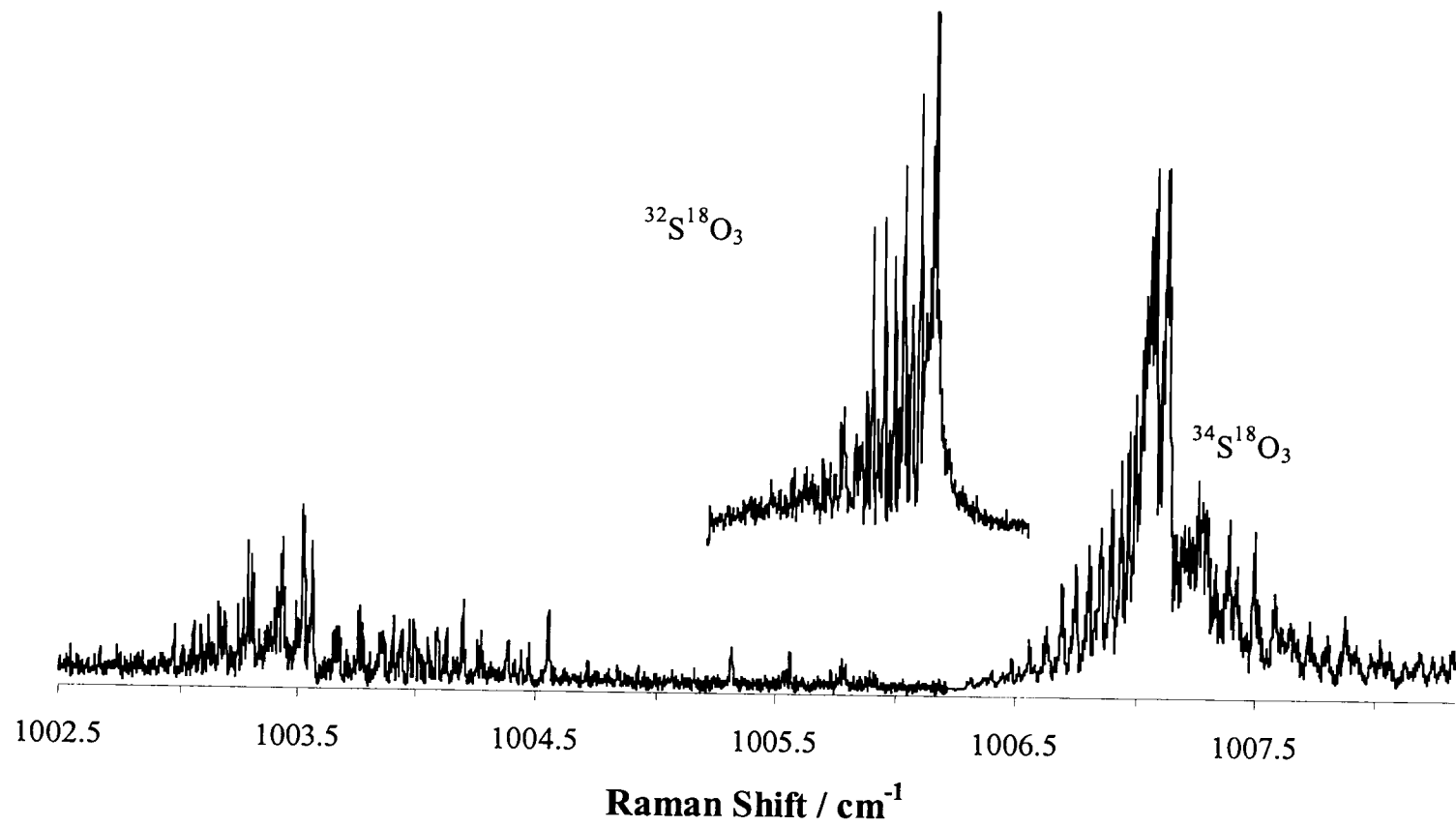


Fig. 2.4 The CARS spectra of ν_1 for $^{32}\text{S}^{18}\text{O}_3$ and $^{34}\text{S}^{18}\text{O}_3$.

detailed analysis of the infrared vibrations of ν_2 and ν_4 along with the hot bands involving these.

2.1.4 Breakdown of the Analysis

The spectral analysis of transitions to the ν_1 levels is complicated by the Fermi resonance of these with the states of $2\nu_2$ and $2\nu_4(l = 0)$. These latter state are in turn greatly perturbed by Coriolis and l -doubling interactions with $\nu_2 + \nu_4(l = \pm 1)$ and $2\nu_4(l = \pm 2)$ levels. The vibrational energy diagram for SO_3 shown in Fig. 2.5 gives an overview of the interactions that, together, result in the complex ν_1 spectra. Successful analysis has already been achieved and reported in the published work involving the two ^{16}O isotopomers (3, 5). The analysis of the ^{18}O species, the focus of my research, is slightly more complex, as will be discussed in the rest of this chapter.

I wish to acknowledge that this work has benefited from collaboration with several scientists. The initial CARS spectra were obtained with Dr. Alfons Weber (N.I.S.T. and N.S.F.) during a summer leave at O.S.U. Key to the theoretical analysis has been Dr. Art Maki (retired, N.I.S.T.), a veteran of previous $^{32}\text{S}^{16}\text{O}_3$ studies, and author of some of the analysis programs. Finally, the high resolution infrared spectra were recorded using the special six meter Bruker FTIR instrument at the user facility at Pacific Northwest National Laboratories in Richland, WA. The scientists there were Drs. Tom Blake, Bob Sams and Steve Sharpe. O.S.U. students who have worked on various aspects of SO_3 are Engelene Chrysostom, Nicu

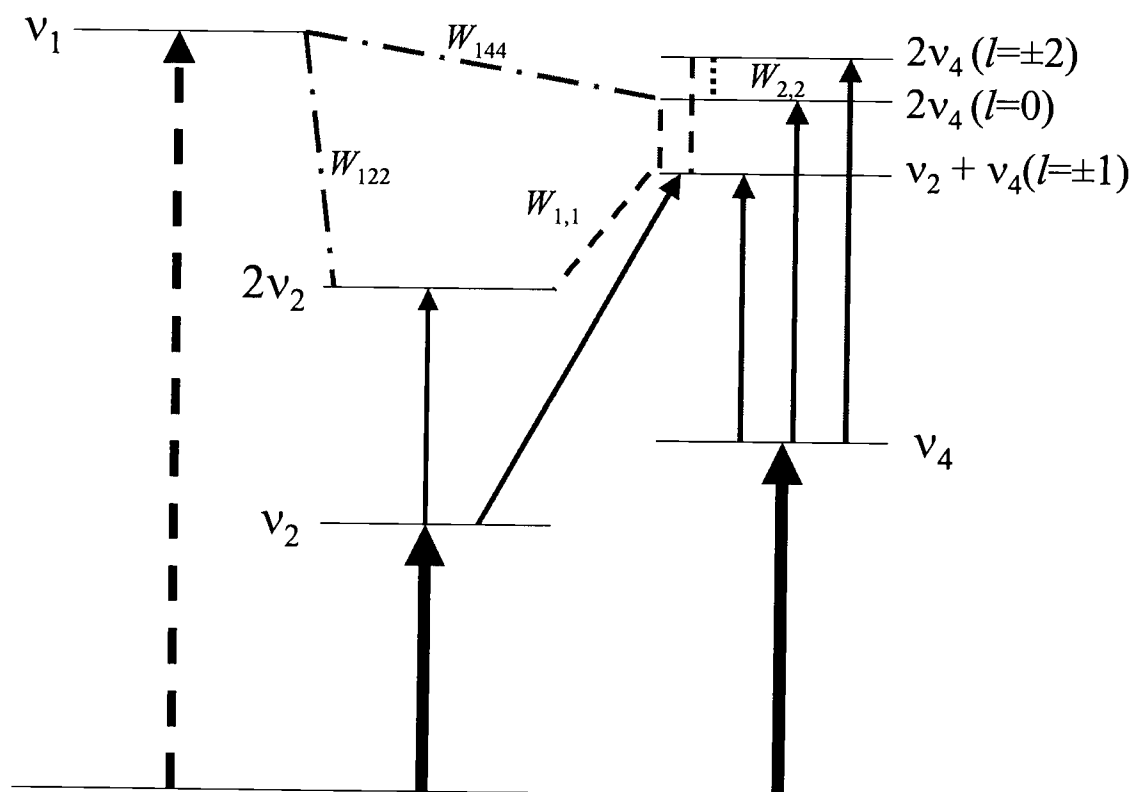
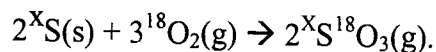


Fig. 2.5 Vibrational energy level diagram for SO_3 . Bold arrows indicate Raman (dashed) and infrared (solid) transitions. Lines between levels indicate the couplings between states, including Fermi resonances (---), Coriolis interactions (-.-.), and l -resonances (.....). Not shown are the l -resonance interactions within the $v_2 + v_4 (l = \pm 1)$ and $2v_4 (l = \pm 2)$ states.

Vulpanovici, Jeffrey Barber, John Frieh, and myself. This collaborative group is large, due mostly to the fact that no isotopic forms of SO₃ had been studied in either the infrared or Raman before this project and the analysis has involved all vibrations and many overtone-combination bands. The result is that SO₃ is now one of the most completely understood of all polyatomic molecules.

2.2 Experimental Details

The different isotopomers of S¹⁸O₃ were synthesized by oxidation of sulfur,



Typically ~ 0.1 g of sulfur was placed in a 0.2 L reaction vessel along with a few pieces of platinum foil that acts to catalyze the further oxidation of the initial product SO₂ to SO₃ (contact process). The sulfur used in the production of ³²S¹⁸O₃ has a natural ³²S abundance of 95.02% (12) while the ³⁴S (Cambridge Isotope Laboratories) burned to generate ³⁴S¹⁸O₃ has a stated purity of 99.8%. Initially, the glass reaction vessel was heated to 50 °C while being evacuated to remove any residual water, a contaminant that would not only reduce the yield of SO₃, but would also promote exchange of ¹⁶O. A stoichiometric excess of ¹⁸O₂ gas (Isotech Laboratories, 98.3%) was added to the reaction vessel and it was then cooked at 450 °C for at least 48 hours. The main products of the reaction were SO₃ and some residual SO₂. For final purification, the reaction vessel was frozen in liquid nitrogen, pumped on to remove any excess oxygen, then warmed to -60 °C at which point the

SO₂ (vapor pressure, 39.7 torr) was pumped away from the solid SO₃ product (vapor pressure, 0.07 torr)(12).

Sulfur trioxide is a highly reactive oxidant and care had to be taken to reduce the chances of contamination due to reaction with cell materials and, particularly, with water. Glass manifolds along with Teflon stopcocks and connectors were used during the synthesis. The 19.95 cm ± 0.01 cm infrared cell was made of stainless steel, electropolished, and gold plated. The cell windows had to be inert enough to withstand attack from SO₃, yet be able to transmit in the low infrared region. AgCl windows proved to be the only acceptable material and possess both properties with the only evidence of reaction being the presence of faint transitions from HCl. An inert fluorocarbon lubricant (Kel-F) was used to coat Viton O-rings that were used to seal the windows to the cell.

The infrared spectra were recorded on a Bruker IFS 120 HR Fourier transform spectrometer at the PNNL facilities in Richland, WA. The sample cell had a double jacket that allowed for a mixture of water/ethylene glycol to flow through it to maintain a constant temperature of 25.00 ± 0.02 °C throughout the recordings. For the low frequency ν_2 , ν_4 spectral region, a Si:Ga liquid helium cooled detector (bolometer) was used with a KBr beamsplitter. The gas pressure and number of averaged scans were 0.40 kPa (3.0 torr) and 18 scans for ³²S¹⁸O₃ and 0.24 kPa (1.8 torr) and 240 scans for ³⁴S¹⁸O₃. The instrumental resolution has been determined (2) to be 0.0015 cm⁻¹. Weak transitions of CO₂ near 650 cm⁻¹ were still observed in the spectra indicating that the spectrometer path was not completely evacuated. These,

in fact, served as a convenient method of absolute wavelength calibration yielding a measurement accuracy estimated to be about 0.00015 cm^{-1} .

The CARS apparatus (Fig. 2.6) at Oregon State University was used to obtain the high resolution Raman spectra of the isotopomers of SO_3 . This system is unusual for Raman spectroscopy in that the overall effective resolution capability has been shown to be very good, 0.001 cm^{-1} (13). The unique component of this system is a seeded, single frequency Nd:YAG laser (Continuum, custom laser) that is frequency doubled to deliver 45-50 ns pulses of 532 nm light at 20 Hz and 100 mJ/pulse. This long pulse, about ten times that of most commercial lasers, gives the high spectral resolution of our system. The frequency of the Nd:YAG laser was locked to $18788.4624(15) \text{ cm}^{-1}$ by adjustment of the temperature controller on the seed laser (Lightwave model 122, 50 mW) and monitoring the output through a cell of iodine vapor such that the frequency of the green light corresponded to a position of 50% absorption intensity on the blue side of line No. 1111 of the Iodine atlas (14).

Part of this green output is used to pump a pulse amplification chain for the tunable Stokes source that originates from an argon ion pumped (Coherent, Innova 200, 6 W) ring dye laser (Continuum, 699-29). Two portions of the 532 nm output were focused along with the pulse amplified Stokes beam into the sample in a folded BOXCARS geometric arrangement. The energies of the pump and Stokes beams were between 2-4 mJ/pulse and 0.3 to 2 mJ/pulse respectively. The signal was spatially and optically filtered before being detected by a Hamamatsu R955 photomultiplier and integrated by a Stanford Research signal averager (SR 250). A

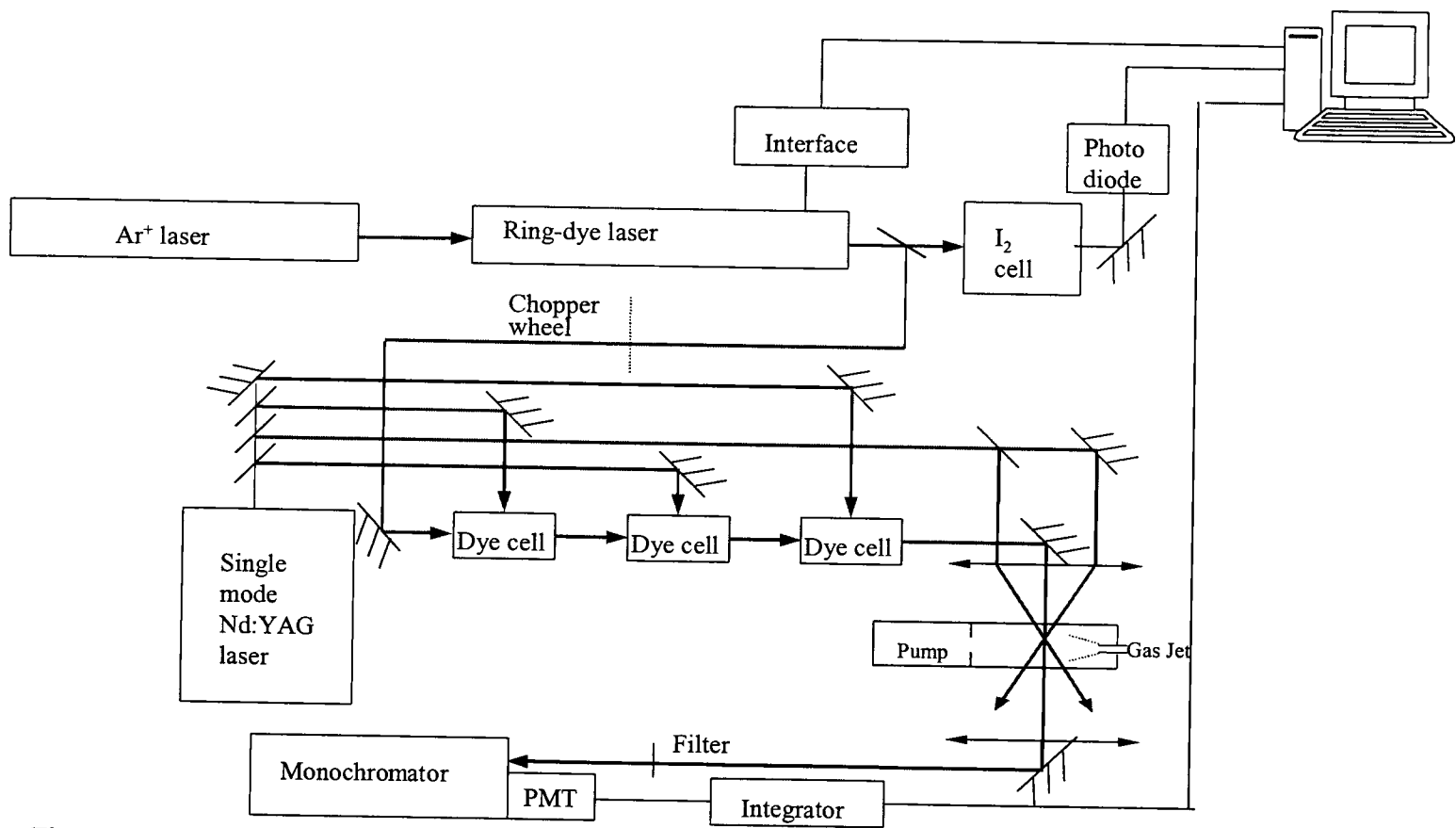


Fig. 2.6 The experimental CARS apparatus

small portion of the light from the ring dye laser was sent through a cell of iodine vapor and recorded in order to calibrate the spectra using the Iodine atlas lines. A glass cell with glass windows sealed again with Kel-F coated Viton o-rings was used to contain the SO_3 for the CARS experiment. A freeze-out tip on the cell was immersed in a salt/ice mixture ranging in temperature from -10 to -20 °C to obtain a sample pressure ranging from 0.9 to 2.4 kPa (7 to 18 torr).

2.3 Results

CARS spectra obtained for $^{32}\text{S}^{18}\text{O}_3$ and $^{34}\text{S}^{18}\text{O}_3$ are shown in Fig. 2.4 and were recorded at pressures of about 10 torr, where collision broadening is expected to be about equal to the Doppler width (0.0015 cm^{-1}) for each line. Additional broadening comes from the laser linewidth (0.001 cm^{-1}) and probably from some saturation and ac-Stark broadening effects at the laser powers employed for these studies. Because of spectral congestion in the Q -branches, in only a few cases was it possible to identify isolated lines in the CARS spectra. Hence, the CARS data were used primarily as a guide in analyzing the well defined P and R line structure of the FTIR spectra. The molecular parameters thus deduced in this work are considered quite reliable since the FTIR measurements are of exceptionally high quality with very small frequency uncertainty.

Fig. 2.7 provides a display of the ν_2 , ν_4 region examined for each of the isotopomers. Although the ν_2 and ν_4 bands overlap somewhat, the general P - Q - R

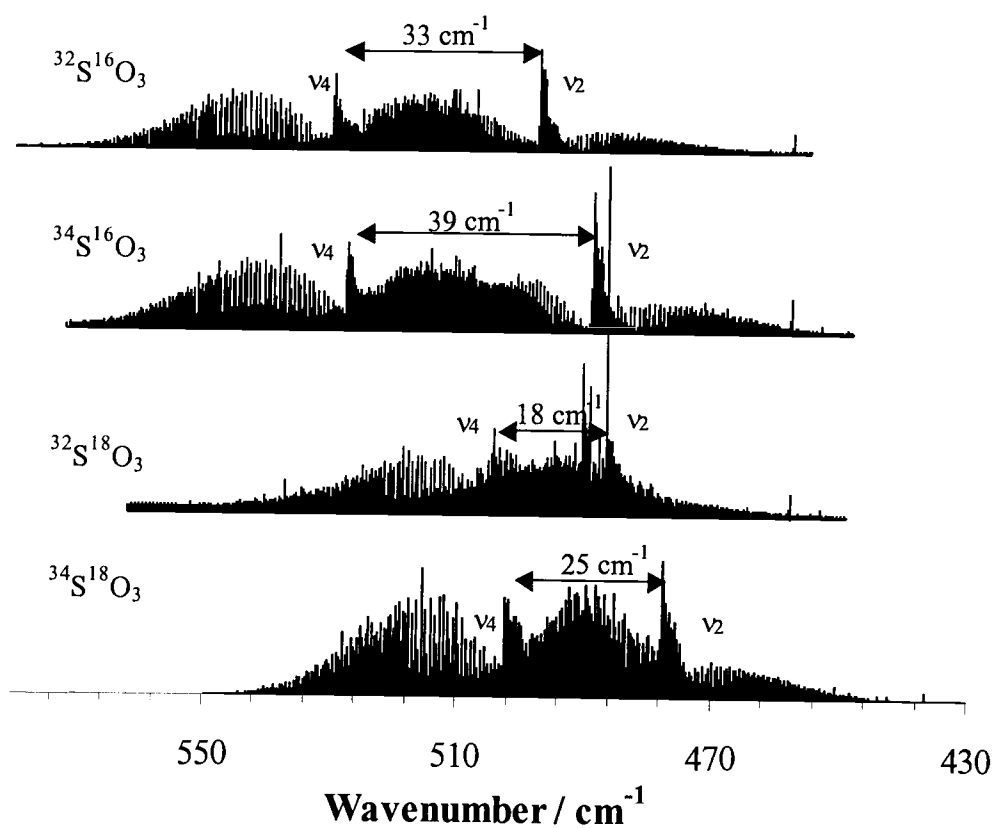


Fig. 2.7 The experimental infrared spectra of the ν_2 , ν_4 region for all of the isotopomers of SO_3 studied. The values shown above each spectrum indicate the approximate energy difference between the band origins of ν_2 and ν_4 .

structure of each mode is apparent. It should be noted that the $\nu_4-\nu_2$ difference is much less for the ^{18}O forms, a feature which results in some extensive mixing between these modes, mixing that made the spectral analysis more difficult than in the ^{16}O cases. The actual data analyzed in this work is identified by file name in Table 2.1. Additional scans were taken to confirm reproducibility but the key files subject to analysis are listed there. In the case of the CARS spectra, we note that composite spectra, formed by the addition of 2 scans, were used in the displays of Figs. 2.3 and 2.4 and in later figures comparing observed and calculated CARS spectra.

2.4 Analysis

2.4.1 Energy Level Expression for the Ground State

A detailed discussion of the Hamiltonian form for an oblate symmetric top, including all the subtle interaction terms important in our analysis is provided in the thesis of Jeffrey Barber (15) and, to some extent in references (2-5). This theory is also given in Papousek (16) and in other texts on spectroscopy. Here, we will simply give the final forms for each of the diagonal and off-diagonal interaction terms used in fitting all the transitions assigned in this work. The actual least square fitting procedure was performed using the symrot65E program, adapted from a version written by Dr. Arthur Maki.

Table 2.1
Data Files Used in the Analysis of $^{32}\text{S}^{18}\text{O}_3$ and $^{34}\text{S}^{18}\text{O}_3$.

CARS files		$^{32}\text{S}^{18}\text{O}_3$	$^{34}\text{S}^{18}\text{O}_3$
	Raw data	32S18O3_5 32S18O3_6	34S18Od 34S18Oy
	Composite	28composite.xls	48composite.xls
FTIR files	Spectra	S18O3BOL.D2	34S18O3W.D1
	Bruker peak picked files	S18O3BOL.TB2	S18O3W1.TBL
Fitted lines with parameters	Data	28data.txt	48data.txt
	Results	28res.txt	48res.txt

The standard expression describing the rotational levels of a nondegenerate vibrational state of quantum number v is

$$\begin{aligned}
 F_v(J,K) = & B_v J(J+1) + (C_v - B_v)K^2 - D_v^J J^2(J+1)^2 - D_v^{JK} J(J+1)K^2 - D_v^K K^4 \\
 & + H_v^J J^3 (J+1)^3 + H_v^{JK} J^2(J+1)^2 K^2 + H_v^{KJ} J(J+1) K^4 + H_v^K K^6 \\
 & \pm \text{splitting terms.}
 \end{aligned}
 \tag{1}$$

Here the rotational constants are given by

$$B_v = B_e - \sum_i \alpha_i^B (v_i + \frac{1}{2}d_i) + \sum_{ij} \gamma_{ij}^B (v_i + \frac{1}{2}d_i)(v_j + \frac{1}{2}d_j),
 \tag{2}$$

with a similar expression describing the rotational constant C_v .

For the ground state, the only rotational level splitting term that proved significant was for $K=3$ and this is given by the expression

$$\pm \delta_{3K} \Delta_0 [J(J+1)][J(J+1)-2][J(J+1) - 6],$$

where Δ_0 describes the splitting parameter. The sign convention for the splitting terms here and elsewhere is that the upper sign is used for even J values and the lower for odd J values, unless otherwise specified. Also, the convention used above and throughout this work is that upper case K is an unsigned quantum number while lower case k and l are signed quantum numbers.

The C -rotational constant for the ground state was determinable only in the case of $^{32}\text{S}^{16}\text{O}_3$ (2, 3) where microwave data of centrifugally-distorted $^{32}\text{S}^{16}\text{O}_3$ was available. Consequently, the C -rotational constants for both $^{32}\text{S}^{18}\text{O}_3$ and $^{34}\text{S}^{18}\text{O}_3$ isotopes were estimated using the planarity condition ($I_C = 2I_B$) but adjusted by the

inertial defect determined in $^{32}\text{S}^{16}\text{O}_3$, scaled by the magnitude of the B -rotational constants. This results in the following expression for the isotopic C' value

$$\frac{1}{C'} - \frac{1}{B'} = \left(\frac{1}{C} - \frac{2}{B} \right) \frac{B'}{B}. \quad [3]$$

The D_k and H_k terms were also not determinable for $^{32}\text{S}^{18}\text{O}_3$ and $^{34}\text{S}^{18}\text{O}_3$ and were estimated as follows. D_k was calculated using the planarity relation

$$D_K = -(2D_J + 3D_{JK})/4 \quad [4]$$

This approximation was confirmed to be valid for the $^{32}\text{S}^{16}\text{O}_3$ isotope where D_K was determinable; hence this assumption is considered reasonable. For H_K , the planarity condition

$$H_K = -(3H_J + 4H_{JK} + 5H_{KJ})/6 \quad [5]$$

was considered less reliable and the H_K for each isotopomer was taken to be $H_K(B'/B)^3$. It is important to note that the actual values of C_0 , D_K and H_K do not actually appear in the expressions for any of the infrared or Raman transitions. The above estimates were made only for purposes of calculating line intensities, for which purpose they are more than adequate.

2.4.2 ν_2 , ν_4

Due to a strong Coriolis interaction that couples the (010^00^0) and (000^01^1) states, the ν_2 , ν_4 band analyses must be done concurrently. As in our earlier treatment of both $^{32}\text{S}^{16}\text{O}_3$ and $^{34}\text{S}^{16}\text{O}_3$, a 3×3 energy matrix of the form

$$\begin{array}{c}
 | \psi_{4+} \rangle \quad | \psi_2 \rangle \quad | \psi_{4-} \rangle \\
 \left| \begin{array}{ccc}
 E_1 & W_{1,1} & W_{2,2} \\
 W_{1,1} & E_2 & W_{1,1} \\
 W_{2,2} & W_{1,1} & E_3
 \end{array} \right|
 \end{array}$$

was used to describe the allowed interaction between ν_2 , ν_4 states with common J and $k-l$ values. In this matrix $E_1 = E(\nu_4, J, k \pm 1, l_4 \pm 1)$, $E_2 = E(\nu_2, J, k, l_4 = 0)$, $E_3 = E(\nu_4, J, k \mp 1, l_4 \mp 1)$ and $E(\nu, J, k, l) = G(\nu, l) + F_{11}(J, K)$ or $F_{\perp}(J, k, l)$. The choice of zero energy is somewhat arbitrary and we have chosen to use the common convention that defines the $J=K=0$ level of the ground state as the minimum energy reference. The vibrational band centers are then defined as differences of vibrational G terms,

$$\nu_0 = G(\nu, l) - G(0, 0) \quad [6]$$

The rotational term level expression $F_{11}(J, K)$ for $\nu_2 A'_2$ levels is the same as that for the ground state [1] with the addition of a $\Delta_\nu = \Delta_2 K=3$ splitting term with sign convention opposite to that in the A'_1 ground state. For the ν_4 vibration, $F_{\perp}(J, k, l)$ is used and is given by

$$\begin{aligned}
 F_{\perp}(J, k, l) = & F_{\nu}(J, K) - 2(C\zeta)_{\nu} kl + \eta_{\nu}^J J(J+1)kl + \eta_{\nu}^K k^3 l \\
 & \pm \delta_{2K} t_{\nu} [J(J+1)][J(J+1)-2].
 \end{aligned} \quad [7]$$

Here, t_{ν} is an added splitting term found to be important for the $K = 2$ levels. The $C\zeta$ term, with its centrifugal distortion corrections, corresponds to an energy term

derived from plus and minus combinations of vibrational and rotational angular momentum components.

The strong Coriolis interaction that couples the ν_2 and ν_4 vibrational states to each other is defined as

$$\begin{aligned} W_{1,1} &= \langle \nu_2, \nu_4, J, k \pm 1, l_4 \pm 1 | H | \nu_2 + 1, \nu_4 - 1, J, k, l_4 \rangle \\ &= \pm [(B\zeta_{2,4}) + z_{2,4J} J(J+1) + z_{2,4K} k(k \pm 1)] [(v_2 + 1)(v_4 \pm l_4 + 1)]^{1/2} [J(J+1) - k(k \pm 1)]^{1/2}. \end{aligned} \quad [8]$$

According to Jahn's rule (17), this interaction only occurs if the symmetry species product of two levels (e.g. $A_2'' \times E' = E''$) is the same as a rotational symmetry species (e.g. A_2' and E''). This ν_2, ν_4 interaction is thus allowed and has proven quite important, producing significant frequency and intensity perturbations in the spectra. The subscript notation used for the $W_{1,1}$ matrix element implies that $|\Delta k|$ and $|\Delta l| = 1$.

Finally, we note that the degenerate levels of ν_4 ($l_4 = \pm 1$) are also Coriolis coupled to each other via an l -type resonance, for which the off-diagonal matrix element is

$$\begin{aligned} W_{2,2} &= \langle \nu_4, J, k, l_4 | H | \nu_4, J, k \pm 2, l_4 \pm 2 \rangle = \frac{1}{4} [q_4 + q_4^J J(J+1) + q_4^{JJ} J^2(J+1)^2] \\ &\quad \times [(v_4 + 1)^2 - (l_4 \pm 1)^2]^{1/2} [J(J+1) - k(k \pm 1)]^{1/2} [J(J+1) - (k \pm 1)(k \pm 2)]^{1/2}. \end{aligned} \quad [9]$$

2.4.3 Energy Levels for $\nu_1, 2\nu_2, \nu_2 + \nu_4$ and $2\nu_4$ States

As described below, these states are all coupled in SO_3 and none of them are seen directly by infrared transitions from the ground state. However, mixed levels

can be accessed via infrared hot bands that originate from ν_2 and ν_4 levels populated thermally at room temperature. In particular, we have observed transitions denoted as $2\nu_2-\nu_2$ ($020^00^0-010^00^0$), $\nu_2 + \nu_4 - \nu_2$ ($010^01^1-010^00^0$), $\nu_2 + \nu_4 - \nu_4$ ($010^01^1-000^01^1$), $2\nu_4(l=0) - \nu_4(l=1)$ ($000^02^0-000^01^1$) and $2\nu_4(l=2) - \nu_4(l=1)$ ($000^02^2-000^01^1$). The mode/level appearing at the right in this notation for the hot bands denotes the vibrational level from which the hot band originates. Together, with the ν_1 (100^00^0) level, the upper levels form the diagonal elements of a 7×7 Hamiltonian matrix (Table 2.2) that was required to take into account all of the possible interactions that take place between these states. It is only states with common J and $k-l$ quantum values that mix, so a few states with low J and K values might not always produce the full 7×7 matrix. For example, ν_1 , $2\nu_2$ and $2\nu_4(l=0)$ have $K=0$, $J=0$ transitions that cannot couple with either $2\nu_4(l=2)$ or $\nu_2+\nu_4(l=1)$ states since $J \geq l$ so that $J=0$ does not exist for the latter. The matrix is thus, in this case, reduced to a 3×3 .

The diagonal elements of the matrix are composed of combinations of energy terms (Eq. 1-7) corresponding to the fundamental vibrations from which they are composed. Coriolis interactions between and within states apply also to the hot bands. For example, $2\nu_2$ and $\nu_2+\nu_4-\nu_2$ both originate from ν_2 and have ν_2 and ν_4 components that couple through an $W_{1,1}$ Coriolis interaction.

In addition, Fermi resonances couple states that possess the same symmetry and this interaction is of increasing importance when the states have similar energies. For a molecule of D_{3h} symmetry, both $2\nu_2$ and $2\nu_4(l=0)$ have the correct symmetry

Table 2.2
The 7×7 Hamiltonian Matrix Describing Possible Interactions with v_1 States

$E(v_1, k, 0)$	W_{144}	W_{122}	0	0	0	0
W_{144}	$E(2v_4, k, 0)$	0	$W_{2,2}$	$W_{2,2}$	$W_{1,1}$	$W_{1,1}$
W_{122}	0	$E(2v_2, k, 0)$	0	0	$W_{1,1}$	$W_{1,1}$
0	$W_{2,2}$	0	$E(2v_4, k+2, 2)$	$W_{4,4}$	$W_{1,1}$	0
0	$W_{2,2}$	0	$W_{4,4}$	$E(2v_4, k-2, -2)$	0	$W_{1,1}$
0	$W_{1,1}$	$W_{1,1}$	$W_{1,1}$	0	$E(v_2+v_4, k+1, 1)$	$W_{2,2}$
0	$W_{1,1}$	$W_{1,1}$	0	$W_{1,1}$	$W_{2,2}$	$E(v_2+v_4, k-1, -1)$

(a_1) to interact with ν_1 . The Fermi resonance term describing the interaction between ν_1 and $2\nu_2$ is given by

$$W_{122} = \langle \nu_1, \nu_2, J, k, l | H | \nu_1 + 1, \nu_2 - 2, J, k, l \rangle = k_{122} + k'_{122} J(J + 1), \quad [10]$$

while interaction with $2\nu_4(l = 0)$ is described by

$$W_{144} = \langle \nu_1, \nu_4, J, k, l | H | \nu_1 + 1, \nu_4 - 2, J, k, l \rangle = k_{144} + k'_{144} J(J + 1) + k^K_{144} k^2. \quad [11]$$

Here, k_{122} and k_{144} are the cubic anharmonic terms that serve to mix the respective coordinates. The effect of neglecting these Fermi resonance terms on the CARS spectra of $^{32}\text{S}^{16}\text{O}_3$ and $^{34}\text{S}^{16}\text{O}_3$ (3, 5) has been explored and shown to be very significant. Similarly, these terms, along with all of the other interactions shown in the interaction matrix prove important for the analysis of the $^{32}\text{S}^{18}\text{O}_3$ and $^{34}\text{S}^{18}\text{O}_3$ spectra studied here.

In analyzing the spectral data, transitions were assigned for all of the infrared bands mentioned earlier and for the vibrational fundamental ν_3 and its overtone, $2\nu_3$. The analysis of these two latter bands for all of the SO_3 isotopes is the subject of another publication (6). The ν_3 levels were not found to couple to any other level, but the least-squares analysis was performed on the entire data set in order to obtain an optimal set of rovibrational constants and for consistency with the analysis of the other isotopes. The ν_2 , ν_4 fundamental bands were fit first and the parameters deduced greatly aided the subsequent analysis of the hot bands. In the case of $^{32}\text{S}^{16}\text{O}_3$, over 11,000 transitions were assigned, more than for any other isotopomer.

As a consequence, some higher order constants were determinable in that isotopomer, but not in others. Where necessary, we have used the $^{32}\text{S}^{16}\text{O}_3$ constants to estimate some of the smaller, undetermined parameters. As it happens, the spectral data obtained for $^{34}\text{S}^{18}\text{O}_3$ were significantly better than for $^{32}\text{S}^{18}\text{O}_3$ where there was a higher concentration of mixed 16-18 forms of SO_3 , thus we present the analysis for $^{34}\text{S}^{18}\text{O}_3$ first.

2.5 Vibration-Rotation Constants for $^{34}\text{S}^{18}\text{O}_3$

2.5.1 Ground State

The ground state constants for $^{34}\text{S}^{18}\text{O}_3$ are given in Table 2.3. Of the 8082 transitions analyzed, 6132 originated directly from the ground state. In comparison with previously published results, specifically $^{34}\text{S}^{16}\text{O}_3$ (4), substitution of ^{16}O with ^{18}O should have the effect of increasing the moment of inertia and thus decreasing the magnitude of the rotational constants. One approximation for estimating the ground state constants from other isotopic data is that the scaling of the ground state constants goes as the ratio $(^{16}\text{O}/^{18}\text{O})^x$ where x is 1 for B_0 , 2 for the D centrifugal distortion terms, and 3 for the H -terms. Indeed, the ratio of the B_0 constant of $^{34}\text{S}^{16}\text{O}_3$ to $^{34}\text{S}^{18}\text{O}_3$ agrees with this within a difference of only 0.014%. The centrifugal terms were also consistent with this prediction, being only slightly larger by 0.23% and 0.12% for D_J and D_{JK} , respectively. This simple scaling approximation is expected to be less precise for the H -terms and the calculated

TABLE 2.3
Ground-State Rotational Constants
in cm^{-1} for $^{34}\text{S}^{18}\text{O}_3$

C_0	0.154 668 79 ^a
B_0	0.309 785 63(36) ^b
$D_J \times 10^7$	2.461 0(20)
$D_{JK} \times 10^7$	-4.342 6(42)
$D_K \times 10^7$	-2.026 ^c
$H_J \times 10^{12}$	0.655(34)
$H_{JK} \times 10^{12}$	-2.124(89)
$H_{KJ} \times 10^{12}$	-2.367(68)
$H_K \times 10^{12}$	-0.895 ^d
$\Delta_0 \times 10^{14}$	-0.700

^a The value of C_0 was calculated from that in $^{32}\text{S}^{16}\text{O}_3$ as described in the text.

^b The uncertainties are two standard deviations. They refer to the last digits and are shown in parentheses.

^c The value of D_k was calculated using the planarity condition.

^d The value of H_k was calculated by multiplying H_k of $^{32}\text{S}^{16}\text{O}_3$ by the cube of the ratio of the B values for $^{34}\text{S}^{18}\text{O}_3/^{32}\text{S}^{16}\text{O}_3$

values were consistently larger than the predicted values; up to 26% larger for the H_J term.

2.5.2 ν_2 and ν_4 Parameters

The parameters for the ν_2 and ν_4 states, along with those of the upper levels of the hot bands, are shown in Table 2.4. With both heavier sulfur and oxygen atoms moving, the fundamental frequencies of the vibrations are, as expected, lower than those for either $^{32}\text{S}^{16}\text{O}_3$ or $^{34}\text{S}^{16}\text{O}_3$. Martin's predicted *ab initio* values (18) for the band origins of $^{34}\text{S}^{18}\text{O}_3$ are 478.5 cm^{-1} for ν_2 and 500.2 cm^{-1} for ν_4 , both extremely close to the experimental values of 477.5 cm^{-1} and 502.1 cm^{-1} . In the harmonic approximation, the ratio of the band center locations for the ν_2 out-of-plane bend scales as the square root of the ratio of the G-matrix element, $G_{22} = 9(1/M_O + 3/M_S)/(4r^2)$. The experimental ν_2 ratios for $^{34}\text{S}^{18}\text{O}_3/^{32}\text{S}^{16}\text{O}_3$ and $^{34}\text{S}^{18}\text{O}_3/^{34}\text{S}^{16}\text{O}_3$ are 0.9597 and 0.9769, in very good accord with the calculated G-matrix ratios of 0.9593 and 0.9767. In a similar way, the so-called Product Rule (19) predicts that the ν_3 , ν_4 product will scale as the square root of the mass ratio of $1/M_O (3/M_S + 1/M_O)$. The products of the ν_3 and ν_4 vibrations give isotopomer ratios of 0.9053 and 0.9214, also in good agreement with calculated values of 0.9043 and 0.9207. Though the assignments are not really in doubt here, such close comparisons confirm that the bands are correctly assigned, and also that the harmonic model is quite good in characterizing the motions in SO_3 .

TABLE 2.4

The Rovibrational Constants in cm^{-1} for the ν_2, ν_4 States for the Fundamentals and Hot Bands of $^{34}\text{S}^{18}\text{O}_3$

constant	ν_2	$2\nu_2$	$\nu_2+\nu_4$	ν_4	$2\nu_4(l=0)$	$2\nu_4(l=2)$
ν_0	477.508 651(46) ^a	954.900(27)	979.782 012(67)	502.055 613(36)	1003.791 6(26)	1004.365 841(80)
$\Delta C^b \times 10^3$	0.109 20(14)	0.216 58(72)	-0.018 70(41)	-0.127 927(79)	-0.256 69(20)	{-0.256 69} ^c
$\Delta B \times 10^3$	0.653(14)	1.211(51)	0.579(13)	-0.048 0(72)	-0.051(26)	{-0.051}
$\Delta D_J \times 10^{10}$	10.8(11)	14.3(36)	27.5(22)	8.53(81)	10.9(24)	{10.9}
$\Delta D_{JK} \times 10^{10}$	-16.0(24)	[-31.9] ^d	[-43.0]	-27.1(16)	-48.4(46)	{-48.4}
$\Delta D_K \times 10^{10}$	6.3(17)	19.9(45)	17.1(24)	18.8(10)	38.3(30)	{38.3}
$\Delta H_J \times 10^{13}$	-1.03(18)	[-2.05]	[-0.65]	0.38(15)	[0.76]	[0.76]
$\Delta H_{JK} \times 10^{13}$	2.93(56)	[5.87]	[1.86]	-1.07(44)	[-2.14]	[-2.14]
$\Delta H_{KJ} \times 10^{13}$	-3.32(72)	[-6.63]	[-2.09]	1.23(58)	[2.46]	[2.46]
$\Delta H_K \times 10^{13}$	1.45(32)	[2.89]	[0.90]	-0.55(27)	[-1.1]	[-1.1]
$(C\zeta_4)$			-0.078 146(19)	-0.078 425 6(33)		-0.078 297 2(60)
$\eta_J \times 10^7$			-4.73(63)	-6.30(48)		-4.89(84)
$\eta_K \times 10^7$			4.42(62)	6.01(47)		4.61(83)
$q \times 10^4$			3.11(26)	3.63(14)	3.13(25)	
$(B\zeta_{2,4})$			0.170 64(46) ^e	0.171 24(26)	0.170 80(47) ^f	
$z_{2,4J} \times 10^7$			-3.36(16) ^e	-3.797(87)	-3.65(15) ^f	
$z_{2,4K} \times 10^7$			2.719(88) ^e	2.738(50)	2.97(11) ^f	
$Q_4 \times 10^6$						-2.6(1.5)
# of transitions	2039	434	696	3016	203	412

^a The uncertainties are two standard deviations. They refer to the last digits and are shown in parentheses.

^b $\Delta C = C' - C_0$, $\Delta B = B' - B_0$, etc.

^c Constants enclosed in {brackets} were fixed to $2\nu_4(l=0)$ values

^d Constants enclosed in [brackets] were fixed to the appropriate combination of values from the ν_2/ν_4 fundamentals.

^e Contained in the $W_{1,1}$ term for $\nu_2+\nu_4$ interacting with $2\nu_2$.

^f Contained in the $W_{1,1}$ term for $\nu_2+\nu_4$ interacting with $2\nu_4(l=0)$ and $2\nu_4(l=2)$.

The rotational constants for ν_2 change in a predictable manner when this out-of-plane mode is excited. The effect is an increased contribution of a pyramidal configuration to the averaged moments of inertia. In the pyramidal extremes, the oxygen atoms move closer to the symmetry axis, reducing I_C (and I_B) and thereby increasing C' . The differences $\Delta C = C' - C''$ (and $\Delta B = B' - B''$) are therefore positive, as observed. This effect is less for $^{34}\text{S}^{18}\text{O}_3$ compared to $^{34}\text{S}^{16}\text{O}_3$ because the bending amplitude is less for the heavier isotope. Thus the magnitude of the vibration-rotation coupling constants $\alpha_2^B = -\Delta B_2$ and $\alpha_2^C = -\Delta C_2$ are slightly smaller for $^{34}\text{S}^{18}\text{O}_3$.

We note that the magnitude of the Coriolis term $B\zeta_{2,4}$ drops slightly from 0.201 to 0.171 cm^{-1} in going from $^{32}\text{S}^{16}\text{O}_3$ to $^{34}\text{S}^{18}\text{O}_3$, but the frequency and intensity perturbations caused in the spectrum actually increase. This is because of the decreased separation of the band origins between the two interacting states (ν_2 and ν_4), as shown in Fig. 2.7. The effect of the Coriolis perturbation is illustrated in Fig. 2.8 where, for example, neglect of the Coriolis term shifts the predicted value of ${}^R R_{12}(25)$ by 0.055 cm^{-1} . Such shifts made the confident assignments of the transitions difficult and it was only by careful, systematic assignment, calculation, and iteration that the final set of transitions was clearly established.

2.5.3 Hot Bands Involving ν_2 and ν_4

Fig. 2.9 shows the experimental region for ν_2 and ν_4 (top), and the hot bands involving these modes also lie buried within this region. It was noted in our earlier

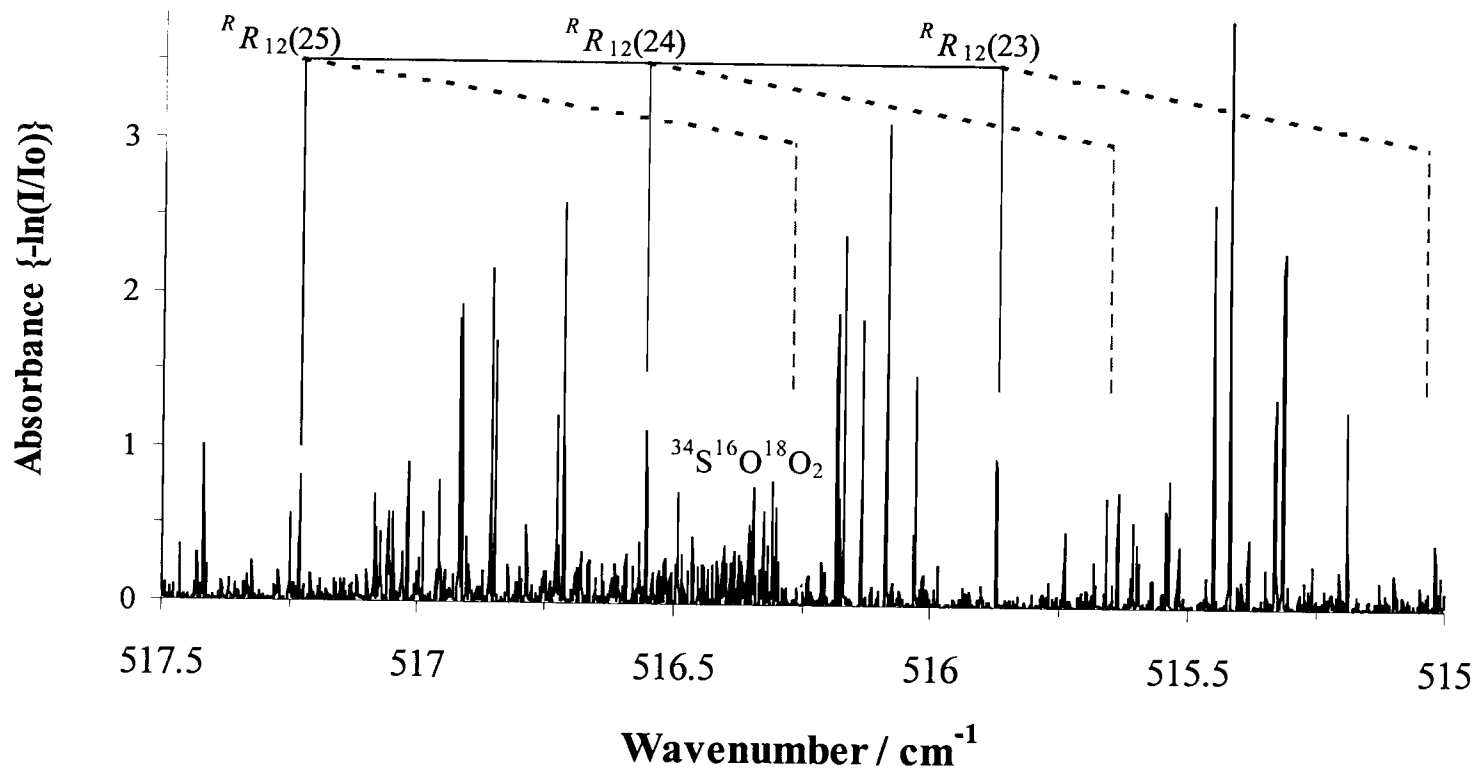


Fig. 2.8 High resolution IR spectrum of ${}^{34}\text{S}{}^{18}\text{O}_3$. The effect of the Coriolis perturbation is demonstrated by the shifting of the predicted line positions in the ${}^R R_{12}(23)$ through ${}^R R_{12}(25)$ sequence. The positions of the transitions have been calculated both with (—) and without (- - -) the Coriolis term. A weak Q -branch sequence near 516.3 cm^{-1} , believed to be due to ${}^{34}\text{S}{}^{16}\text{O}{}^{18}\text{O}_2$ impurity, is also indicated.

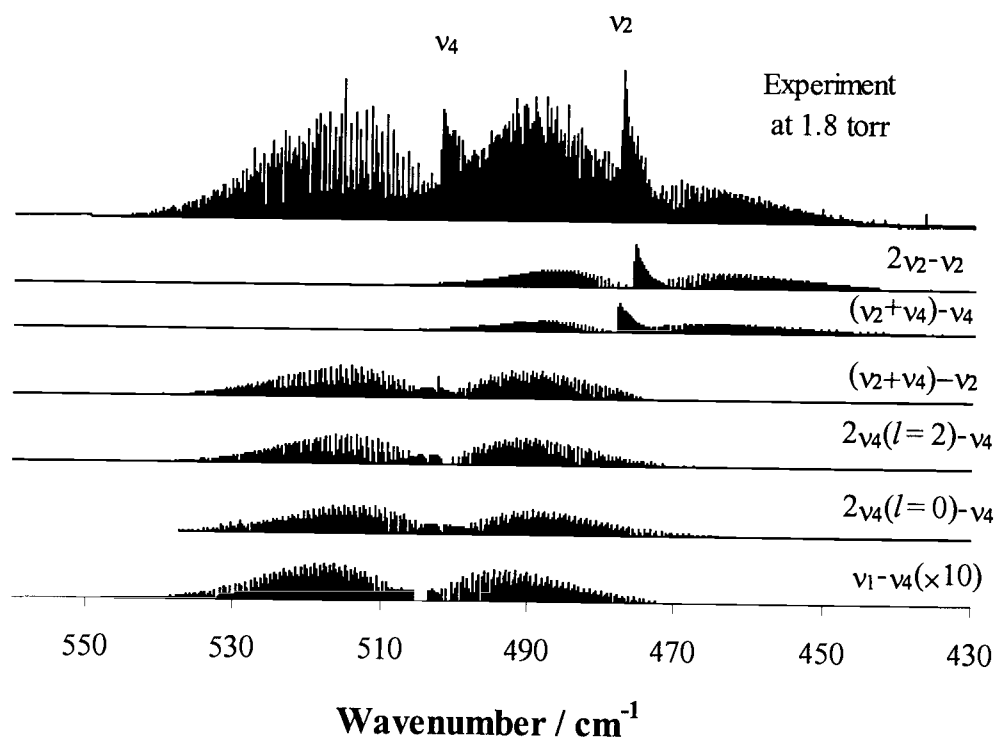


Fig. 2.9 Infrared spectrum of the ν_2 , ν_4 region of $^{34}\text{S}^{18}\text{O}_3$ (top) and calculated spectra of hot bands involving the ν_1 perturbing states. Calculated spectra are approximately at the correct relative intensities.

studies of $^{32}\text{S}^{16}\text{O}_3$ and $^{34}\text{S}^{16}\text{O}_3$ that, to a reasonable degree, the vibration-rotational parameters of overtone levels such as $2\nu_2$ and $2\nu_4$ are very nearly twice those of the fundamentals. This approximation was thus used to obtain an initial guess of parameters used for the fitting of $^{34}\text{S}^{18}\text{O}_3$. In fact, in the final set of parameters displayed in Table 2.4, this approach was used to fix the ΔD_{JK} constants for $\nu_2+\nu_4$ and $2\nu_2$ equal to the appropriate combination of values from the ν_2/ν_4 fundamentals. Another good initial approximation is that the $B\zeta$ constants describing the interactions between $2\nu_2$, $\nu_2+\nu_4$ and $2\nu_4(l=0)$ levels will be very nearly the same as that found for the ν_2 , ν_4 interaction. The $C\zeta$ l -resonance terms are also nearly the same for the ν_4 fundamental and $\nu_2+\nu_4$ and $2\nu_4$ levels.

Small $W_{4,4}$ and Δ_2 terms determined for $^{32}\text{S}^{16}\text{O}_3$ could not be determined for $^{34}\text{S}^{18}\text{O}_3$ but their effect was included by setting them equal to the corresponding values. A $W_{-2,4}$ term did prove necessary and it was found to be slightly smaller than in $^{32}\text{S}^{16}\text{O}_3$ (the forms of these matrix elements $W_{4,4}$ and $W_{-2,4}$ are given in (3)). When all significant terms were determined and the parameters fit, the hot band spectra displayed in the larger panels of Fig. 2.9 resulted. These are scaled with approximately correct intensities and, although not apparent at the scale of the figure, the agreement of the calculated line positions and intensities with the experimental spectra was extremely good. This can be seen by the RMS deviation values of Table 2.4, which are about 10 times smaller than the widths of most lines in the spectrum.

2.5.4 The ν_1 Level Perturbations and Their Effect on the Calculated CARS Spectrum.

The interaction between ν_1 and the hot band of $^{34}\text{S}^{18}\text{O}_3$ can be contrasted with the case found for the previously studied isotopomers, $^{32}\text{S}^{16}\text{O}_3$ and $^{34}\text{S}^{16}\text{O}_3$. For the latter, the position of the pure ($J=0, K=0$) ν_1 vibrational level lies well above those for the $2\nu_4$ states (Fig. 2.10) and, of course, above the $\nu_2+\nu_4$ and $2\nu_2$ states. In particular, the ν_1 interaction with $2\nu_4(l = -2)$ and $2\nu_4(l = 0)$ occurs when either of these latter states approaches a ν_1 level with the same $J, k-l$ value. This occurs mainly at high J and K values. In $^{34}\text{S}^{18}\text{O}_3$, however, ν_1 is very nearly resonant with $2\nu_4(l = 0, \text{ and } -2)$ levels and this has a dramatic effect on the experimental spectrum as shown in Fig. 2.2, where the spectrum has a spread of 6 cm^{-1} compared to less than 1 cm^{-1} for $^{32}\text{S}^{16}\text{O}_3$ and $^{34}\text{S}^{16}\text{O}_3$. The level crossing occurs at lower $J, k-l$ values and the effect of this is the mixing of Raman character into many more of the infrared transitions than in the case of the other isotopomers. This in fact allowed us to assign a number of these as ν_1 - ν_4 hot bands.

The reduced energy diagram displayed for $^{34}\text{S}^{18}\text{O}_3$ in Fig. 2.11 shows the variation of the states with ν_1 as a function of J for different $k-l$ sequences. Energy levels that contain more than 50% character of either ν_1 or $2\nu_4(l = -2, 0 \text{ or } 2)$ are indicated with a particular symbol. Mixed states that do not contain a predominant character have been denoted with a (+) symbol. As the diagram shows there is heavy mixing between all the states. The ν_1 levels, and hence the CARS spectrum, are

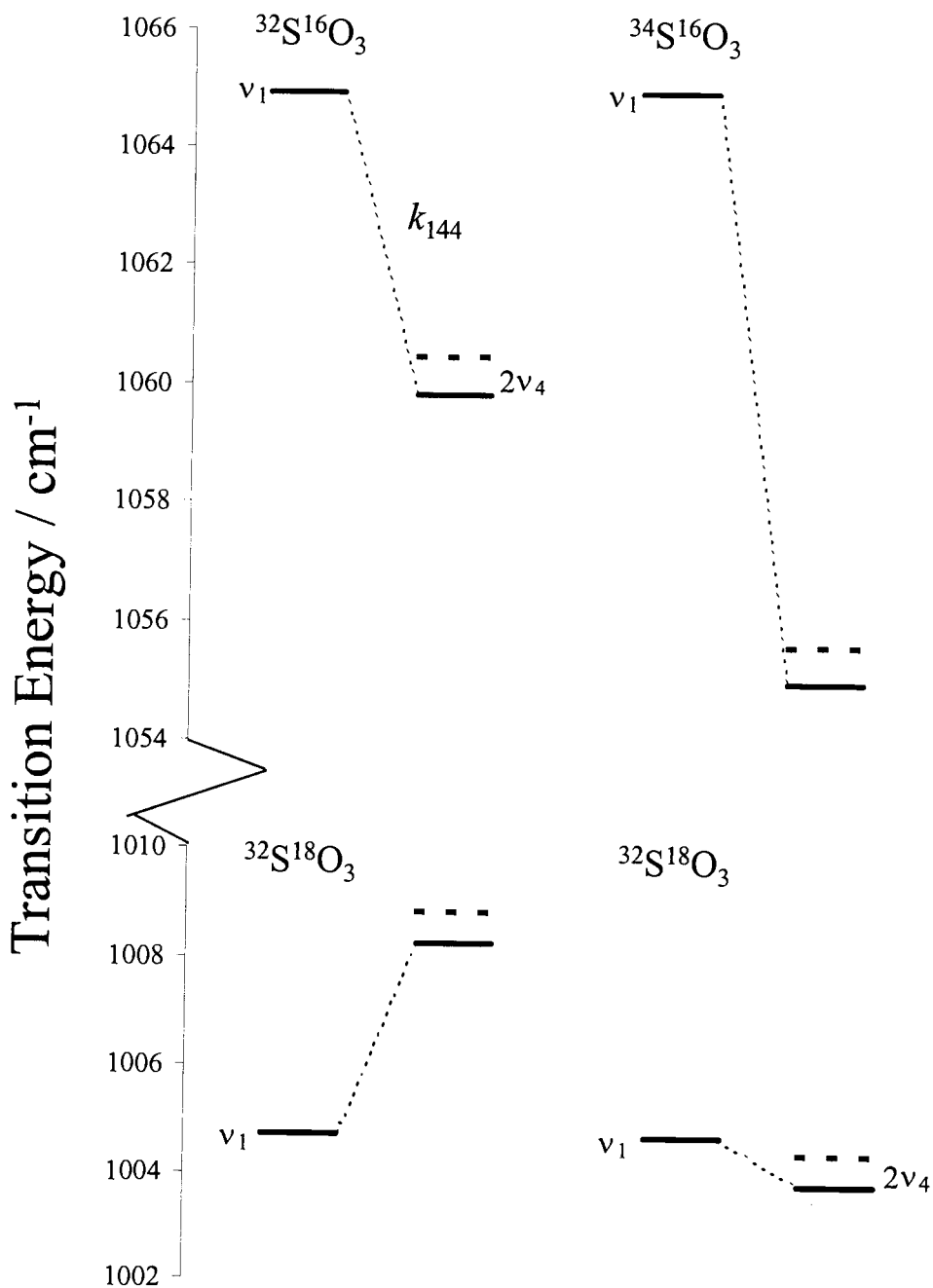


Fig. 2.10 The relative positions of ν_1 and $2\nu_4$ for the isotopomers of SO_3 . The Fermi resonance between ν_1 and $2\nu_4(l=0)$ is indicated. The $2\nu_4(l=\pm 2)$ (---) state does not interact with ν_1 , but does interact with $2\nu_4(l=0)$ through an $W_{2,2}$ interaction (.....).

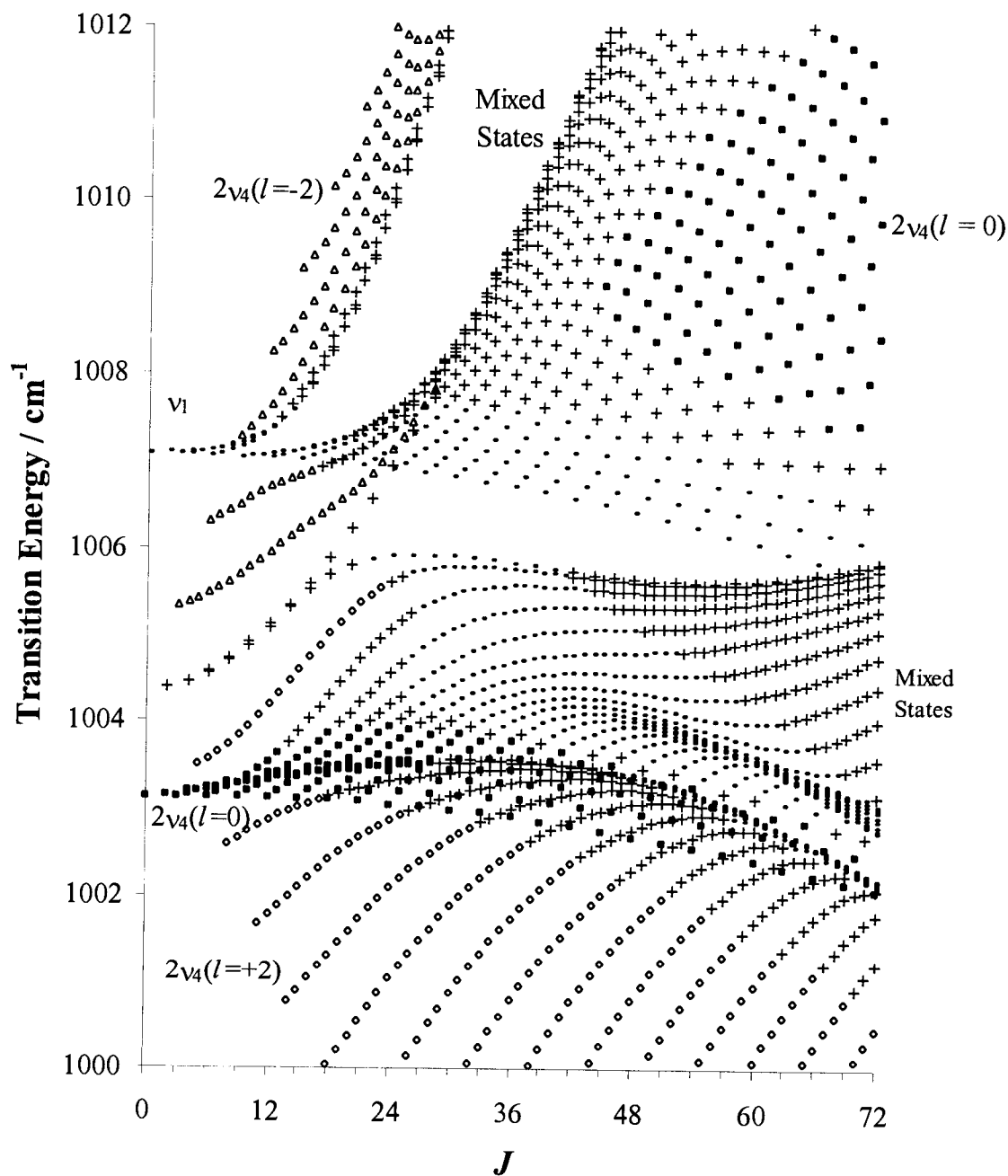


Fig. 2.11 Reduced energy ($E'_{JK} - E''_{JK}$) diagram which corresponds to Q -branch transitions from the ground state of $^{34}\text{S}^{18}\text{O}_3$ to ν_1 and its perturbing states. States identified as ν_1 (-), $2\nu_4(l=-2)$ (\blacktriangle), $2\nu_4(l=0)$ (\blacksquare) and $2\nu_4(l=+2)$ (\diamond) are at least 50% of the identified state. States that do not have any component greater than 50% are denoted as mixed states (+).

essentially split into two regions due to an avoided crossing located around 1006 cm^{-1} .

Fig. 2.12 shows in expanded and rotated form, the effect of the avoided crossings for $k-l = 0, 15$ and 27 levels involving the ν_1 mode. This display mode allows a direct comparison of the ν_1 levels with the calculated and experimental Q -branch CARS spectra shown at the top. It can be seen that the J values for $k-l = 0$ ($J=K, K+1, \dots$) follow a erratic pattern, starting off at 1007.09 cm^{-1} and following a regular progression of increasing energy to 1007.58 cm^{-1} ($J=14$), at which point a jump occurs to $J=22$ at 1005.86 cm^{-1} . The line sequence continues to a band head at 1005.91 cm^{-1} ($J=28$) and then reverses in energy, reaching 1005.76 cm^{-1} for $J=40$. There is then another very large jump down to 1003.39 cm^{-1} for $J=48$. The progressions of many other K series exhibit similar wacky patterns, the result being the very complex pattern seen for ν_1 . As seen here and also in expanded form in Fig. 2.13, when all interactions are properly included, the CARS spectrum calculated from the fitting of only infrared transitions is virtually identical to that observed experimentally.

In fact, the calculated CARS spectrum is extremely sensitive to the choice of the various interaction parameters and to their magnitudes. To illustrate this, we display in Figs. 2.14-2.18 the effect on the calculated CARS spectrum of selectively turning off some of the couplings of the ν_1 levels with the $2\nu_2$, $\nu_2+\nu_4$ and $2\nu_4$ levels. First, in Fig. 2.14, the consequence of turning off the Fermi resonance constants is examined. When both k_{122} and k_{144} couplings are set to zero (d), the Q -branch is

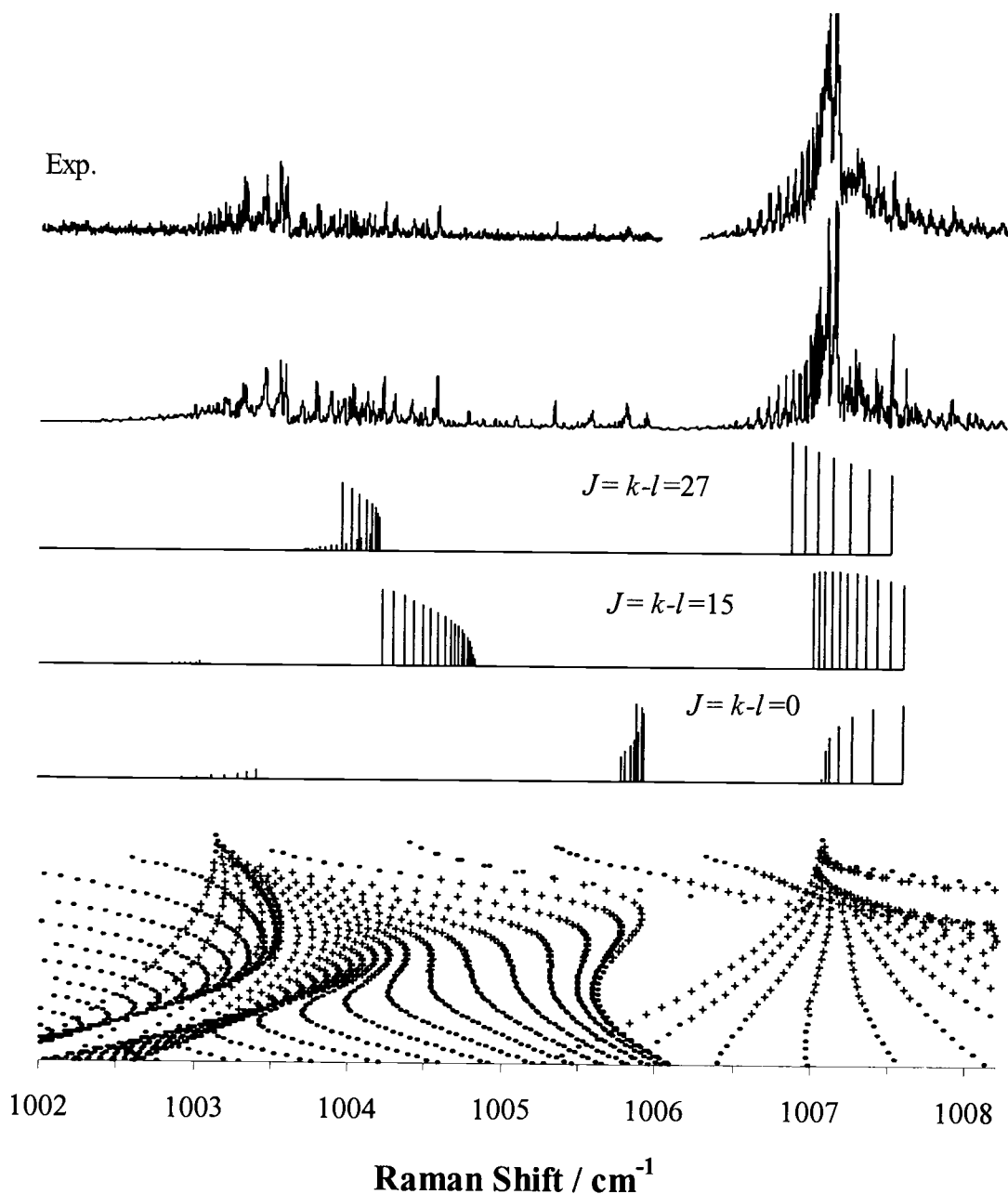


Fig. 2.12 Experimental and calculated CARS spectra for $^{34}\text{S}^{18}\text{O}_3$ (top), along with an expanded view of Fig. 2.11 showing how the level pattern contributes to the appearance of the spectrum. Those v_1 levels contributing 10% or greater of the maximum CARS intensity are designated with a +. Stick spectra for $k-l = 0, 15$ and 27 show the pattern of these subbands to illustrate the jumps that occur in these sequences due to avoided crossings. The start of each sequence ($J = k-l$) is indicated.

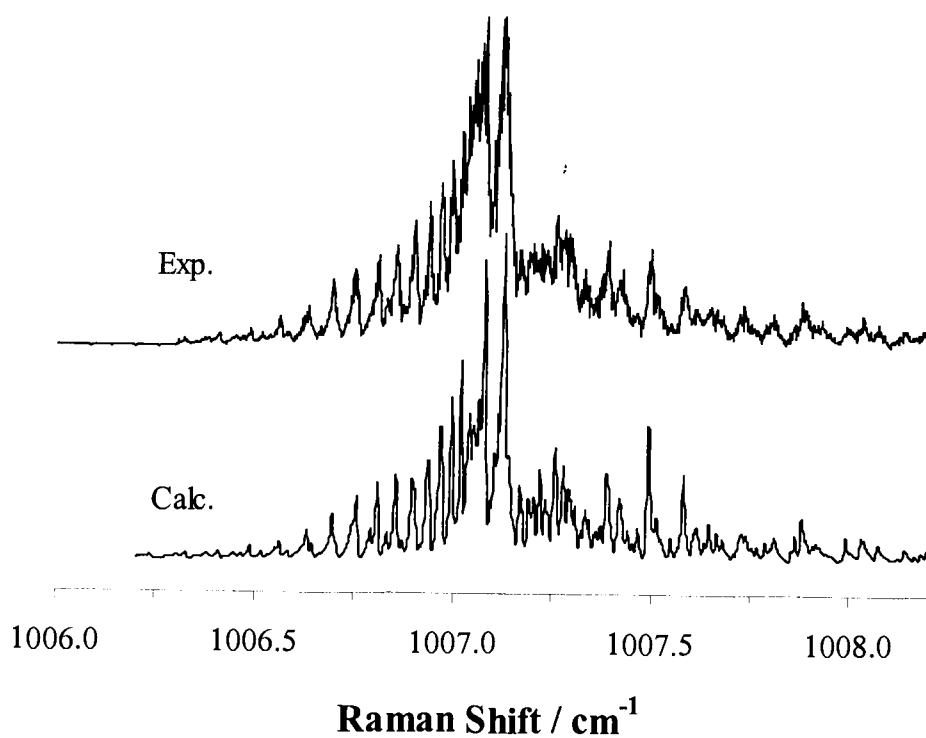
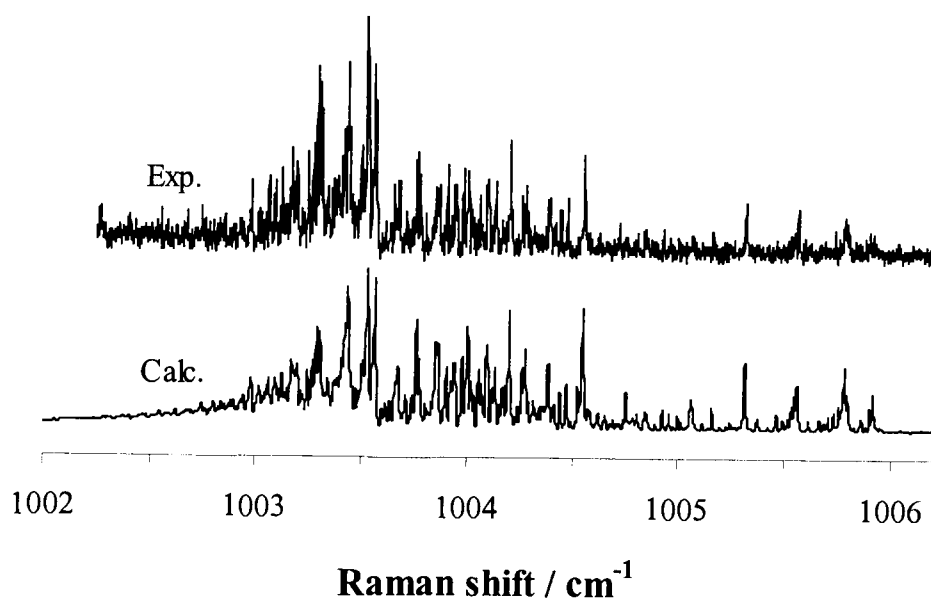


Fig. 2.13 The CARS spectrum of ν_1 of $^{34}\text{S}^{18}\text{O}_3$. The CARS spectrum displayed below the experimental curve are calculated using parameters derived only from infrared hot-band transitions.

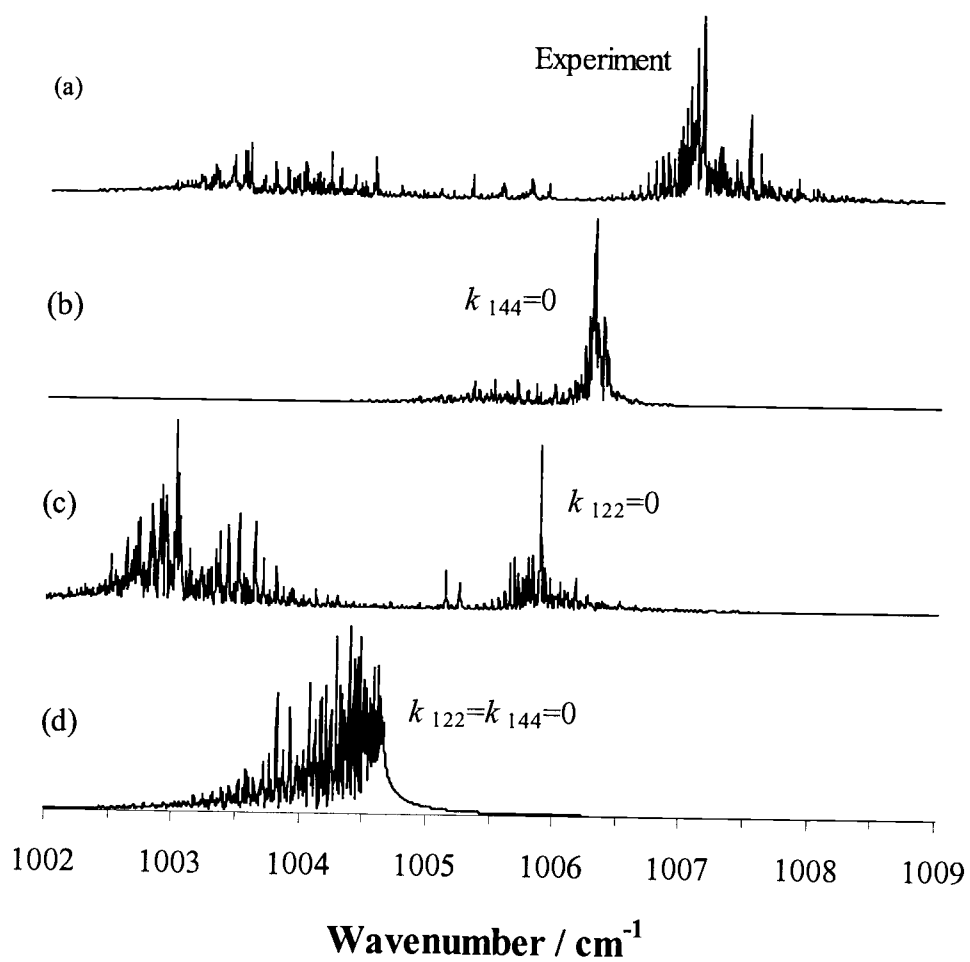


Fig. 2.14 Effect of ν_1 CARS spectrum (a, experimental spectrum) of setting the Fermi resonance constants k_{122} and k_{144} to zero (b-d calculated spectra).

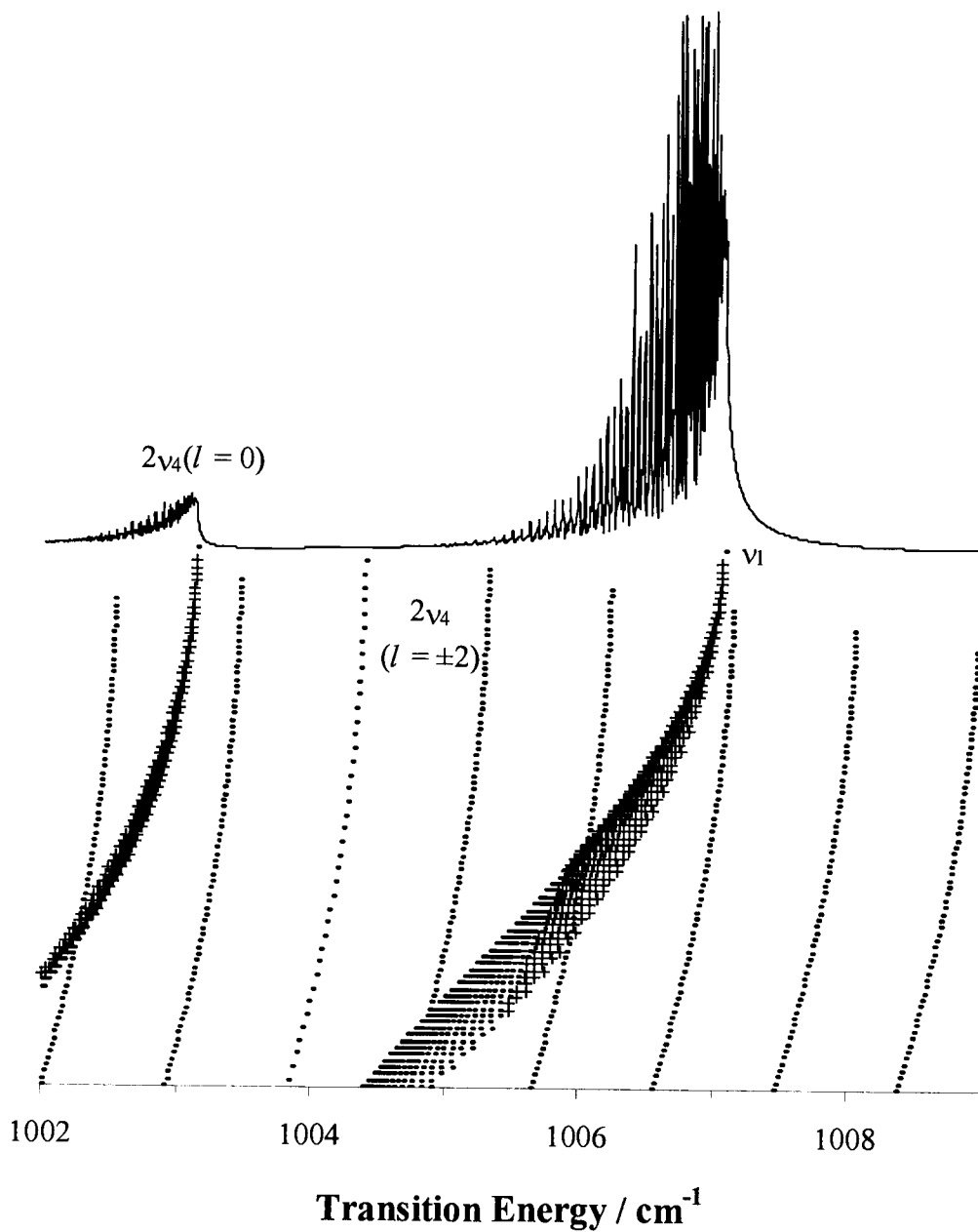


Fig. 2.15 Effect on the ν_1 CARS spectrum (top) and reduced energy diagram (bottom) of setting all $W_{1,1}$ and $W_{2,2}$ interactions to zero but with all Fermi resonance interactions on. Levels with greater than 10% ν_1 character are labeled with a +.

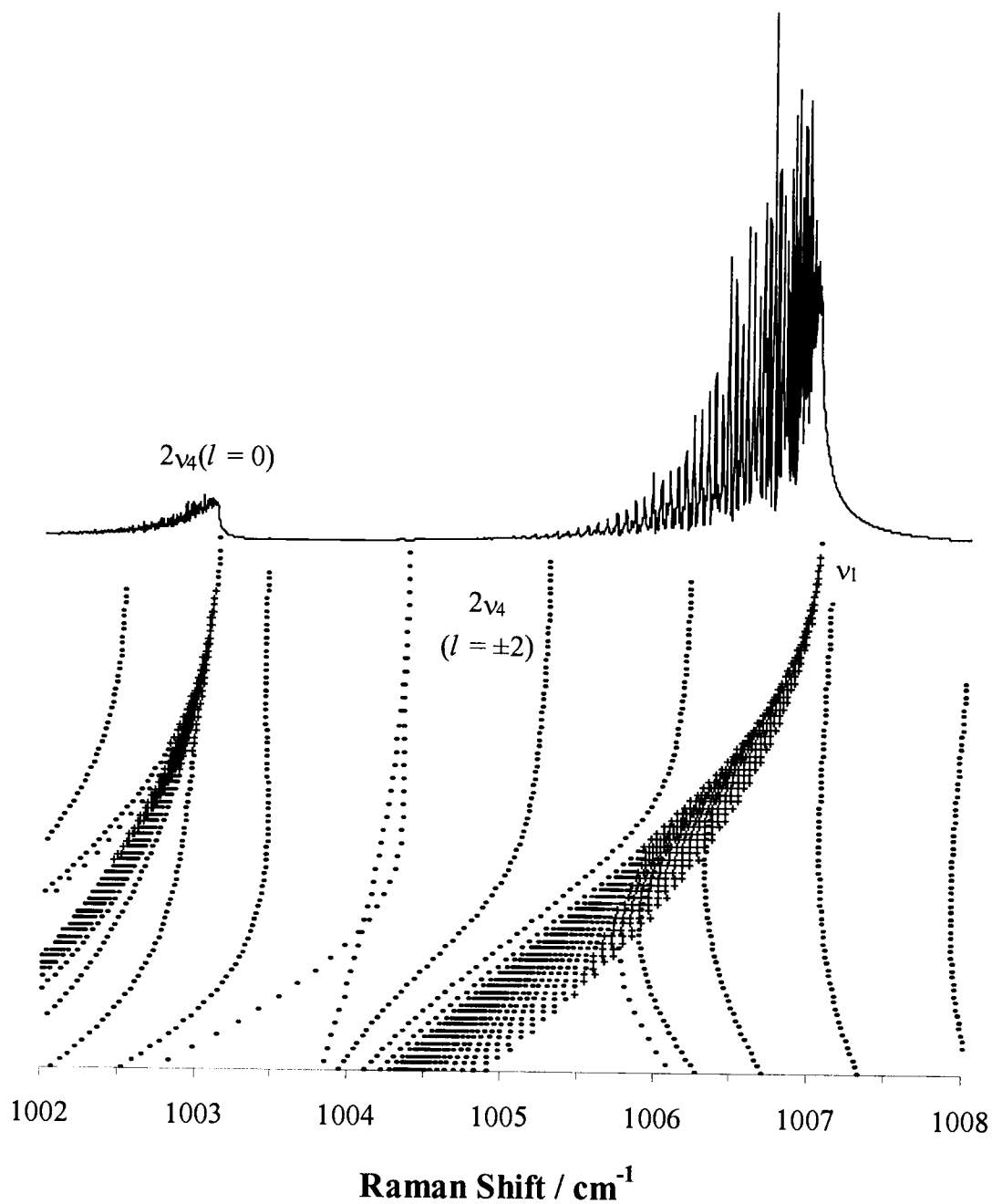


Fig. 2.16 Effect on the ν_1 CARS spectrum (top) and reduced energy diagram (bottom) of setting all $W_{1,1}$ interactions to zero but with $W_{2,2}$ and Fermi resonance interactions on. Levels with greater than 10% ν_1 character are labeled with a +.

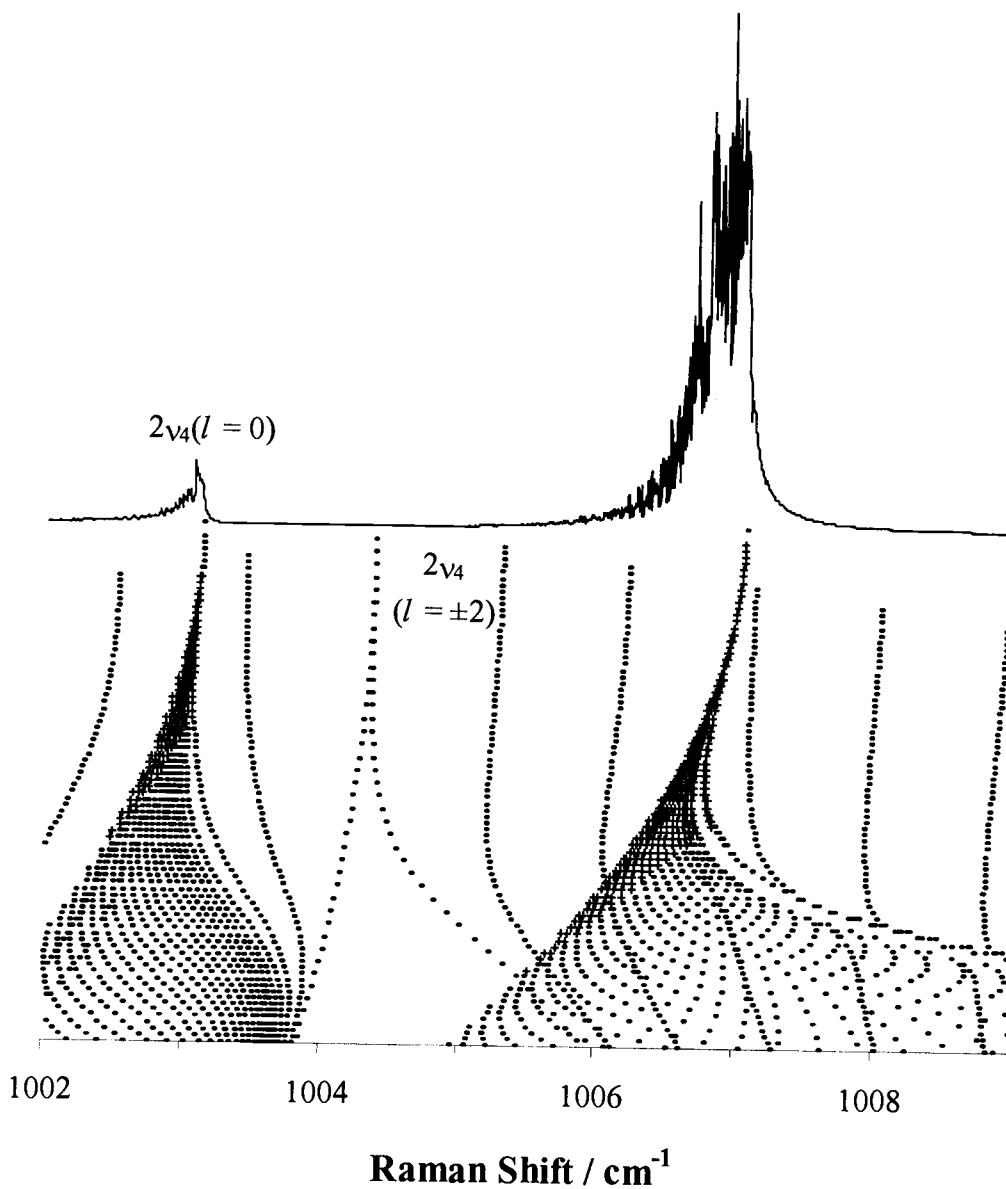


Fig. 2.17 Effect on the ν_1 CARS spectrum (top) and reduced energy diagram (bottom) of setting $W_{1,1}$ for the $\nu_2+\nu_4/2\nu_4$ coupling to zero, but with $W_{2,2}$ and Fermi resonance interactions and $W_{1,1}$ for $\nu_2+\nu_4/2\nu_2$ coupling on. Levels with greater than 10% ν_1 character are labeled with a +.

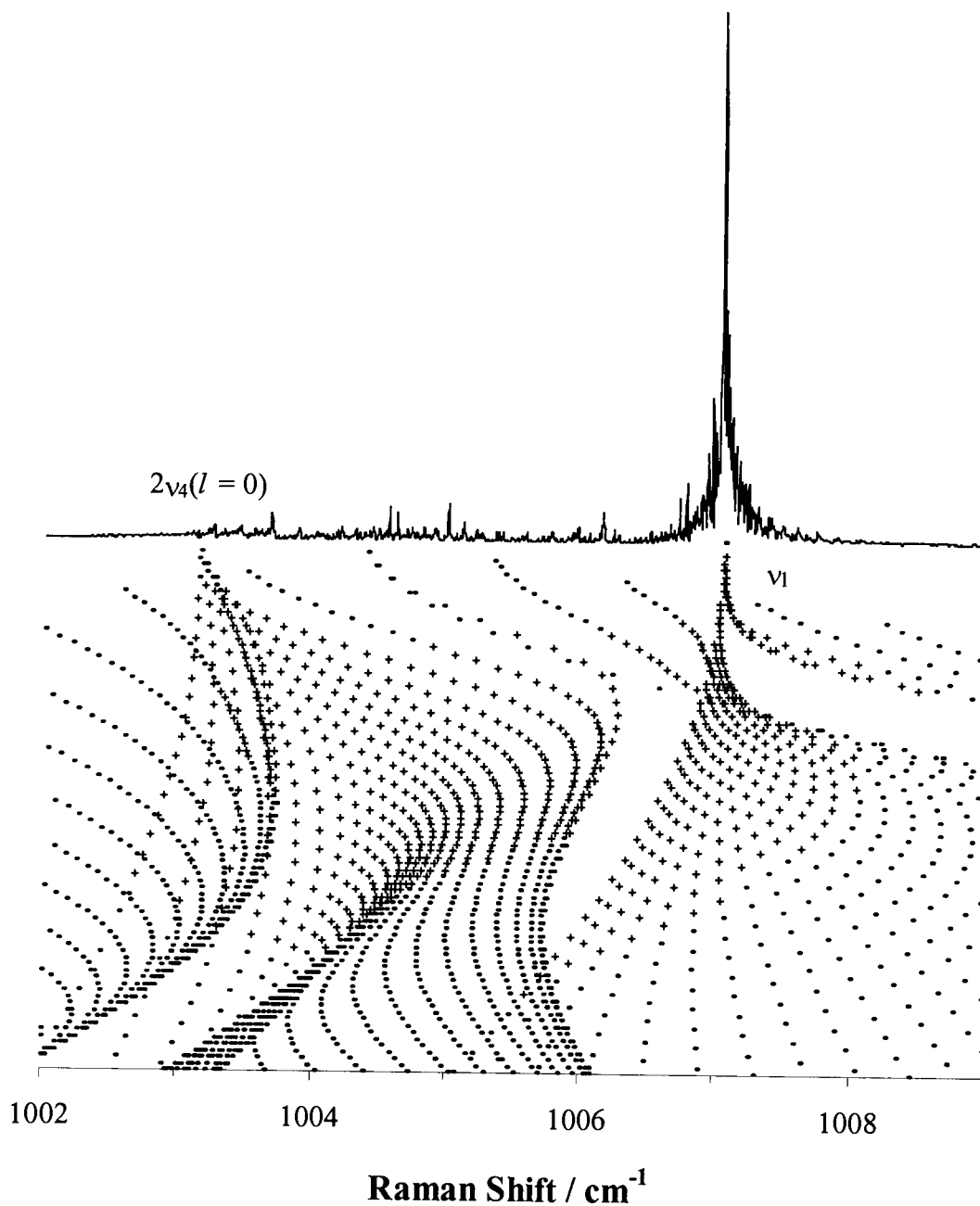


Fig. 2.18 Effect on the ν_1 CARS spectrum (top) and reduced energy diagram (bottom) of setting $W_{1,1}$ for the $\nu_2+\nu_4/2\nu_2$ coupling to zero but with $W_{2,2}$ and Fermi resonance interactions and $W_{1,1}$ for $\nu_2+\nu_4/2\nu_4$ on. Levels with greater than 10% ν_1 character are labeled with a +.

unperturbed and the band origin occurs at the unperturbed ν_1 value of 1004.66 cm^{-1} . When the k_{122} constant is turned on ($k_{144}=0$, panel b), the push from the lower (954.90 cm^{-1}) $2\nu_2$ level raises the ν_1 band by about 1.5 cm^{-1} and the Q -branch structure is altered significantly. In panel c, we show the effect of turning on k_{144} with $k_{122}=0$. Here the band structure is dramatically split into two regions suggesting very strong Fermi mixing of ν_1 and $2\nu_4$. The position and intensities do not match experiment however, and it is only when both Fermi terms are included that agreement is reached between calculated and observed spectra.

We next explore the effect of the more subtle Coriolis interaction terms $W_{1,1}$ and $W_{2,2}$ that couple the ν_2 , $\nu_2+\nu_4$ and $2\nu_4$ levels. The consequence of setting all $W_{1,1}$ and $W_{2,2}$ terms to zero is seen in Fig. 2.15. The result is that the only interaction affecting the ν_1 levels is Fermi resonance, and the appearance of the spectrum is quite similar to that of Fig. 2.14(d) ($k_{122}=k_{144}=0$) except for an overall shift to higher frequency of about 2.4 cm^{-1} due to the push from both $2\nu_4(l=0)$ and $2\nu_2$. Note here the weak lower $2\nu_4(l=0)$ band made visible by intensity borrowing from the ν_1 band. One also sees that the J structure of the $k-l$ levels of $2\nu_4(l=\pm 2)$ is quite regular and does not contribute to the CARS spectrum.

When the W_{22} term is turned on, the $l=\pm 2$ components of $2\nu_4$ couple with the $l=0$ component. However, this interaction is fairly weak, only affecting the $2\nu_4$ energies at high J and K values. The result on ν_1 is minor (Fig. 2.16) since $2\nu_4(l=0)$

is flanked above by $2\nu_4(l = -2)$ and below by $2\nu_4(l = +2)$ so that it is perturbed roughly equally from both.

The effect of turning on the $W_{1,1}$ $\nu_2+\nu_4/2\nu_2$ interaction ($W_{2,2}$ is on, $W_{1,1}$ of $\nu_2+\nu_4/2\nu_4$ is off) is examined in Fig. 2.17 where it is seen to lower the main ν_1 feature by about 1 cm^{-1} . This is because the $W_{1,1}$ coupling that pushes the $\nu_2+\nu_4$ levels up in turn lowers those of $2\nu_2$. The latter are coupled by k_{122} to the ν_1 levels, which thus are lowered in energy, which in turn lowers $2\nu_4(l = 0)$ by about 0.2 cm^{-1} through the k_{144} interaction. The net effect of this indirect "tugging" of the levels is compression of the main Q -branch structure at higher J and K values.

By far, the $W_{1,1}$ interaction between $\nu_2+\nu_4$ and $2\nu_4$ has the greatest effect on the shape of the CARS spectrum as evidenced in Fig. 2.18. In consequence of this interaction, $\nu_2+\nu_4$ is lowered in energy and $2\nu_4$ ($l = 0$ and ± 2) are raised. In fact, some of the $2\nu_4(l = 0)$ J levels now lie higher in energy than the ν_1 levels and push the latter down, resulting in a highly perturbed spectrum. This does not however match the observed spectrum and it is only when all interactions are taken into account that a close match is achieved. Fig. 2.13 shows this in some detail and it is pleasing that the match is so close, considering that only infrared transitions were used in determining the hot bands ν_1 parameters. The vibration-rotation constants deduced for ν_1 are given in Table 2.5.

TABLE 2.5
The Rovibrational Constants in cm^{-1}
for ν_1 of $^{34}\text{S}^{18}\text{O}_3$

ν_0	1004.661(24) ^a	1005.0 ^b
$\Delta C^c \times 10^3$	-0.350 23(86)	
$\Delta B \times 10^3$	-0.706 6(12)	
$\Delta D_J \times 10^{10}$	24(11)	
$\Delta D_{JK} \times 10^{10}$	-48(22)	
$\Delta D_K \times 10^{10}$	24(11)	

^a The uncertainties are two standard deviations. They refer to the last digits and are shown in parentheses.

^b Deperturbed *ab initio* value (Private communication, Ref. 18)

^c $\Delta C = C' - C_0$, $\Delta B = B' - B_0$, etc

2.5.5 ν_1 Parameters

Of the 8082 infrared transitions analyzed, 112 had >50% ν_1 character so the ν_1 parameters are well determined. When the effects of all perturbations is accounted for, the band origin for ν_1 is observed to be 1004.66 cm^{-1} , only slightly higher than a value of 1003.88 cm^{-1} calculated by multiplying the $^{34}\text{S}^{16}\text{O}_3$ value of 1064.92 cm^{-1} by the $(^{16}\text{O}/^{18}\text{O})^{1/2}$ harmonic oscillator ratio. The unperturbed positions of $2\nu_4(l=0)$ and $2\nu_4(l=\pm 2)$ are 1003.79 and 1004.37 cm^{-1} , nearly resonant with ν_1 . This results in the more perturbed ν_1 spectrum for $^{34}\text{S}^{18}\text{O}_3$ compared to the other isotopomers, where the interacting levels are further apart. The ΔB , ΔC values determined here are both negative with $\Delta B \sim 2\Delta C$ as would be expected for an oblate top. The negative sign is reasonable since excitation of the symmetric SO stretch will increase I and hence decrease B . Since the motion of only the oxygen atoms is involved in the ν_1 vibration, the rotational constants should, just as in the ground state, scale to those of $^{34}\text{S}^{16}\text{O}_3$ according to the ratio of the oxygen masses. The approximation comes close, with predictions for ΔC and ΔB being only slightly larger than the observed values, by 5% and 18% respectively. Even an approximation that the ΔD terms scale as $(^{18}\text{O}/^{16}\text{O})^2$ is reasonable, with the observed values being slightly smaller than prediction by a maximum of 50%.

2.5.6 The Anharmonicity Constants

The Fermi resonance constants are displayed in Table 2.6 along with other anharmonic parameters deduced from the overtone and hot band levels. Previous

TABLE 2.6
Anharmonic Constants in cm^{-1} for $^{34}\text{S}^{18}\text{O}_3$

constant Ref. (18)	This work	
x_{22}	-0.007(14) ^a	0.072 ^b
x_{33}	-4.996 5(53)	-4.970
x_{44}	-0.016 24(64)	-0.017
x_{24}	0.217 748(66)	0.248
x^{33}	2.647 2(53)	2.605
x^{44}	0.143 55(64)	0.144
k_{122}	9.422(71)	10.36
$k^J_{122} \times 10^5$	-1.87(29)	
k_{144}	-1.503 5(19)	-1.54
$k^J_{144} \times 10^5$	-2.32(13)	
$k^K_{144} \times 10^5$	2.23(13)	

^a The uncertainties are two standard deviations. They refer to the last digits and are shown in parentheses.

^b Deperturbed value (Private communication, Ref. 18)

papers (3, 5) have shown Martin's *ab initio* predictions (18) for these constants to be slightly higher than the observed values. This is also true for $^{34}\text{S}^{18}\text{O}_3$ where k_{122} is overestimated by 10% and k_{144} by 2%. The x_{ii} constants are also listed and they too agree well with Martin. As in the case for $^{34}\text{S}^{16}\text{O}_3$, the x_{22} constant was not determinable.

2.5.7 The Rotational Constants and Equilibrium Bond Length for $^{34}\text{S}^{18}\text{O}_3$

Knowledge of the vibration-rotation $\alpha_i^B = -(B_i - B_0) = -\Delta B$ and α_i^C corrections permits calculation of equilibrium parameters for $^{34}\text{S}^{18}\text{O}_3$. Table 2.7 lists the rotational parameters that were fit to the equation

$$B_e = B_v + \sum_i \alpha_i^B (v_i + 1/2 d_i) - \sum_{ij} \gamma_{ij}^B (v_i + 1/2 d_i)(v_j + 1/2 d_j), \quad [12]$$

with a similar equation for C (sans C_e due to the lack of microwave data for this isotope). The table also lists constants obtained if the less well-determined $\gamma_{ij}^{B,C}$ correction terms are set to zero. With the γ correction included, the B_e value for $^{34}\text{S}^{18}\text{O}_3$ is within the experimental uncertainty of the B_e values of both $^{32}\text{S}^{16}\text{O}_3$ and $^{34}\text{S}^{16}\text{O}_3$, when multiplied by the product of $^{16}\text{O}/^{18}\text{O}$ ratio. The SO equilibrium bond length is calculated to be 141.733 7(3) pm and is within the experimental uncertainties of the r_e values of $^{32}\text{S}^{16}\text{O}_3$ and $^{34}\text{S}^{16}\text{O}_3$ of 141.734 0(1) and 141.734 7(7) pm respectively (3, 5).

TABLE 2.7
Rotational Constants^a for ³⁴S¹⁸O₃

Constant ^b	C constants	C constants ^c
$\alpha_1 \times 10^3$	0.350 23(86) ^d	0.350 23(86)
$\alpha_2^* \times 10^3$	-0.111 01(76)	-0.109 20(14)
$\alpha_3 \times 10^3$	0.511 10(13)	0.512 995(26)
$\alpha_4^* \times 10^3$	0.126 69(48)	0.127 927(79)
$(\frac{1}{2}\alpha_2^* + \alpha_4^*) \times 10^3$	0.071(66)	-0.073 33(12)
$\gamma_{22} \times 10^5$	-0.091(38)	
$\gamma_{33} \times 10^5$	-0.063 0(38)	
$\gamma_{44} \times 10^5$	0.041 6(94)	
$\gamma_{24} \times 10^5$	0.002(40)	
$(\frac{1}{4}\gamma_{22} + \gamma_{44} + \frac{1}{2}\gamma_{24}) \times 10^5$	-0.063(25)	
	B constants	B constants ^d
B_0	0.309 785 63(36) ^e	
$\alpha_1 \times 10^3$	0.706 6(12)	0.706 6(12)
$\alpha_2^* \times 10^3$	-0.772(70)	-0.652(14)
$\alpha_3 \times 10^3$	0.959 96(23)	0.961 896(29)
$\alpha_4^* \times 10^3$	0.102(35)	0.048 0(72)
$(\frac{1}{2}\alpha_2^* + \alpha_4^*) \times 10^3$	-0.283 19(63)	-0.278 30(12)
$\gamma_{22} \times 10^5$	-4.7(26)	
$\gamma_{33} \times 10^5$	-0.064 6(71)	
$\gamma_{44} \times 10^5$	2.3(13)	
$\gamma_{24} \times 10^5$	-2.6(14)	
$(\frac{1}{4}\gamma_{22} + \gamma_{44} + \frac{1}{2}\gamma_{24}) \times 10^5$	-0.201(45)	
B_e	0.310 818 4(12)	0.310 822 52(69)
r_e (pm) ^e	141.733 71(27)	141.732 76(16)
r_0 (pm) ^e	141.969 764(84)	

^a In cm⁻¹ except for r values.

^b The constants followed by an asterisk, *, are the constant with the ν_2/ν_4 Coriolis perturbation removed, the so-called deperturbed constants.

^c Value calculated without inclusion of γ terms.

^d The uncertainties are two standard deviations. They refer to the last digits and are shown in parentheses.

^e The r values are calculated using NIST Physical Reference Data values of $h = 6.62606876(52) \times 10^{-34}$ J s, $N_A = 6.02214199(47) \times 10^{23}$ mol⁻¹, and $m(^{16}\text{O}) = 15.9949146221(15)$ amu.

2.6 Studies of $^{32}\text{S}^{18}\text{O}_3$

Early in the course of this work, samples of $^{32}\text{S}^{18}\text{O}_3$ were prepared and examined by CARS and FTIR methods. The ν_1 CARS spectrum is displayed in Fig. 2.4 and the ν_2 , ν_4 infrared region is shown in Fig. 2.7. Compared to the $^{34}\text{S}^{18}\text{O}_3$, the $^{32}\text{S}^{18}\text{O}_3$ was more contaminated by mixed oxygen forms such as $^{32}\text{S}^{16}\text{O}^{18}\text{O}_2$ and $^{32}\text{S}^{16}\text{O}_2^{18}\text{O}$ so that the ν_2 , ν_4 infrared spectra were more cluttered and difficult to analyze. The quality of the spectra was also somewhat poorer since fewer scans were averaged, 18 vs. 240 for $^{34}\text{S}^{18}\text{O}_3$.

An effort was made to improve this situation by introducing $^{32}\text{S}^{18}\text{O}_3$ into a special one meter multiple reflection cell at PNNL, but this was unsuccessful due to exchange with adsorbed H_2^{16}O in the cell. Moreover, the last of our $^{18}\text{O}_2$ sample was consumed in this experiment. Thus, we have used the original FTIR data in the analysis presented here. Fortunately, the analysis was greatly aided by knowledge of the parameters of the other isotopomers so that the quality of the fit achieved for $^{32}\text{S}^{18}\text{O}_3$ is still considered quite good.

2.6.1 Ground State Parameters of $^{32}\text{S}^{18}\text{O}_3$

The ground state parameters shown in Table 2.8 are very similar to those of $^{34}\text{S}^{18}\text{O}_3$, as would be expected considering the change of $^{32}\text{S}^{16}\text{O}_3$ to $^{34}\text{S}^{16}\text{O}_3$ is at the center of mass. In going from $^{34}\text{S}^{18}\text{O}_3$ to $^{32}\text{S}^{18}\text{O}_3$, B_0 drops by 0.000011 cm^{-1} , about the same amount observed in going from $^{34}\text{S}^{16}\text{O}_3$ to $^{32}\text{S}^{16}\text{O}_3$ (2, 4). In the latter

TABLE 2.8
Ground-State Rotational Constants
in cm⁻¹ for ³²S¹⁸O₃

C_0^a	0.154 663 29 ^b
B_0	0.309 774 64(36)
$D_J \times 10^7$	2.482 6(35)
$D_{JK} \times 10^7$	-4.433 2(59)
$D_K \times 10^7$	-2.083 ^c
$H_J \times 10^{12}$	1.081(66)
$H_{JK} \times 10^{12}$	-4.19(14)
$H_{KJ} \times 10^{12}$	-4.056(95)
$H_K \times 10^{12}$	-0.895 ^d
$\Delta_0 \times 10^{14}$	-0.700

^a The value of C_0 was calculated assuming the inertial defect is the same as that in ³²S¹⁶O₃ scaled by the B_0 ratio

^b The uncertainties are two standard deviations. They refer to the last digits and are shown in parentheses.

^c The value of D_k was calculated using the planarity condition.

^d The value of H_k was calculated by multiplying H_k of ³²S¹⁶O₃ by the ratio of the B values for ³⁴S¹⁸O₃/³²S¹⁶O₃

comparison, the higher order D and H constants are equivalent within their experimental uncertainties, but the D and H terms for $^{32}\text{S}^{18}\text{O}_3$ appear to be significantly larger than those for $^{34}\text{S}^{18}\text{O}_3$. It is not clear whether this is a real effect or, more likely, is a consequence of the somewhat poorer set of $^{32}\text{S}^{18}\text{O}_3$ data.

2.6.2 Parameters for ν_2 , ν_4 , $2\nu_2$, $\nu_2+\nu_4$ and $2\nu_4$

The parameters for the ν_2 and ν_4 levels, along with upper levels involved in their hot bands are shown in Table 2.9. Shown earlier in Fig. 2.7 were the experimental spectra for the different isotopomers of SO_3 . The most noticeable differences between the spectra are the band center locations and the intensity perturbations. Examination of the $B\zeta_{2,4}$ Coriolis parameter in Tables 2.4, 2.9, and in refs. 3 and 5, shows that the magnitude does not change appreciably from isotopomer to isotopomer (range from 0.207 cm^{-1} for $^{34}\text{S}^{16}\text{O}_3$ to 0.165 cm^{-1} for $^{32}\text{S}^{18}\text{O}_3$). Since this term appears as an off-diagonal interaction between ν_2 and ν_4 , its perturbation effect on the line positions and intensities will be governed by the ratio $B\zeta_{2,4}/(\nu_4-\nu_2)$. Changes in the energy denominator thus are important and it is seen that the perturbing effect will be largest for $^{32}\text{S}^{18}\text{O}_3$. This effect is shown dramatically in Fig. 2.19 where neglect of the Coriolis term shifts the predicted value of ${}^R\text{R}_{12}(25)$ by over 1.0 cm^{-1} . In contrast, similar perturbations shown in Fig. 2.8 for $^{34}\text{S}^{18}\text{O}_3$ are only about 0.90 cm^{-1} . The effect of these relatively large Coriolis interactions thus added appreciably to the challenge of analyzing the $^{32}\text{S}^{18}\text{O}_3$ spectra.

TABLE 2.9
The Rovibrational Constants in cm^{-1} for the ν_2, ν_4 States for the Fundamentals and Hot Bands of $^{32}\text{S}^{18}\text{O}_3$

constant	ν_2	$2\nu_2$	$\nu_2+\nu_4$	ν_4	$2\nu_4(l=0)$	$2\nu_4(l=2)$
ν_0	488.488 159(53) ^a	972.725(26)	990.987 14(10)	504.284 750(46)	1008.255 6(37)	1008.829 50(12)
$\Delta C^b \times 10^3$	0.110 72(19)	0.218 6(21)	-0.013 04(40)	-0.124 29(10)	-0.249 19(25)	{-0.249 19} ^c
$\Delta B \times 10^3$	0.732(16)	1.298(39)	0.604 0(77)	-0.082 5(80)	-0.083(18)	{-.083}
$\Delta D_J \times 10^{10}$	12.04(92)	14.9(72)	27.4(37)	8.28(79)	14.7(30)	{14.7}
$\Delta D_{JK} \times 10^{10}$	-16.6(26)	[-33.2] ^d	[-42.9]	-26.31(96)	[-52.61]	{-52.61}
$\Delta D_K \times 10^{10}$	6.3(23)	22.0(81)	18.8(42)	18.81(84)	38.7(28)	{38.7}
$\Delta H_J \times 10^{13}$	-1.03 ^e	[-2.1]	[-0.65]	0.38	[0.76]	[0.76]
$\Delta H_{JK} \times 10^{13}$	4.82(81)	[9.63]	[2.82]	-2.00(54)	[-4.00]	[-4.00]
$\Delta H_{KJ} \times 10^{13}$	-5.1(14)	[-10]	[-2.4]	2.67(99)	[5.33]	[5.33]
$\Delta H_K \times 10^{13}$	1.41(67)	[2.82]	[0.415]	-0.96(46)	[-1.99]	[-1.99]
$(C\zeta_4)$			-0.080 931(15)	-0.081 219 4(35)		-0.081 103 5(43)
$\eta_J \times 10^7$			-5.95(53)	-9.22(73)		-5.74(78)
$\eta_K \times 10^7$			5.61(53)	8.86(72)		5.39(78)
$q \times 10^4$			3.51(23)	4.37(16)	3.50(17)	
$(B\zeta_{2,4})$			0.164 14(26) ^f	0.164 98(22)	0.164 26(25) ^g	
$z_{2,4J} \times 10^7$			-3.60(26) ^f	-4.34(12)	-3.870(99) ^g	
$z_{2,4K} \times 10^7$			2.64(14) ^f	2.510(74)	3.04(21) ^g	
$Q_4 \times 10^6$						-3.0
# of transitions	1320	217	280	1614	78	211

^a The uncertainties are two standard deviations. They refer to the last digits and are shown in parentheses.

^b $\Delta C = C' - C_0$, $\Delta B = B' - B_0$, etc.

^c Constants enclosed in {brackets} were fixed to $2\nu_4(l=0)$ values

^d Constants enclosed in [brackets] were fixed to the appropriate combination of values from the ν_2/ν_4 fundamentals.

^e Constants enclosed in |brackets| were fixed to a value from $^{34}\text{S}^{18}\text{O}_3$ where it was determinable

^f Contained in the $W_{1,1}$ term for $\nu_2+\nu_4$ interacting with $2\nu_2$.

^g Contained in the $W_{1,1}$ term for $\nu_2+\nu_4$ interacting with $2\nu_4(l=0)$ and $2\nu_4(l=2)$.

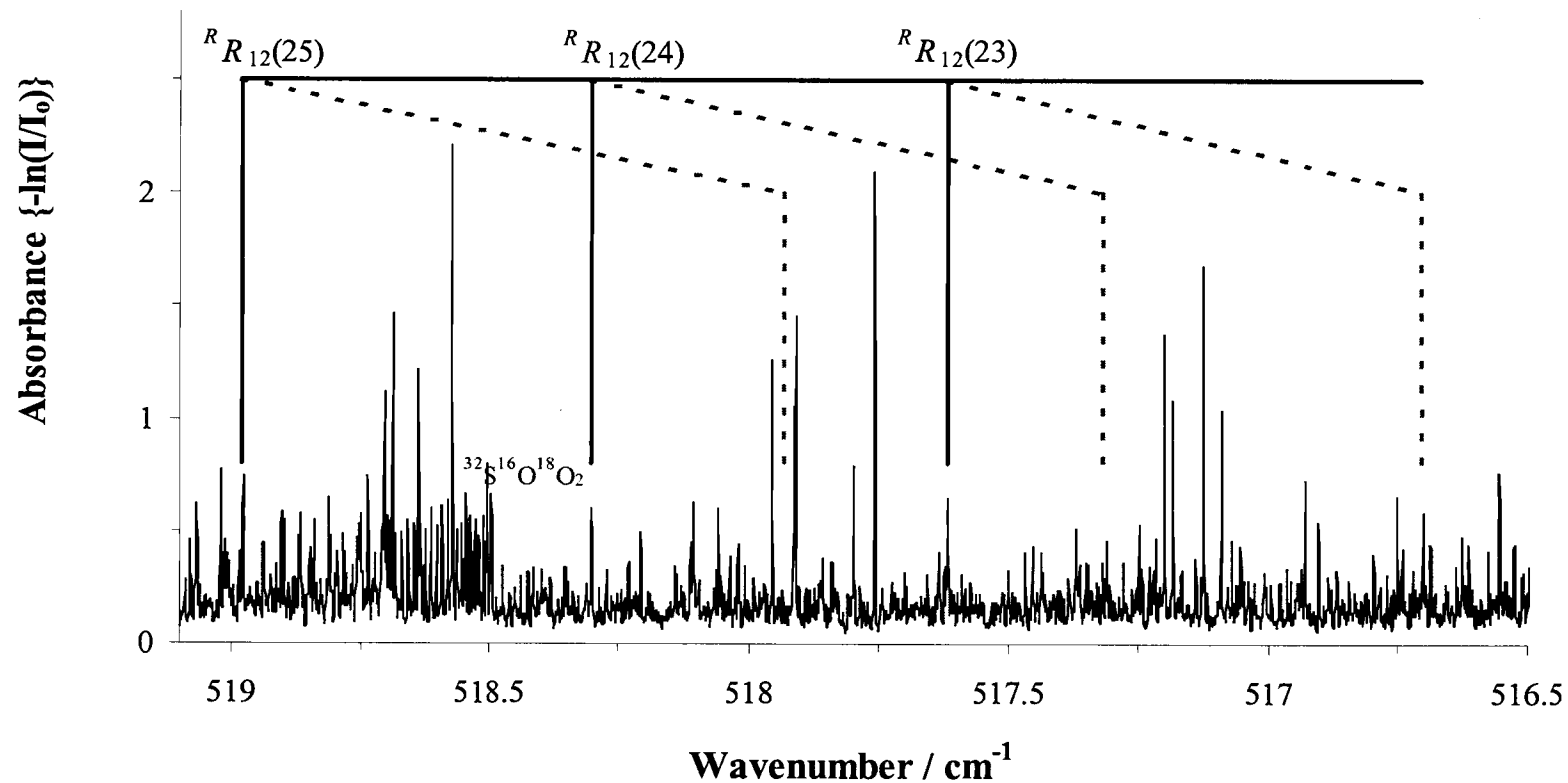


Fig. 2.19 High resolution IR spectrum of ${}^{32}\text{S}{}^{18}\text{O}_3$. The effect of the Coriolis perturbation is demonstrated with the shifting of the predicted line positions ${}^R R_{12}(23)$ through ${}^R R_{12}(25)$ sequence. The positions of the transitions have been calculated both with (—) and without (- - -) the Coriolis term.

The observed values of the band origins for ν_2 and ν_4 of 486.5 and 504.3 cm^{-1} are somewhat lower than the *ab initio* predictions of Martin (18), 487.5 and 502.4 cm^{-1} , respectively. The experimental ν_2 ratios for the a_2'' out-of-plane bend are 0.9777 and 1.0188 for $^{32}\text{S}^{18}\text{O}_3/^{32}\text{S}^{16}\text{O}_3$ and $^{32}\text{S}^{18}\text{O}_3/^{34}\text{S}^{18}\text{O}_3$, respectively. These ratios are in good accord with the calculated G-matrix ratios of 0.9775 and 1.0190. The magnitude of the deviation of these ratios from unity implies that replacing the center of mass of SO_3 with a heavier isotope has less of an effect on the ν_2 vibration than does replacement of the three oxygen atoms. We note that the experimental ν_4 band origin ratio for $^{34}\text{S}^{18}\text{O}_3/^{32}\text{S}^{18}\text{O}_3$ (0.9956) is nearly the same as that (0.9955) found for $^{34}\text{S}^{16}\text{O}_3/^{32}\text{S}^{16}\text{O}_3$.

The ΔB , ΔC changes in the rotational constants for $^{32}\text{S}^{18}\text{O}_3$ are very similar to those found in $^{34}\text{S}^{18}\text{O}_3$, as was expected from the comparison of $^{32}\text{S}^{16}\text{O}_3$ to $^{34}\text{S}^{16}\text{O}_3$. In the latter case, increasing the mass of the sulfur lowers the amplitude of the ν_2 vibration and thus increases the moment of inertia, so the ΔB value drops by almost 5%. In going from $^{32}\text{S}^{18}\text{O}_3$ to $^{34}\text{S}^{18}\text{O}_3$, the effect is enhanced and the ΔB value drops by 10%. The ΔC changes are smaller for ^{34}S substitution, dropping by 1.6% for the ^{16}O pair compared to 1.4% for the ^{18}O pair. A curious result is observed in the ΔB , ΔC changes when the ν_4 vibration is excited. Both ΔB and ΔC decrease in magnitude in going from $^{32}\text{S}^{16}\text{O}_3$ to $^{34}\text{S}^{16}\text{O}_3$. For the ^{18}O comparison, the ΔB value decreases, but the ΔC value increases. Moreover, ΔB for $^{32}\text{S}^{18}\text{O}_3$ is larger than for $^{32}\text{S}^{16}\text{O}_3$ by 10%, but ΔC is smaller by 26%. These small deviations from

expected systematic trends may suggest that some of the constants assumed in the $^{32}\text{S}^{18}\text{O}_3$ fitting are influencing the parameters.

2.6.3 The ν_2/ν_4 Hot Bands

As was mentioned earlier, the presence of mixed isotopic species hampered the assignments of the infrared hot bands of $^{32}\text{S}^{18}\text{O}_3$. Despite this nuisance, it was possible to confidently assign 786 infrared transitions. This was not sufficient to determine all of the ν_1 parameters so that a few of the actual CARS transitions were used in the fitting process (at reduced weight). Only when this was done was it possible to adequately reproduce the experimental CARS spectrum. It was also found necessary to fix the ΔD_{JK} terms for $2\nu_2, \nu_2+\nu_4$, and $2\nu_4$ vibrations to their ν_2/ν_4 fundamental combination values. In addition, a small $W_{-2,4}$ term was not determinable in this work and it was therefore fixed at the $^{34}\text{S}^{18}\text{O}_3$ value.

2.6.4 The ν_1 Constants and the Calculated CARS Spectrum

Of the 786 hot band transitions assigned in this work, only 3 had more than 50% ν_1 character, and only 91 contained more than 10%. As a consequence, the constraints in the ν_1 parameters were less effective than for $^{34}\text{S}^{18}\text{O}_3$ and it was necessary to assign 5 CARS transitions and include them in the final fitting. Only CARS features that could be assigned to a single isolated transition were used and these were given an uncertainty 20 \times larger than those of the infrared transitions. The ΔD terms for the ν_1 vibration were also set equal to the $^{34}\text{S}^{18}\text{O}_3$ values where they

were determinable. With these constraints, the calculated CARS spectrum in Fig. 2.20, which uses the ν_1 parameters in Table 2.10 comes very close to the observed spectrum. The band origin and the rotational constants ΔB and ΔC for ν_1 are almost, within experimental uncertainties, identical to those found in $^{34}\text{S}^{18}\text{O}_3$.

From the analysis of the spectra for the four isotopically substituted SO_3 species, it is evident that the precise positions of ν_1 and the hot band levels, particularly $2\nu_4$, govern the shape of the CARS spectra. In $^{32}\text{S}^{16}\text{O}_3$ and $^{34}\text{S}^{16}\text{O}_3$, the $2\nu_4$ level lies below ν_1 , and in $^{34}\text{S}^{18}\text{O}_3$ the two are nearly resonant. In $^{32}\text{S}^{18}\text{O}_3$, however, all of $2\nu_4$ lies well above ν_1 , causing the k_{144} Fermi resonant term to push on it from a different side than in the other isotopomers (Fig. 2.10). The consequence of this is seen in the energy level diagram of Fig. 2.21. Here, it is seen that the ν_1 levels interact especially with the $2\nu_4(l = +2)$ levels. The $2\nu_4(l = +2)$ states vibration do not directly couple to ν_1 of course, but rather couple to $2\nu_4(l = 0)$ via the $W_{2,2}$, interaction. Perturbations to $2\nu_4(l = 0)$ are then passed through the k_{144} Fermi resonance. This results in fairly smooth line progressions, as shown for the ν_1 $K=0$ sequence in panel e of the expanded level diagram of Fig. 2.22. However, crossing of the $2\nu_4$, ν_1 levels occur for $2\nu_4$ sequences with $K \geq 14$ ($k-l = 15$) and the perturbations are more dramatic. For example, for the ν_1 , $k-l = 15$ sequence shown in panel d of Fig. 2.22, a clear jump occurs between $J=18$ and 19 lines, due to the avoided crossing. Similar jumps are seen in the higher $k-l$ sequences, such as shown for $k-l = 27$ in panel c, and the result produces the Q -branch structure shown in panel

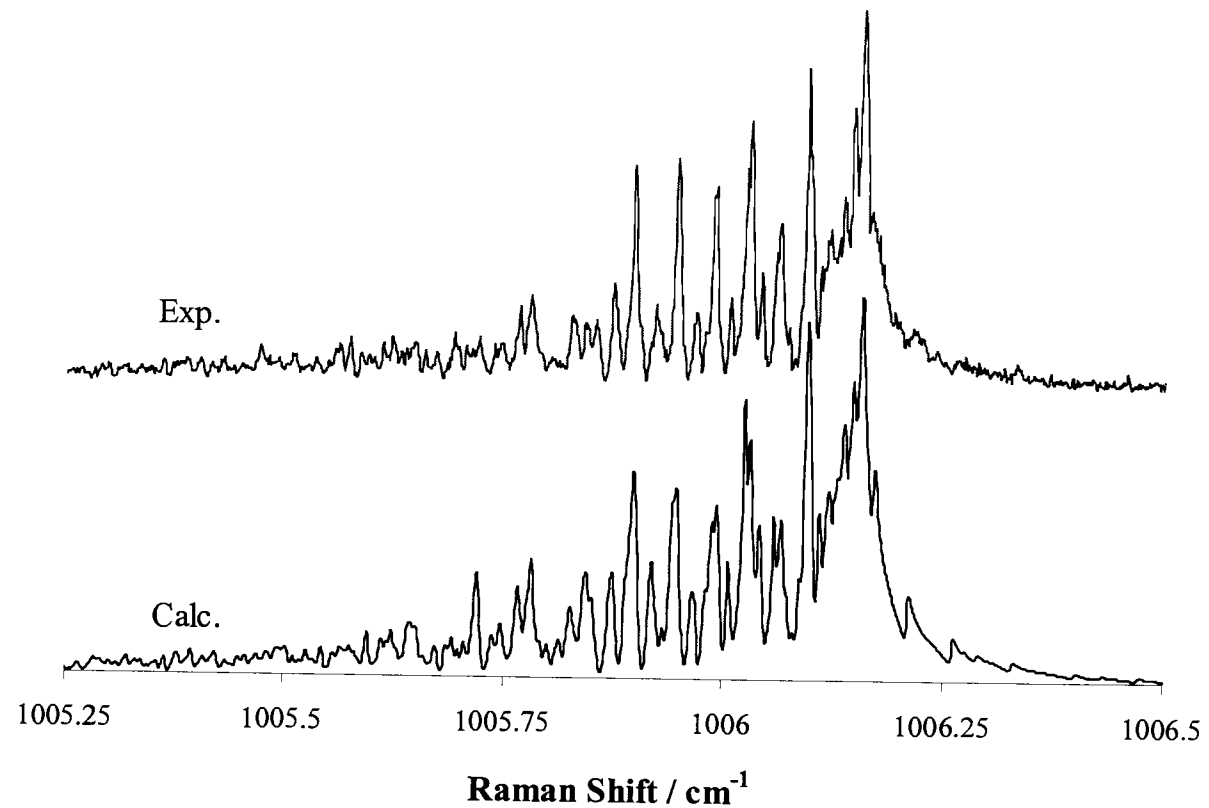


Fig. 2.20 The CARS spectrum of ν_1 of $^{32}\text{S}^{18}\text{O}_3$. The fit of the CARS spectrum using parameters derived from infrared hot band transitions and five CARS transitions is displayed below the experimental curve.

TABLE 2.10
The Rovibrational Constants in cm^{-1}
for ν_1 of $^{32}\text{S}^{18}\text{O}_3$

ν_0	1004.693(23) ^a	1005.0 ^b
$\Delta C^c \times 10^3$	-0.347 6(31)	
$\Delta B \times 10^3$	-0.712 2(23)	
$\Delta D_J \times 10^{10}$	24 ^d	
$\Delta D_{JK} \times 10^{10}$	-49	
$\Delta D_K \times 10^{10}$	24	

^a The uncertainties are two standard deviations. They refer to the last digits and are shown in parentheses.

^b Deperturbed *ab initio* value (Private communication, Ref. 18)

^c $\Delta C = C' - C_0$, $\Delta B = B' - B_0$, etc

^d Constants in |brackets| were fixed to the same values as for $^{34}\text{S}^{18}\text{O}_3$.

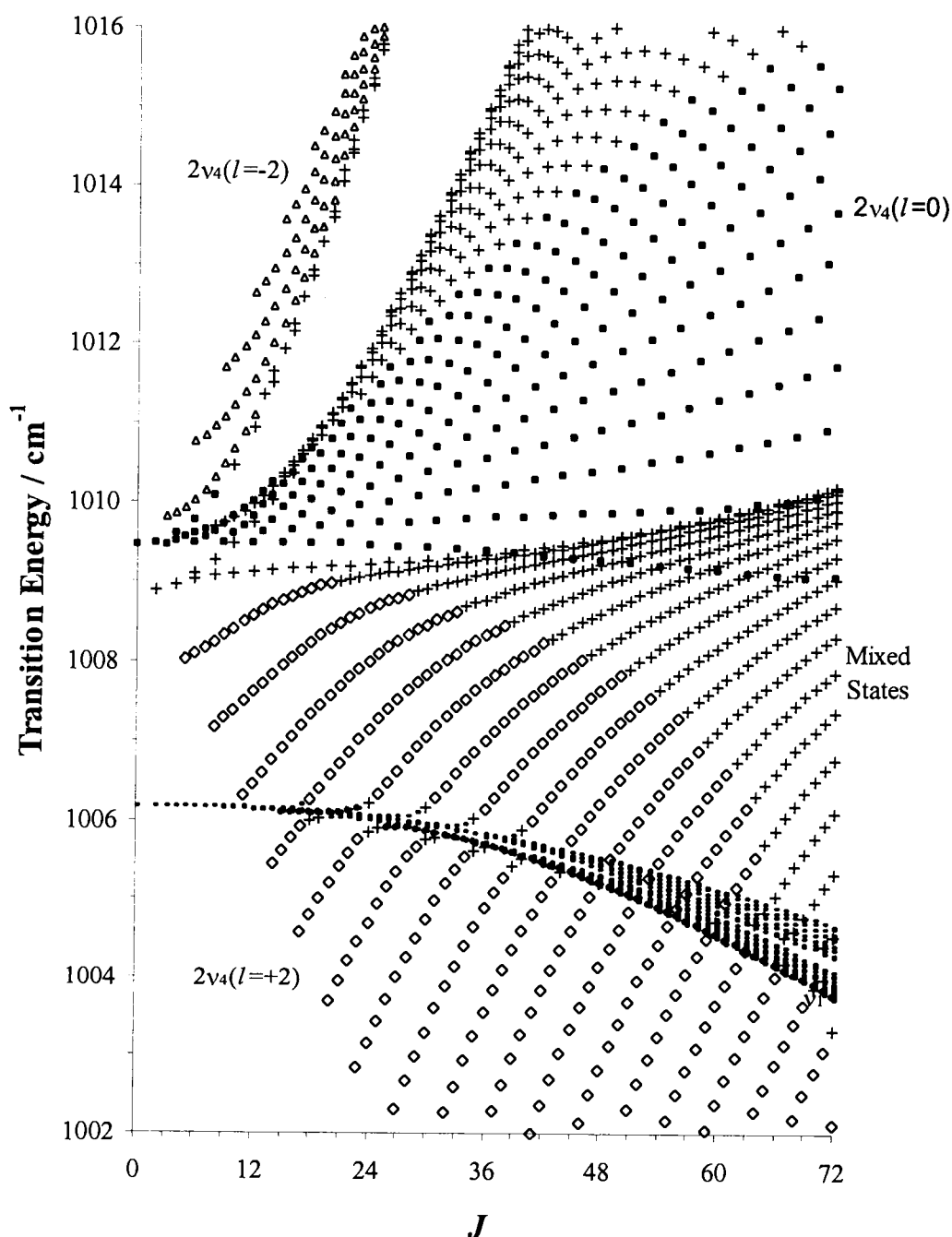


Fig. 2.21 Reduced energy diagram corresponding to Q -branch transitions from the ground state of $^{32}\text{S}^{18}\text{O}^3$ to v_1 and its perturbing states. States identified as $v_1(-)$, $2v_4(l=-2)$ (\blacktriangle), $2v_4(l=0)$ (\blacksquare) and $2v_4(l=+2)$ (\diamond) are at least 50% of the identified state. States that do not have any component greater than 50% are denoted as mixed states (+).

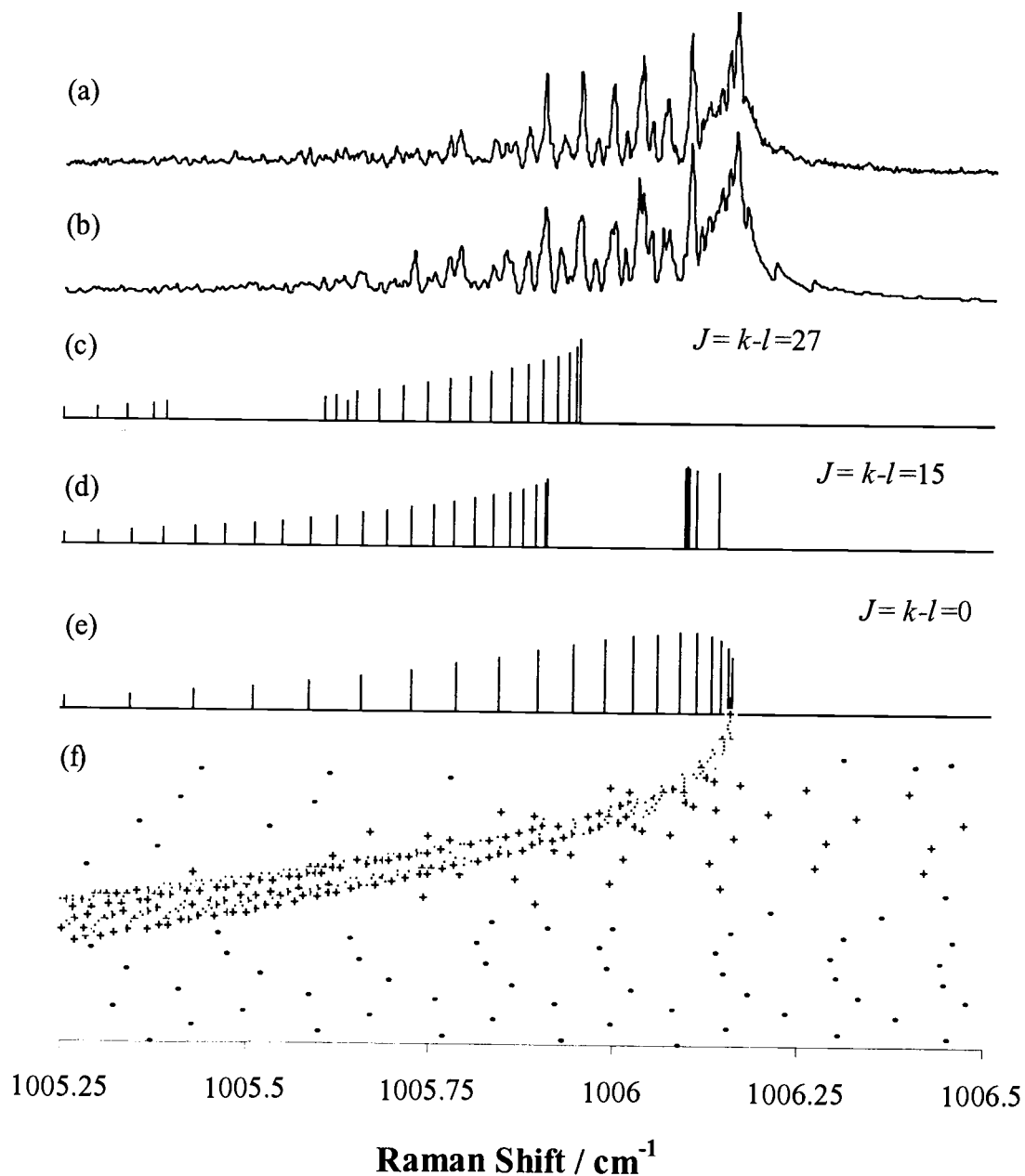


Fig. 2.22 Experimental and calculated CARS spectra for $^{32}\text{S}^{18}\text{O}_3$ (a-b), along with an expanded view of Fig. 2.21 showing the level pattern (f) to illustrate how this pattern contributes to the appearance of the spectrum. Those levels with 10% or greater of the maximum intensity are designated with a +. Stick spectra for $k-l = 0$, 15 and 27 show the level pattern of these $k-l$ subbands to illustrate the role of perturbations on the spectrum (c-e). The start of each sequence ($J = k-l$) is indicated with an arrow.

b. The close similarity to the experimental spectrum at the top of the sequence is considered quite good although not quite as exact as for the other isotopomers.

2.6.5 The Anharmonicity Constants

The Fermi resonance and anharmonicity constants for $^{32}\text{S}^{18}\text{O}_3$ are listed in Table 2.11. The uncertainties for most of the x_{ij} constants are larger than in the other isotopomers due to the reduced number of fitted transitions. Nonetheless, the agreement of the constants with Martin's predicted *ab initio* values is comparable to that seen for the other isotopomers. A possible exception is x_{44} for which the agreement is better for the other isotopomers. The k_{122} and k_{144} values are well determined and lead to predicted CARS spectra shown in Fig. 2.23 when set to zero. The unperturbed ν_1 parameter is 1004.69 cm^{-1} at the band origin of the CARS Q -branch when k_{122} and k_{144} are turned off (Fig 2.23, d). Since $2\nu_4$ lies above ν_1 for $^{32}\text{S}^{18}\text{O}_3$, turning on k_{144} (with $k_{122}=0$, panel c) causes the band to drop about 0.5 cm^{-1} . If only k_{122} is turned on (b), the push by the Fermi interaction increases the band position by about 2.5 cm^{-1} . Only when both interactions, along with all $W_{1,1}$ and $W_{2,2}$ Coriolis terms are included is the fit "just right".

2.6.6 The Equilibrium Bond Lengths

Table 2.12 gives the values of the rotational parameters for $^{32}\text{S}^{18}\text{O}_3$. The α and γ terms are very similar to those found in $^{32}\text{S}^{18}\text{O}_3$ in both magnitude and uncertainty. These values were used as input for equation 12 to obtain a B_e value of

TABLE 2.11
Anharmonic Constants in cm^{-1} for $^{32}\text{S}^{18}\text{O}_3$

constant	This work	Ref. (18)
x_{22}	-0.007(12) ^a	0.075 ^b
x_{33}	-5.148(10)	-5.135
x_{44}	-0.013 47(91)	-0.039
x_{24}	0.214 23(10)	0.246
x^{33}	2.740(10)	2.720
x^{44}	0.143 47(92)	0.168
k_{122}	9.586(43)	10.56
$k_{122}^J \times 10^5$	-1.69(43)	
k_{144}	-1.644 7(17)	-1.65
$k_{144}^J \times 10^5$	-2.57(11)	
$k_{144}^K \times 10^5$	2.46(17)	

^a The uncertainties are two standard deviations. They refer to the last digits and are shown in parentheses.

^b Deperturbed value (Private communication, Ref. 18)

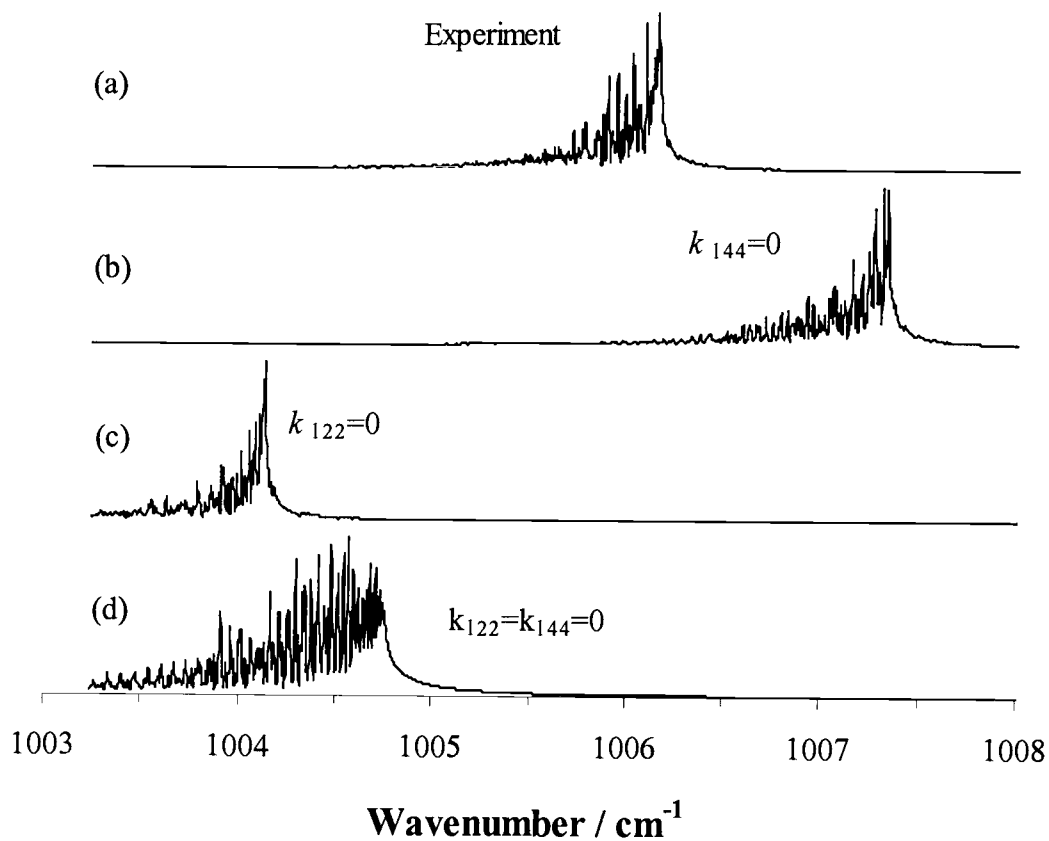


Fig. 2.23 Effect of ν_1 CARS spectrum (a, experimental spectrum) of setting the Fermi resonance constants k_{122} and k_{144} to zero (b-d calculated spectra).

TABLE 2.12
Rotational Constants^a for ³²S¹⁸O₃

Constant ^b	C constants	C constants ^c
$\alpha_1 \times 10^3$	0.347 6(31) ^d	0.347 6(31)
$\alpha_2^* \times 10^3$	-0.113 0(22)	-0.110 72(19)
$\alpha_3 \times 10^3$	0.522 80(22)	0.525 699(46)
$\alpha_4^* \times 10^3$	0.123 66(59)	0.124 29(10)
$(\frac{1}{2}\alpha_2^* + \alpha_4^*) \times 10^3$	0.067 16(12)	-0.068 94(16)
$\gamma_{22} \times 10^5$	-0.14(11)	
$\gamma_{33} \times 10^5$	-0.096 6(59)	
$\gamma_{44} \times 10^5$	0.030(13)	
$\gamma_{24} \times 10^5$	0.054(43)	
$(\frac{1}{4}\gamma_{22} + \gamma_{44} + \frac{1}{2}\gamma_{24}) \times 10^5$	-0.038(36)	
	B constants	B constants ^d
B_0	0.309 774 64(56) ^e	
$\alpha_1 \times 10^3$	0.712 2(23)	0.712 2(23)
$\alpha_2^* \times 10^3$	-0.942(70)	-0.732(16)
$\alpha_3 \times 10^3$	0.976 54(30)	0.977 925(49)
$\alpha_4^* \times 10^3$	0.183(35)	0.082 5(80)
$(\frac{1}{2}\alpha_2^* + \alpha_4^*) \times 10^3$	-0.288 6(11)	-0.283 31(15)
$\gamma_{22} \times 10^5$	-8.6(24)	
$\gamma_{33} \times 10^5$	-0.046 2(91)	
$\gamma_{44} \times 10^5$	4.1(12)	
$\gamma_{24} \times 10^5$	-4.5(11)	
$(\frac{1}{4}\gamma_{22} + \gamma_{44} + \frac{1}{2}\gamma_{24}) \times 10^5$	-0.238(77)	
B_e	0.310 821 5(20)	0.310 825 3(13)
r_e (pm) ^e	141.732 99(46)	141.732 12(30)
r_0 (pm) ^e	141.972 28(13)	

^a In cm⁻¹ except for r values.

^b The constants followed by an asterisk, *, are the constant with the v_2/v_4 Coriolis perturbation removed, the so-called deperturbed constants.

^c Value calculated without inclusion of γ terms.

^d The uncertainties are two standard deviations. They refer to the last digits and are shown in parentheses.

^e The r values are calculated using NIST Physical Reference Data values of $h = 6.62606876(52) \times 10^{-34}$ J s, $N_A = 6.02214199(47) \times 10^{23}$ mol⁻¹, and $m(^{16}\text{O}) = 15.9949146221(15)$ amu.

0.310 821 5(20) cm^{-1} . Within the experimental uncertainties, this is identical with the $^{34}\text{S}^{18}\text{O}_3$ B_e value of 0.310 818 4(12) cm^{-1} . The r_e value calculated for $^{32}\text{S}^{18}\text{O}_3$ was 141.732 99(46) pm. This value is (just) within the experimental uncertainty of the $^{34}\text{S}^{18}\text{O}_3$ value of 141.733 71(27) pm. These can be compared with r_e values of 141.734 03(13) pm for $^{32}\text{S}^{16}\text{O}_3$, and 141.734 70(68) pm for $^{34}\text{S}^{16}\text{O}_3$. Although marginally beyond the uncertainties, the average r_e value for the ^{18}O species appears to be 0.0010 pm smaller than the average for the ^{16}O species. It is interesting to consider the possible cause of such a small difference. It may indicate that the potential function for SO_3 is not completely isotope independent, i.e. that a breakdown of the Born-Oppenheimer approximation may occur as a molecule vibrates and rotates due to the lag of the electrons (such effects have been seen for diatomic molecules (21, 22)). However, it could also be that the calculated moment of inertia ($I_B = m_o r_e^2$) for SO_3 is simply an underestimate since not all of the mass of electrons around each oxygen atom is localized at the nuclear position. An r_e calculated from the experimental I_B value is thus too high. This error goes to zero for infinite nuclear mass so the effect would be smaller in the ^{18}O substituted species. This would predict a smaller average r_e value for the ^{18}O species than for the ^{16}O species, as observed.

2.7.7 The Force Constants

Accurately unperturbed vibrational frequencies have now been determined for all of the symmetric SO_3 isotopomers. Using this data, a global force field

analysis was performed. Wilson's FG matrix method (19) was implemented using the harmonic force field program ASYM(40) written by Ian Mills and Lisa Hedberg (20). Frequencies were calculated for these symmetric as well as for the mixed isotopomers. The results are given in Table 2.13. Some rough estimates of the band origins of the mixed isotopomers were deduced from apparent Q -branches such as seen in Figs. 2.8 and 2.19. These estimated frequencies are also listed in the table, but they were not used in obtaining the force constants.

Table 2.14 lists the force constants derived from this calculation. From the symmetrized force constants (F), one can deduce the internal f_r S-O stretch and f_{rr} stretch-stretch interaction constants. It is seen that the f_r stretching constant is higher in magnitude in SO_3 than for the either SO_2 or SO . This trend is consistent with bond length changes, with the S-O distance shorter in SO_3 than in SO_2 and SO by 1.0 % and 4.5% respectively. These trends are conspicuously opposite the normal trend seen as bond order increases (SO_3 has a bond order of $4/3$, SO_2 of $3/2$ and SO of 2 in the usual valence picture). This anomaly has been attributed to resonance hybrids involving $p\pi-p\pi$ S-O bonding and participation of oxygen $p\pi$ orbitals with empty sulfur $d\pi$ orbitals (23). An additional confirmation is provided in Martin's (18) *ab initio* calculations where the trend in experimental properties were calculated only when $d\pi$ orbitals were included in the basis set.

Table 2.13
Predicted Frequencies of the Isotopomers of SO₃

Isotopic Species	Calculated	Observed	Calc.-Obs.	Isotopic Species	Calculated	Observed	Calc.-Obs.
³² S ¹⁶ O ₃				³⁴ S ¹⁶ O ₃			
v ₁	1065.31	1064.92	0.39	v ₁	1065.31	1064.92	0.39
v ₂	497.67	497.57	0.10	v ₂	488.82	488.80	0.02
v ₃	1391.95	1391.52	0.43	v ₃	1373.37	1373.44	-0.07
v ₄	530.20	530.09	0.12	v ₄	527.82	527.68	0.14
³² S ¹⁶ O ₂ ¹⁸ O				³⁴ S ¹⁶ O ₂ ¹⁸ O			
v ₁	1043.4	1044.6	-1.2	v ₁	1043.233	-	-
v ₂	494.0	493.9	0.1	v ₂	485.043	-	-
v ₃	1365.0	1364.8	0.2	v ₃	1346.129	-	-
v ₃	1391.9	1392.1	-0.2	v ₃	1373.308	-	-
v ₄	516.3	516.0	0.3	v ₄	513.799	-	-
v ₄	526.9	526.9	0.0	v ₄	524.677	-	-
³² S ¹⁶ O ¹⁸ O ₂				³⁴ S ¹⁶ O ¹⁸ O ₂			
v ₁	1023.2	1025.1	-1.9	v ₁	1023.063	-	-
v ₂	490.2	490.2	0.1	v ₂	481.239	-	-
v ₃	1349.0	1349.0	0.0	v ₃	1329.713	-	-
v ₃	1379.1	1379.5	-0.4	v ₃	1360.38	-	-
v ₄	507.4	506.7	0.7	v ₄	504.993	-	-
v ₄	518.4	518.5	-0.1	v ₄	516.2	516.3	-0.1
³² S ¹⁸ O ₃				³⁴ S ¹⁸ O ₃			
v ₁	1004.25	1004.69	-0.44	v ₁	1004.25	1004.66	-0.41
v ₂	486.47	486.49	-0.02	v ₂	477.40	477.51	-0.10
v ₃	1348.93	1348.85	0.07	v ₃	1329.63	1330.08	-0.45
v ₄	504.14	504.29	-0.14	v ₄	501.93	502.06	-0.12

^a Values obtained for the pure isotopic forms of SO₃ originated from Tables 3,4,8 and 9

^b Observed values were taken from medium resolution (0.125 cm⁻¹) spectra shown in Figs. 4, 5, and 6 of ref. 1 and from high resolution spectra such as in Figs. 2.8 and 2.19

Table 2.14
Calculated Force Constants and Bond
Lengths for Different Oxides of Sulfur

SO ₃	F ₁₁	10.695
	F ₂₂	0.833
	F ₃₃	10.387
	F ₃₄	-0.303
	F ₄₄	1.255
	f _r	10.489
	f _{rr}	0.103
	r _e	1.4173 Å
SO ₂ ^a	f _r	9.970
	r _e	1.4308 Å
SO ^a	f _r	8.134
	r _e	1.4811 Å

^aRef. 1

3 Coherent Raman Spectra of the ν_1 Mode of Carbon Suboxide

3.1 Introduction

Carbon suboxide, C_3O_2 is an unusual molecule that has fascinated and puzzled spectroscopists for decades. First prepared by Diels and Wolf in 1906 (24), it is a colorless lachromator with a boiling point of $7^\circ C$. Though the least common of the simple carbon oxides, C_3O_2 is ubiquitous. C_3O_2 is believed to play a role in photochemical reactions in the atmospheres of Earth (25, 26) and Venus (7, 27) and to exist on the surface of the moons of Jupiter (28, 29) and in Halley's comet (30). At high pressures, it readily undergoes polymerization to form a red solid film; Oyama (31) has suggested that the latter may contribute to the red color of the Martian surface, where carbon suboxide is proposed as a photolytic reaction product of CO_2 .

From structural and spectroscopic standpoints, carbon suboxide is intriguing because of its floppy structure, as indicated by the ν_7 CCC bending frequency of 18.25 cm^{-1} (32). To our knowledge this is the lowest value observed for any "linear" molecule. In fact, calculations and experiments indicate that the equilibrium structure of C_3O_2 is bent and even slightly W-shaped, with recent *ab initio* calculations by Koput (33) yielding CCC and CCO angles of 155.9° and

176.9° respectively. However all calculations and experimental results indicate that the barrier to linearity is small (20-40 cm^{-1}) so that the vibrationally averaged ground state structure is linear. C_3O_2 is thus termed a “quasi-linear molecule”, similar to the C_3 molecule, for which the bending mode is also quite low (63 cm^{-1}).

(34)

The vibrational modes of carbon suboxide are shown in Fig. 3.1. Due to the effective center of symmetry, the rule of mutual exclusion applies, with ν_1 , ν_2 , and ν_5 modes observable only by Raman methods (35-37) while the other modes appear only in the infrared, where they have been studied extensively (32, 37-40). In all cases, the spectra show added hot band structure arising from thermally populated levels of the ν_7 bending mode. Detailed analyses of the resultant spectra have revealed the ν_7 level structure in the vibrational manifolds of the other fundamentals, as illustrated in Fig. 3.2, which is taken from Fusina and Mills (41). Here the potentials are deduced from the observed level spacings and are represented by a simple two dimensional bending potential with quadratic and quartic terms. The results show that the potential barrier and the pattern of levels are quite sensitive to excitation of a normal mode. For example, on excitation of the ν_2 symmetric CC stretch, the barrier drops to about zero from 22 cm^{-1} in the ground state. However antisymmetric excitation of the ν_4 CC stretch more than doubles the barrier, to 49.3 cm^{-1} , and this increase is even greater (65.3 cm^{-1}) when the ν_3 antisymmetric CO stretch is excited. Less dramatic are the effects of

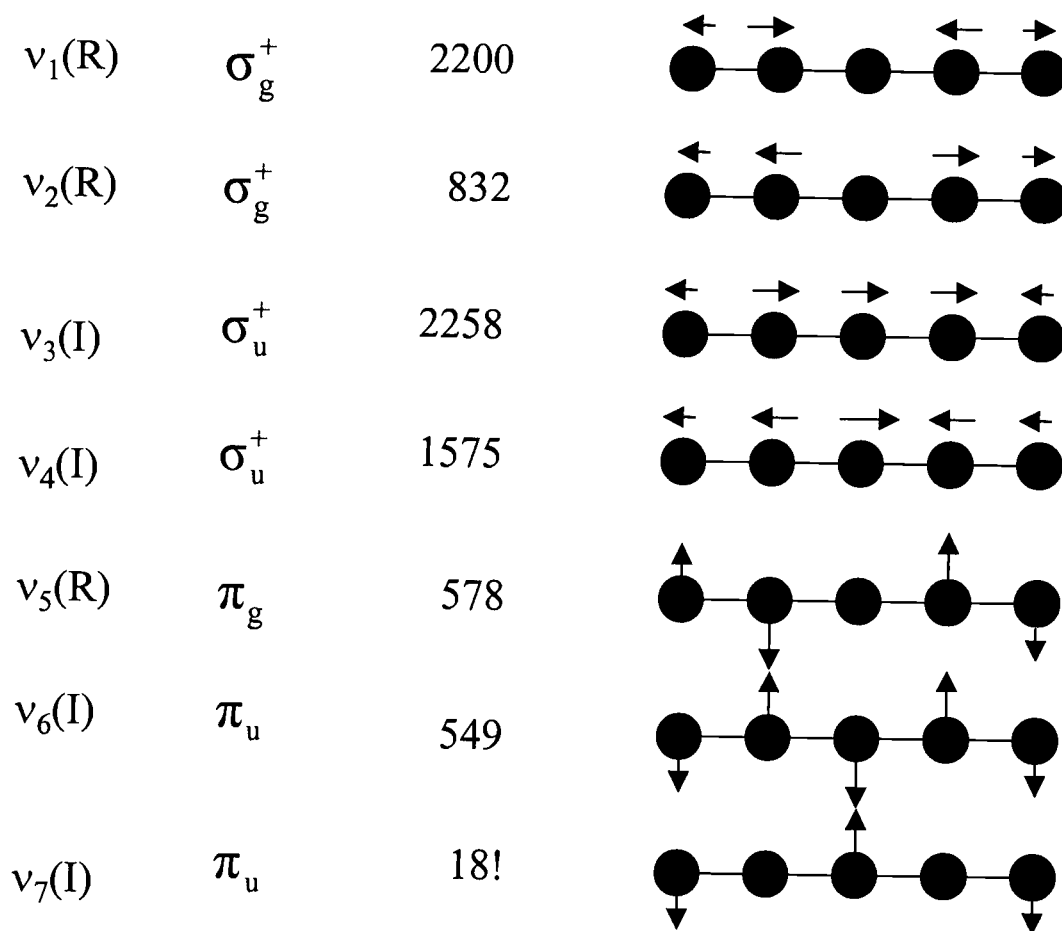


Fig. 3.1 The vibrational modes of C_3O_2

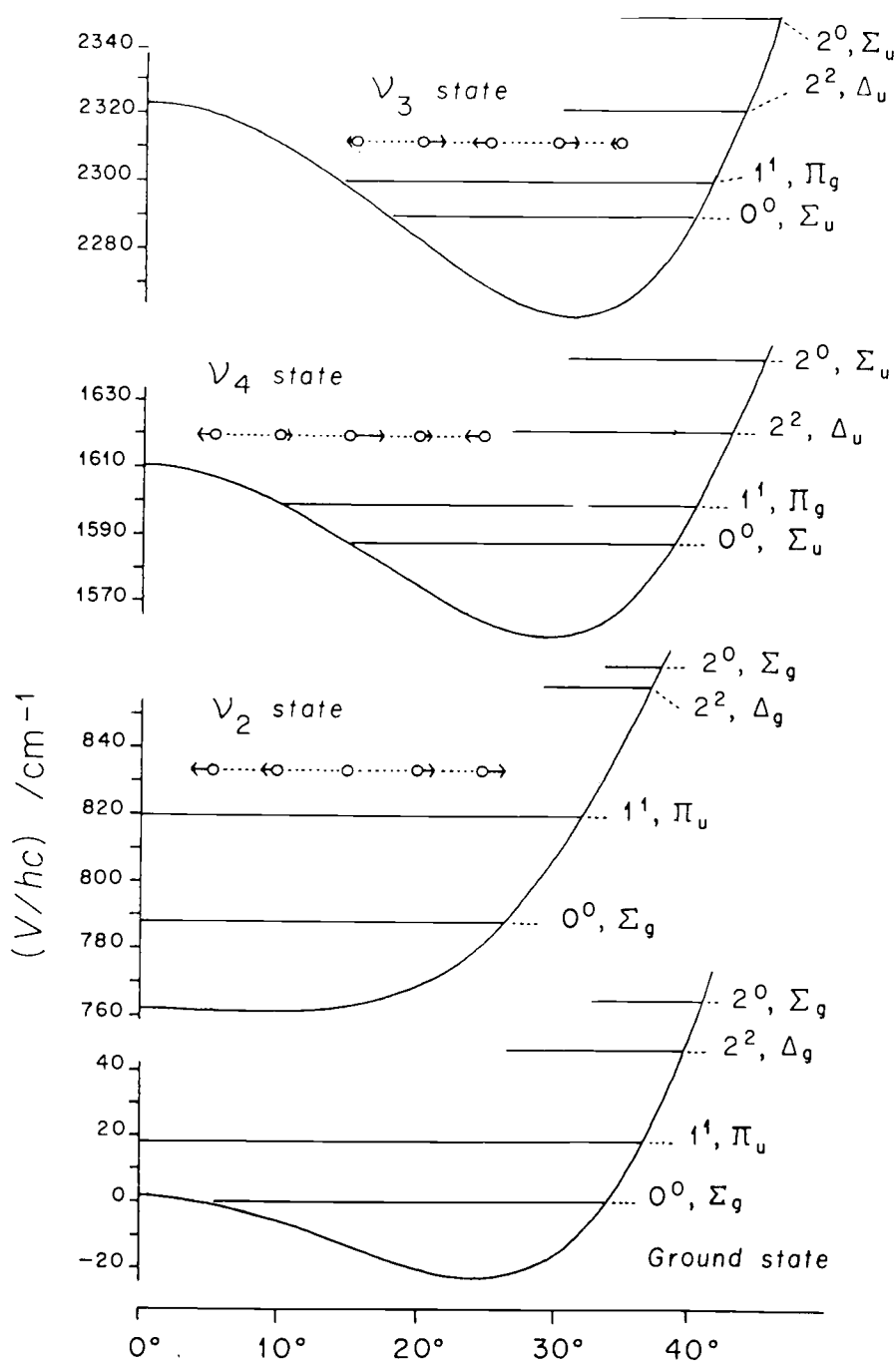


Fig. 3.2 The effective potential surfaces for the ground, v_2 , v_3 , and v_4 states. Reprinted from *J. Mol. Spec.* 79(1), L. Fusina, and I.M. Mills, "The Vibrational Dependence of the v_7 Bending Potential Function", 123-131, ©1980, with permission from Elsevier.

excitation in the ν_5 symmetric and ν_6 antisymmetric CCO bends, the barriers being 29.9 and 19.7 cm^{-1} respectively (42, 43).

Although Raman spectra have been reported (35) for the ν_1 symmetric CO stretch, the effect of excitation of this mode on the ν_7 barrier has not been examined in detail and is perhaps not obvious. By analogy with excitation of the CCC symmetric stretch one might expect a decrease in the barrier, but it is also true that excitation of the antisymmetric CO stretch results in a large barrier increase. The most recent (1979) Raman data on ν_1 (35) is of low resolution (0.25 cm^{-1}) but does reveal some hot band structure that suggests that the barrier is quite similar to that in the ground state. Since CARS spectra can now be obtained with much greater sensitivity and resolution, it was felt that a reexamination of the ν_1 Q -branch structure might be worthwhile and the results of this investigation are reported here.

3.2 Experimental

In these studies C_3O_2 was prepared through dehydration of malonic acid by phosphorous pentoxide, P_2O_5 . The malonic acid, powdered P_2O_5 and sand (to increase the reaction surface area) were mixed together in a 1:10:2 ratio and then heated to 140 °C in an oil bath while the vapors were collected in a liquid nitrogen cold trap. To reduce contamination from water, the sand was pre-roasted while being evacuated and the chemicals were mixed together in a dry bag. The

main products of the reaction were C_3O_2 , acetic acid and CO_2 . The latter was removed by pumping on the trap at $-110\text{ }^\circ\text{C}$, a temperature where the vapor pressure of CO_2 and C_3O_2 are 33.3 torr and 0.2 torr, respectively (12, 45). The C_3O_2 was separated from the acetic acid by warming the trap to $-50\text{ }^\circ\text{C}$ (vapor pressures of C_3O_2 and acetic acid are 45.8 and 0.1 torr, respectively) and distilling the C_3O_2 .

Due to its reactivity and tendency to polymerize, the sample was kept frozen at 77K until just before use. All handling of C_3O_2 was done in glass vacuum manifolds and cells with Teflon stopcocks and connectors. Spectra were recorded of samples at 4 kPa (30 torr) in glass cells and also in jet expansions in which Ar gas at about 0.5 atm was flowed through a C_3O_2 reservoir held at temperatures chosen to give a 50% mix. Due to the very limited amount of C_3O_2 available, the spectral scans in jets were taken rapidly and it was not possible to be certain that the concentration was constant during all scans. However, the wavenumber positions of features seen in the jet spectra were quite reproducible and, in the figures shown here, the intensities are believed to be a valid representation of the relative contributions of the Q -branch features. The spectra were taken at a position early in the expansion (about one to two nozzle diameters) since the signal to noise was better there and, also, the warmer jet close to the nozzle made it possible to measure a number of the rotational lines in the vibrational Q -branches.

A description of the CARS apparatus is given in section 2.2. In order to minimize decomposition of the sample during the static scans, the power of the probe beams was kept to less than 2 mJ/pulse. Surprisingly, when the intensity of the beams was too great, breakdown occurred at the ends of the sample cell rather than at the center where the focusing of the beams makes their intensities the greatest. This leads us to believe that the breakdown occurred because of heating on the window surface.

Modifications had to be made to the system in order to obtain the jet spectra. The sample cell was replaced with a vacuum chamber that was evacuated such that it maintained a pressure of less than 0.1 torr throughout the measurements. The sample was introduced into the chamber through a pulsed jet nozzle that was temporally adjusted to match the timing of the pump and probe beams. Nitrogen (atmosphere) was used to optimize the focal and spatial overlap such that the maximum CARS signal was achieved. Due to the low amount of C_3O_2 expelled from the nozzle, the power of the pump and Stokes beams were increased to around 13 and 3 mJ/pulse respectively. Vereschagin *et al.* studied saturation effects on this system (44) and found that, at this power, ac-Stark broadening will limit the resolution to around 0.004 cm^{-1} . Although almost twice the expected Doppler width, this value is sufficiently fine to resolve the individual Q -lines as will be seen in the following figures.

3.3 Results and Discussion

3.3.1 CARS Spectra of C_3O_2

Fig. 3.3 offers a comparison of the previous Raman spectrum and the CARS spectra obtained in this work. The top trace shows the Raman spectrum recorded at 0.25 cm^{-1} resolution by Lolck and Brodersen (35) and the dominant Q -branch is seen to consist of several unresolved features that they assigned to ν_7 hot bands according to the labeling shown at the top. An expanded view of this structure is seen in the higher resolution CARS spectrum shown in the middle and it is apparent that some of the Q_J line structure is discernable. However, due to the high line density and collisional broadening at the 30 torr sample pressure, a detailed analysis was not possible. It was for this reason that CARS spectra were taken for C_3O_2 samples cooled by expansion in a jet, where collisional broadening would be reduced and vibrational and rotational cooling might simplify the spectra.

The result of jet cooling on the CARS spectrum, shown at the bottom of Fig. 3.3, was quite surprising to us since it showed a dramatic enhancement of the two higher wavenumber Q -branches and a great reduction in intensity of the other branches seen in the room temperature scan. Clearly the previous assignment of the Raman transition from the ground state to one of the latter is incorrect and in fact the data suggest a reversal of the order of assignment, as shown in the middle of the figure.

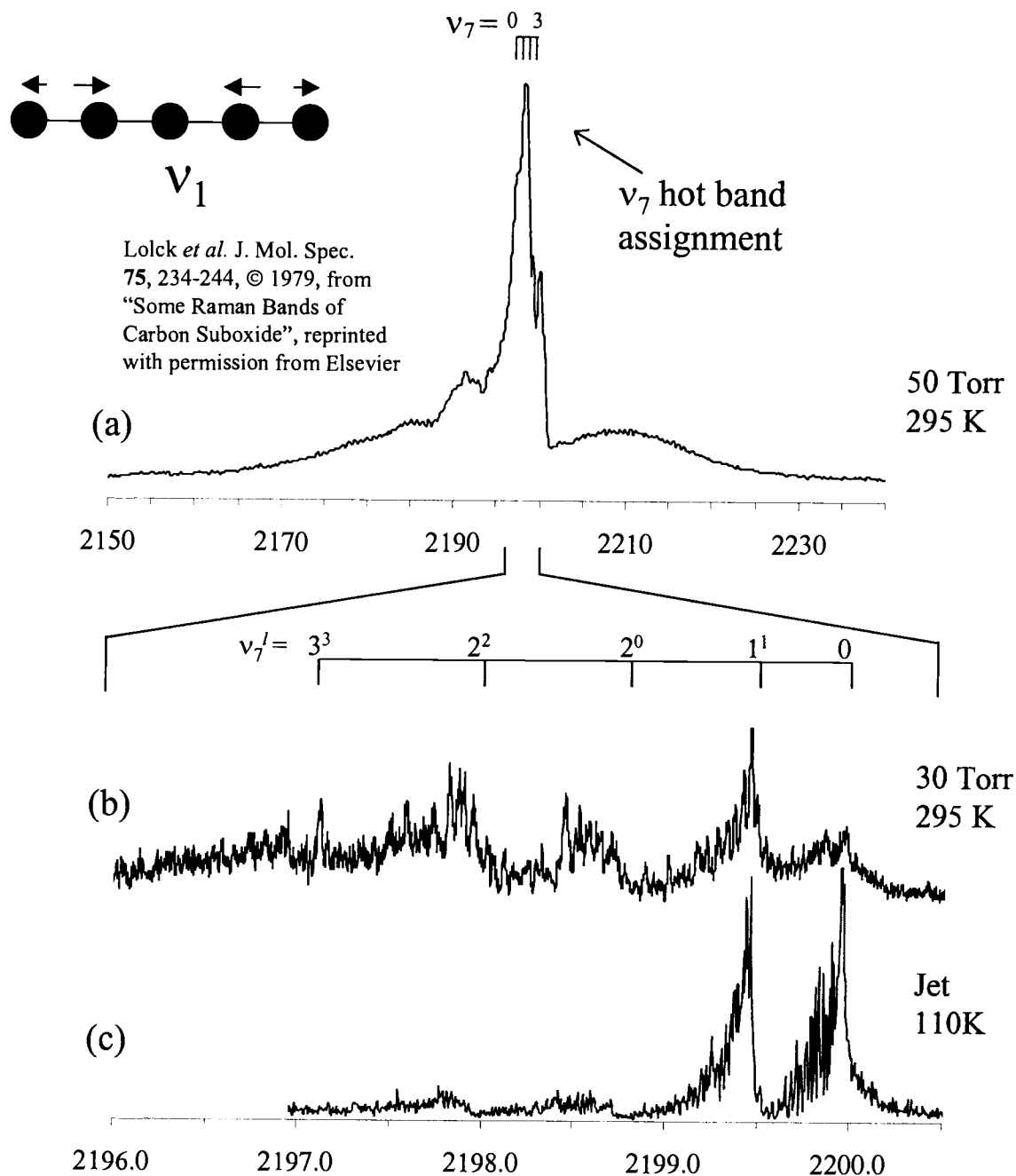


Fig. 3.3 Raman and CARS spectra of C_3O_2 . The Raman spectrum (a, 0.25 cm^{-1} instrumental resolution) shows a dominant, but unresolved Q -branch. The CARS spectrum (0.001 cm^{-1} instrumental resolution) taken at 295 K (b) reveals Q -branch features complicated by high line density and collisional broadening. The jet-cooled sample (c) clearly shows the $v_7^l = 0-3$ vibrational transitions. Note that the order of assignment in panel b is different than that given in panel a.

It is of course possible that either of the two main Q -branches seen in the jet spectra could be due to the $\Sigma - \Sigma$ transition from the ground state but a closer look at the rotational structure of these is revealing. Fig. 3.4 shows that the rotational lines in the highest wavenumber branch are more clearly defined than is the case in the other Q -branch. This is expected for transitions from the ground Σ state since J_{odd} levels, and hence J_{odd} lines, will be missing due to nuclear spin constraints. (Both ^{12}C and ^{16}O atoms are Bosons with nuclear spin zero so the nuclear spin functions are only symmetric to exchange of identical particles.) However, for degenerate Π and Δ states all lines are present and the features are less resolved.

3.3.2 Modeling of Spectra

From the spectra, there can be no doubt that the highest wavenumber Q -branch corresponds to transitions from $v_7 = 0$. The assignment of specific J values in this band is less certain but the values shown on Fig. 3.4 gave the most reasonable values of the vibration-rotation parameters and also seemed to give better standard errors than did fits in which all J values were changed by +2 or by -2, the maximum changes considered possible. From the experimental data the best fit was obtained for a simple Q -branch expression

$$Q_J = \nu_0 + (B' - B'')J(J+1) = 2199.97(6) - 0.000203(6) J(J+1)$$

so the $B' - B''$ value is quite reasonable. An initial estimate for $B' - B''$ of 0.00026 cm^{-1} was obtained from an estimate of the likely extension of the CO bond length

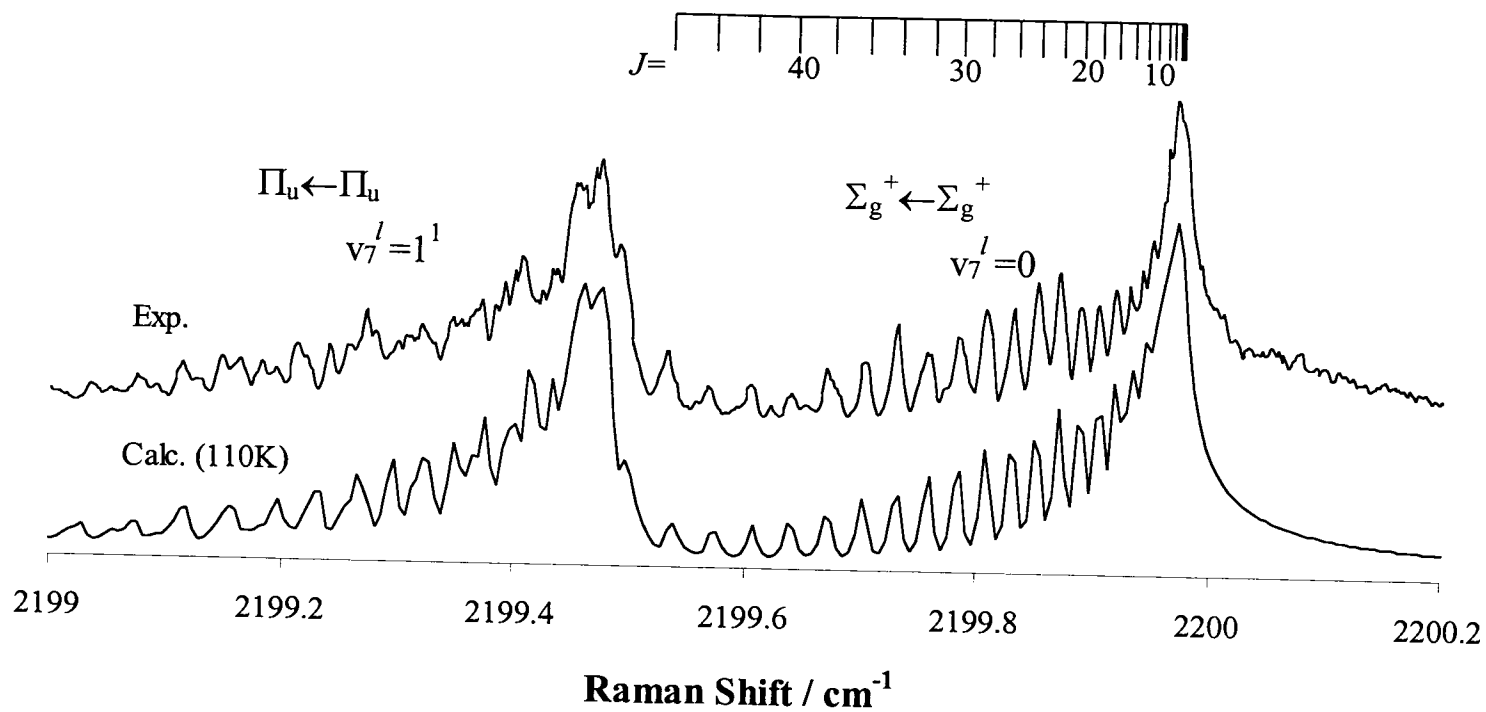


Fig. 3.4 The rotational modeling of the Q -branch of C_3O_2 . The fit of the CARS spectrum using parameters given in the text is displayed below the experimental curve.

from an analogy with the changes seen in CO. Another estimate was 0.00023 cm^{-1} from an anharmonic force field calculation by Fusina and Mills (41).

Because of interference effects in CARS spectra by overlapping lines, it is well known that the peak maxima can be shifted slightly from the true transition frequencies (46). To take this into account, an iterative fitting process was employed, with preliminary peak maxima from the CARS spectra first being used to generate by least squares a set of fitting parameters. These, along with an assumed rotational temperature in the jet, were used to calculate a CARS spectrum that was then compared with experiment. The differences between the calculated peak maxima and the input transition frequencies were then used to correct the experimental peak maxima to "true" transition values. These were then used in the least squares fit and the process was repeated until convergence was achieved. Table 3.1 shows the initial and final transitions, and the corrections for each line are seen to be small but significant at the fitted level. At the bottom are the final parameters, along with errors corresponding to twice the standard deviation.

The rotational temperature deduced in this fitting procedure was 110 K. This temperature was then assumed to be equal to the vibrational temperature that governs the population of the higher v_7 levels. Fig. 3.5 shows the fitting obtained for the first four Q -branches, and it is seen that the relative intensities of these are reasonably well reproduced, although a somewhat lower vibrational temperature, down to 80K, would also be acceptable. Despite this uncertainty, it is clear that the v_7 assignments are correct since the relative Boltzmann factors for these are

Table 3.1
CARS Transitions and Vibrational-Rotational Parameters

<u>J Assignment</u>	<u>CARS Transition</u>	<u>Adjusted Transition</u>
16	2199.9166	2199.9160
18	2199.9024	2199.9015
20	2199.8866	2199.8859
22	2199.8695	2199.8692
24	2199.8495	2199.8485
26	2199.8290	2199.8285
28	2199.8066	2199.8065
30	2199.7827	2199.7825
32	2199.7545	2199.7517
34	2199.7287	2199.7272
36	2199.7017	2199.7021
38	2199.6716	2199.6717
40	2199.6399	2199.6401
42	2199.6037	2199.6007

Final Parameters

$\Sigma_g^+ \leftarrow \Sigma_g^+(0)$	J-2	J	J+2
ν_0	2199.960(3)	2199.9721(6)	2199.983(3)
$B'-B'' \times 10^4$	-2.18(3)	-2.029(6)	-1.91(2)
R^2	0.99519	0.99997	0.99959

	$\Pi_u \leftarrow \Pi_u(1^1)$	$\Delta_g \leftarrow \Delta_g(2^2)$	$\Sigma_g^+ \leftarrow \Sigma_g^+(2^0)$
ν_0	2199.481	2198.642	2197.935

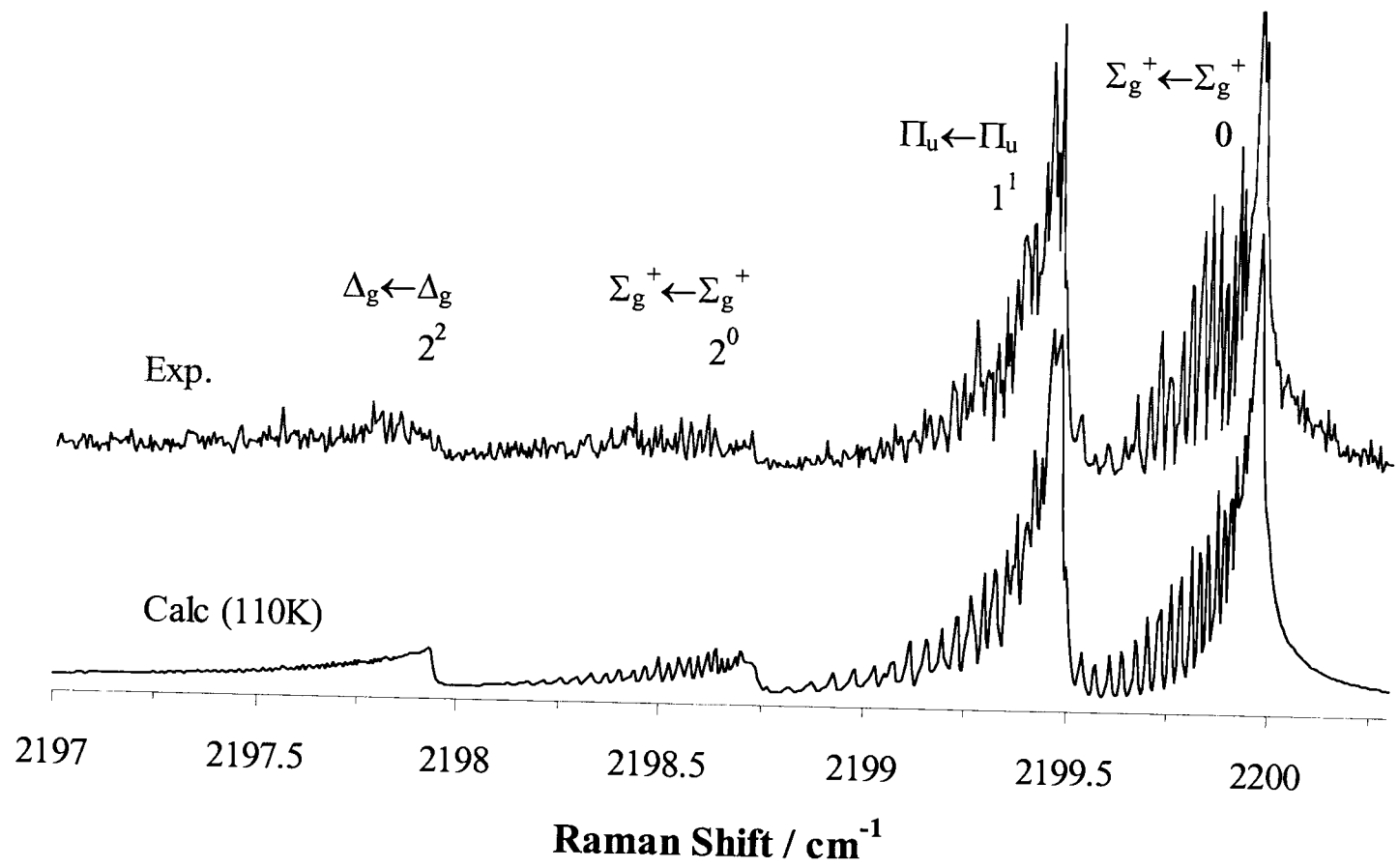


Fig. 3.5 The vibrational modeling of C_3O_2 .

particularly sensitive to temperature. Note that there is more resolved structure in the $v_7=2^0 \Sigma \leftarrow \Sigma$ transition than in the $2^2 \Delta \leftarrow \Delta$ transition, again expected from nuclear spin statistics. Thus the regular v_7 ordering shown in the middle of Fig. 3.1 is believed to be correct. In the fitting procedure, the $B'-B''$ differences were all taken to be the same as for the $\Sigma - \Sigma$ transition but the individual v_0 values were varied to give a best visual fit to the jet spectra. The resulting values are listed in Table 3.1.

3.3.3 Implications for v_7 Bending Potential in the v_1 Manifold

The present results indicate that there is only a small change in the effective bending potential when the symmetric CO stretch is excited. From our measured value of $B'-B''$ and assuming the CCC framework is unaffected, one can estimate a net increase of only 0.41 pm in the CO bond length (116.4 pm, ref. 47) when v_1 is excited. Our assignments show that the v_7 level spacings **decrease** slightly compared to the ground state, the opposite of the predictions from the earlier Raman studies. As seen in Fig. 3.1, decreased level spacings are consistent with a slight increase (estimated at about 1-2 cm^{-1}) in the barrier to linearity. Since the CO moieties do not contain the central carbon atom, it is perhaps not surprising that symmetric excitation of the CO stretch has little effect on the bending potential. However it must be remembered that excitation of the antisymmetric CO stretch more than triples the barrier height. This indicates that symmetry of

charge flow during the course of the vibrations is an important factor in determining the ease with which bending can occur around the central carbon.

3.3.4 Axial Force Constants and Bonding in C_3O_2

Our value of ν_1 , along with literature values for the ν_2 , ν_3 , and ν_4 axial modes, allows one to calculate some of the axial force constants for carbon suboxide. The relationships, along with their calculated values are given in Tables 3.2 and 3.3. There are six internal force constants describing axial motion but only four observables so we make the assumption that the CO--CO interaction constant is zero and also that the C'C--CO interaction is zero. With these assumptions we obtain the results shown in Table 3.3. Also listed there for comparison are some bond stretching force constants for a few other relevant molecules.

From these values, it can be seen that the CO stretching constant is in between those of carbon monoxide (triple bond) and carbon dioxide (double bond) whereas the CC stretching constant is slightly higher than that of a double bond (C_3H_4).

These results can be partially rationalized in terms of the valence bond resonance structures:

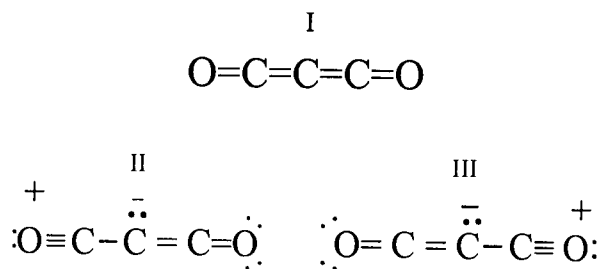


Table 3.2
Harmonic Force Constant Relations for C₃O₂^a

$$\lambda_1 + \lambda_2 = (\mu_O + \mu_C)F_{11} + \mu_C F_{22} - 2\mu_C F_{12}$$

$$\lambda_1 \lambda_2 = \mu_O \mu_C (F_{11} F_{22} - F_{12}^2)$$

$$\lambda_3 + \lambda_4 = (\mu_O + \mu_C)F_{33} + (\mu_C + 2\mu_M)F_{44} - 2\mu_C F_{34}$$

$$\lambda_3 \lambda_4 = (5\mu_O \mu_C)(F_{33} F_{44} - F_{34}^2)$$

$$f_{11} = f_{CO} + f_{CO,CO} \approx f_{CO}$$

$$f_{22} = f_{CC} + f_{CC,CC}$$

$$f_{12} = f_{CO,CC} + f_{CO,CC} \approx f_{CO,CC}$$

$$f_{33} = f_{CO} - f_{CO,CO} \approx f_{CO}$$

$$f_{44} = f_{CC} - f_{CC,CC}$$

$$f_{34} = f_{CO,CC} - f_{CO,CC} \approx f_{CO,CC}$$

$$^a \mu_i = m_i^{-1}$$

Table 3.3
Internal Force Constants for C₃O₂ and Related Molecules

Molecule	F _{CO}	F _{CC}	F _{CC,CC}	F _{CO,CC}
O=C=C=C=O C ₃ O ₂ ^a	1654	1085	135	127
O=C=O CO ₂ ^b	1550			
C≡O CO ^c	1901			
C=C=C C ₃ ^d		1026	45	
H ₂ C=C=CH ₂ C ₃ H ₄ ^e		995	74	
H ₂ C=CH ₂ C ₂ H ₄ ^b		957		

^a This work

^b Ref. 49

^c Ref. 50

^d Ref. 51

^e Ref. 52

Structure I, the classical representation, is generally thought to be mixed with ionic forms such as II and III. The latter will tend to give somewhat stronger CO bonds, as observed, and also will favor bent structures, so that a low bend frequency should result. However, it would also predict a reduction in the C=C bond force constant, rather than the slight increase observed experimentally. Brown *et al.* (48) consider an alternative description of the bonding in terms of molecular orbitals with some success, but these arguments are complex and will not be discussed here.

4 Conclusion

This thesis has highlighted the application of two complementary methods of high resolution spectroscopic analysis, infrared and coherent Raman (CARS) spectroscopy, to the study of two simple but "difficult" polyatomic molecules.

The analysis of sulfur trioxide demonstrated how there are circumstances where these two methods of study are intimately interconnected. Through careful, systematic assignment of infrared data, causes of the complicated CARS spectrum were revealed. Thus, the collaborative team effort to analyze the high quality infrared data makes this molecule one of the most (if not the most) accurately determined non-linear polyatomic molecules known. The study of the ^{18}O isotopomers performed in this work has contributed to this effort by revealing the effects isotopic substitution have on the vibrational, rotational and interaction terms of SO_3 . This body of work sets a standard for future studies of isotopic variants of other molecules. In a practical way these findings will be of value in subsequent diagnostic studies of sulfur trioxide where the frequencies and abundance of both pure and mixed isotopic species are of interest. For example, some of our detailed results have already been requested for diagnostic application by researchers at the Jet Propulsion Laboratory and by a commercial company, Physical Sciences Inc.

Highlighted in the study of carbon suboxide was the utility of coherent Raman techniques. Due to the high line density and collisional broadening, the

best method of analysis proved to be sampling of C_3O_2 cooled by jet expansion. Only with a technique such as CARS, where the probe beams could be focused just under the jet nozzle, would such a measurement be possible. In this study, the assignments of the $\nu_7 = 0-3$ hot bands were found to conflict with those identified in the literature. This has implications not only on the infrared analysis of the combination/difference bands involving this vibration, but also in the description of its potential energy surface. The latter is important in characterizing the cause of the low frequency bending found in C_3O_2 and other long carbon chain molecules. Consequently, future work is suggested on the ν_2 vibration of C_3O_2 . This symmetric carbon-carbon stretch suffers from the same hot band complications as in this work, suggesting that CARS spectra taken in a jet expansion might be equally revealing.

Bibliography

1. E.t.H. Chrysostom, N. Vulpanovici, T. Masiello, J. Barber, J.W. Nibler, A. Weber, A. Maki, and T.A. Blake, *J. Mol. Spectrosc.* **210**, 233-239 (2001).
2. A. Maki, T.A. Blake, R.L. Sams, N. Vulpanovici, J. Barber, E.t.H. Chrysostom, T. Masiello, J.W. Nibler, and A. Weber, *J. Mol. Spectrosc.* **210**, 240-249 (2001).
3. J. Barber, E.t.H. Chrysostom, T. Masiello, J.W. Nibler, A. Maki, A. Weber, T.A. Blake, and R.L. Sams, *J. Mol. Spectrosc.* **216**, 105-112 (2002).
4. J. Barber, T. Masiello, E.t.H. Chrysostom, T. Masiello, J.W. Nibler, A. Maki, A. Weber, T.A. Blake, and R.L. Sams, *J. Mol. Spectrosc.* **218**, 197-203 (2003).
5. J. Barber, T. Masiello, E.t.H. Chrysostom, T. Masiello, J.W. Nibler, A. Maki, A. Weber, T.A. Blake, and R.L. Sams, **218**, 204-212 (2003).
6. S.W. Sharpe, T.A. Blake, R.L. Sams, A. Maki, T. Masiello, J. Barber, N. Vulpanovici, J.W. Nibler, The ν_3 and $2\nu_3$ Bands of $^{32}\text{S}^{16}\text{O}_3$, $^{32}\text{S}^{18}\text{O}_3$, $^{34}\text{S}^{16}\text{O}_3$, and $^{34}\text{S}^{18}\text{O}_3$. *J. Mol. Spectrosc.* (in press).
7. L. Young, A. Young, *Scientific American*. **233(3)**, 71-78 (1975).
8. R.M. Nelson, W.D. Smythe, *Icarus*. **66**, 181-187 (1986).
9. H. Gerding, W. J. Nijveld, and G. J. Muller, *Nature* **137**, 1033 (1936); *Z. Phys. Chem. B* **(35)**, 193-215 (1937).
10. H. Gerding, and J. Lecomte, *Nature* **142**, 718 (1938); *Physica* **6**, 737-763 (1939).
11. K.J. Palmer, *J. Am. Chem. Soc.*, **60**, 2360-2369 (1938).
12. CRC Handbook of Chemistry and Physics, 74th Edition, D. Lide Editor and Chief, Boca Roton: CRC Press, 1993-1994.
13. M. Leuchs, M. Crew, J. Harrison, M. F. Hineman and J. W. Nibler, *J. Chem. Phys.*, **105**, 4885-4888 (1996).
14. S. Gerstenkern and P. Luc, *Atlas du Spectra d'Absorption de la Molecule d'Iode*, Centre National de la Recherche Scientifique, Paris, France, (1978).

Bibliography (Continued)

15. J. Barber, Ph.D. Thesis, Oregon State University (2003).
16. D. Papousek, and M. R. Aliev, "Molecular Vibrational-Rotational Spectra", Elsevier, Amsterdam (1982).
17. H. C. Allen Jr., and, P. C. Cross, "Molecular Vib-Rotors", John Wiley & Sons, Inc., New York (1963).
18. J.M.L. Martin, *Spectrochim. Acta. Part A* **55**, 709-718 (2000), and private communication.
19. E. B. Wilson, Jr., J. Decius, and P. C. Cross, "Molecular Vibrations", Dover, New York (1980).
20. L. Hedberg and I.M. Mills, *J. Mol. Spectrosc.* **160**, 117-142 (1993); **203**, 82-95 (2000).
21. C.H. Townes and A.L. Schawlow, "Microwave Spectroscopy", Dover, New York (1975).
22. J.F. Ogilvie, "The Vibrational and Rotational Spectrometry of Diatomic Molecules", Academic Press, New York, 1998.
23. F.A. Cotton and G. Wilkinson, "Advanced Inorganic Chemistry", 3rd ed. Interscience, New York, (1972).
24. O. Diels and B. Wolf, *Ber.* **39**, 689-697 (1906).
25. M. Shimizu, "*Proc. – Symp. Planet. Atmos*", Jones, A. Vance Editors, 67-69 (1977).
26. T.P. Sheahen, *Combustion and Flame.* **22**(2), 243-251 (1974).
27. W.T. Plummer and R.K. Carson, *Astrophysical Journal.* **159**(1) Pt. 1, 159-163, (1970).
28. E.B. Jenkins and D.C. Morton, *Astrophysical Journal.* **157**(2) Pt. 1, 913-924 (1969).

Bibliography (Continued)

29. M.L. Delitsky and A.L. Lane, *J. Geophysical Research*. **103**(E13), 31-291-31-403 (1998).
30. W.T. Huntress Jr., M. Allen and M. Delitsky, *Nature*, **352**, 316-317 (1991).
31. V.I. Oyama, B.J. Berdahl and F. Woeller, *Life Sciences and Space Research*. **17**, 47-51 (1979).
32. J. Vander Auwera, J.W.C. Johns, and O.L. Polyansky, *J. Chem. Phys.* **95**(4), 2299-2316 (1991).
33. J. Koput, *Chem. Phys. Lett.*, **320**(3,4), 237-244 (2000).
34. L. Gausset, G. Herzberg, A. Lagerqvist, and B. Rosen, *Astrophys. J.* **142**(1), 45-76 (1965).
35. J.-E. Lolck and S. Brodersen, *J. Mol. Spec.* **75**, 234-244 (1979).
36. J.-E. Lolck and S. Brodersen, *J. Mol. Spec.* **72**, 445-462 (1978).
37. L.A. Carreira, R.O. Carter, J.R. Durig, R.C. Lord, and C.C. Millionis, *J. Chem. Phys.* **59**(3) 1028-1037 (1973).
38. A.D. Walters, M. Winnerwisser, K. Lattner, and B.P. Winnewisser, *J. Mol. Spec.* **149**, 542-556 (1991).
39. W.H. Weber, P.D. Maker, and C.W. Peters, *J. Chem. Phys.* **64**(5), 2149-2158 (1976).
40. J. Vander Auwera, J.K. Holland, P. Jensen, J.W.C. Johns, *J. Mol. Spec.* **163**(2) (1994).
41. L. Fusina, and I.M. Mills, *J. Mol. Spec.* **79**(1), 123-131 (1980).
42. P. Jensen, *J. Mol. Spec.* **104**(1), 59-71 (1984).
43. P. Jensen, and J.W.C. Mills, *J. Mol. Spec.* **118**(1), 248-266 (1986).
44. K.A. Vereschagin, V.V. Smirnov, E.T.H. Chrysostom, J.W. Nibler, *J. Raman Spec.* **31**(8/9), 719-723 (2000).

Bibliography (Continued)

45. L.E. McDougall and J.E. Kilpatrick, *J. Chem. Phys.* **42**(7), 2311-2321 (1965).
46. M.L. Orlov, J.F. Ogilvie, and J.W. Nibler, *J. Mol. Spec.* **185**, 128-141 (1997).
47. G. Walford, J.H. Clarke, and J.C. Dore, *Molec. Phys.* **36**(6), 1581-1600 (1978).
48. L.D. Brown and W.N. Lipscomb, *J. Amer. Chem. Soc.* **99**(12), 3968-3979 (1977).
49. G. Herzberg, "*Molecular Spectra and Molecular Structure: Infrared and Raman Spectra of Polyatomic Molecules*", Van Nostrand Co. Inc., Princeton, N. J. (1945).
50. G. Herzberg, "*Spectra of Diatomic Molecules*", Van Nostrand Co. Inc., Princeton, N. J. (1950).
51. K. Ramaswamy and V. Balasubramanian, *Indian. J. of Pure and Appl. Phys.* **10**(12), 853-857 (1972).
52. K. Venkateswarlu and M.G. Krishna Pillai, *Z. Physik. Chem.* **18**, 396-400 (1958).